ISTANBUL TECHNICAL UNIVERSITY ★ GRADUATE SCHOOL

DESIGN, METHODOLOGY DEVELOPMENT AND PRODUCTION OF COMPOSITE CRYOGENIC LIQUID OXYGEN TANK FOR SPACE APPLICATIONS

Ph.D. THESIS

Recep UFUK

Department of Mechanical Engineering

Mechanical Engineering Programme

FEBRUARY 2024

ISTANBUL TECHNICAL UNIVERSITY ★ GRADUATE SCHOOL

DESIGN, METHODOLOGY DEVELOPMENT AND PRODUCTION OF COMPOSITE CRYOGENIC LIQUID OXYGEN TANK FOR SPACE APPLICATIONS

Ph.D. THESIS

Recep UFUK
(503152024)

Department of Mechanical Engineering

Mechanical Engineering Programme

Thesis Advisor: Prof. Dr. İ. Murat EREKE
Thesis Co-Advisor: Assoc. Prof. Dr. Arif KARABEYOĞLU

FEBRUARY 2024

ISTANBUL TEKNİK ÜNİVERSİTESİ ★ LİSANSÜSTÜ EĞİTİM ENSTİTÜSÜ

UZAY UYGULAMALARINA YÖNELİK KOMPOZİT KRİYOJENİK SIVI OKSİJEN TANK TASARIMI, METODOLOJİ GELİŞTİRİLMESİ VE ÜRETİMİ

DOKTORA TEZİ

Recep UFUK
(503152024)

Makina Mühendisliği Anabilim Dalı

Makina Mühendisliği Programı

Tez Danışmanı: Prof. Dr. İ. Murat EREKE
Eş Danışman: Doç. Dr. Arif KARABEYOĞLU

ŞUBAT 2024

Recep UFUK, a Ph.D. student of İTU Graduate School student ID 503152024, successfully defended the thesis/dissertation entitled "DESIGN, METHODOLOGY DEVELOPMENT AND PRODUCTION OF COMPOSITE CRYOGENIC LIQUID OXYGEN TANK FOR SPACE APPLICATIONS", which he prepared after fulfilling the requirements specified in the associated legislations, before the jury whose signatures are below.

Thesis Advisor :	**Prof. Dr. İ. Murat EREKE** Istanbul Technical University	.....
Co-advisor :	**Assoc. Prof. Dr. Arif KARABEYOĞLU** Koç University	.....
Jury Members :	**Prof. Dr. Zahit MECİTOĞLU** Istanbul Technical University	.....
	Prof. Dr. Ersan ÜSTÜNDAĞ Istanbul Technical University	.....
	Assoc. Prof. Dr. Çağlar ÜÇLER Ozyegin University	.....
	Prof. Dr. Onur TUNÇER Istanbul Technical University	.....
	Dr. Fatih USTA Gebze Technical University	.....

Date of Submission : 25 December 2023
Date of Defense : 16 February 2024

To my family, beloved spouse and my child Ahmet Agah,

FOREWORD

I am honored to present my PhD thesis, a pivotal point in my academic journey. This accomplishment owes much to the constant support and guidance I have received from numerous individuals and organizations.

First and foremost, I want to thank my family and my wife. Their constant belief in me, patience, and encouragement have been the foundation of my academic pursuits. Their sacrifices and support mean the world to me.

I also want to express my gratitude to my colleagues at DeltaV Space Technologies Inc. I've been fortunate to work with brilliant minds who have shared their knowledge and insights, contributing to the development of my research. Our teamwork and collaboration have been invaluable.

I owe a special thanks to my friend and colleague, Dr. Kaan BİLGE. His contributions, leadership, and continuous support have been essential to my success. His presence has inspired me throughout this journey.

I'd like to acknowledge the guidance and support of Doç. Dr. Çağlar ÜÇLER. His expertise and mentorship have had a significant impact on my research, and I'm fortunate to have had him as a mentor.

Additionally, I'm deeply grateful to my advisors, Prof. Dr. İ. Murat EREKE and Doç. Dr. Arif KARABEYOĞLU. Their wisdom, guidance, and dedication to my academic growth have been crucial to my success.

In conclusion, I want to thank everyone who has played a part in my academic journey. This thesis represents the collective effort of a supportive network that has helped me reach this point. As I look ahead to the future, I'm excited to continue my pursuit of knowledge with the same passion, dedication, and support that have carried me through this PhD journey.

December 2023

Recep UFUK
(Mechanical Engineer)

TABLE OF CONTENTS

Page

ABBREVIATIONS

ABS : Acrylonitrile Butadiene Styrene
ACP : Ansys Composite PrepPost
AFP : Automated Fiber Placement
AIT : Auto Ignition Temperature
ALOOH : Nanosheet Boehmite
ASTM : American Society for Testing and Materials
CAD : Computer Aided Design
CCTD : Composite Cryotank Technology Demonstration Project
CFRP : Carbon Fiber Reinforced Plastics
CHATT : Cryogenic Hypersonic Advanced Tank Technologies
CTE : Coefficient of Thermal Expansion
DCB : Double-Cantilever Beam
DCOD : Delaminated Crack Opening Displacement
DGBEA : Bisphenol A Diglycidyl Ether
DLR : German Aerospace Center
DSC : Differential Scanning Calorimetry
ENF : End-Notched Flexure
EU : European Union
FE : Finite Element
FEA : Finite Element Analysis
FEM : Finite Element Method
GCD : Game Changing Development Program
GOX : Gas Oxygen
ISO : International Organization for Standardization
ITS : Interplanetary Transport System
LH2 : Liquid Hydrogen
LM : Lockheed Martin
LN2 : Liquid Nitrogen
LOX : Liquid Oxygen
LO2 : Liquid Oxygen

MMB : Mixed-Mode Bending
MSFC : Marshall Space Flight Center
MUPET : Multiple Use Precision Extractable Tooling
MWCNT : Multiwalled Carbon Nanotubes
NASA : National Aeronautics and Space Administration
NI : National Instruments
OOA : Out-Of-Autoclave
PEAR : Polyetheramide Resin
PEEK : Polyether ether ketone
PTFE : Polytetrafluoroethylene
PVA : Polyvinly Alcohol
RT : Room Temperature
RUC : Repeated Unit Cell
RVE : Representative Volume Element
SCZM : Surface Cohesive Zone Model
SEM : Scanning Electron Microscopy
SG : Strain Gauge
TRL : Technology Readiness Level
TTT : Time Temperature Transformation
UD : Uni-Directional
UK : United Kingdom
US : United States
USA : United States of America
VBMT : Vibration-based Monitoring Techniques
VGCF : Vapor-Grown Carbon Fiber
XFEM : Extended Finite Element Method

SYMBOLS

$\mathbf{A_\varepsilon}$	**:** Strain amplification factor vector for temperature increment
$\mathbf{A_\sigma}$	**:** Stress amplification factor vector for temperature increment
$\overline{\mathbf{C}}$	**:** Macro stiffness matrix
$\mathbf{C_M}$	**:** Resin compressive strength
D	**:** Beam center maximum deflection
$\overline{\mathbf{E}}$	**:** Macro elastic modulus matrix
$\mathbf{E_c}$	**:** Composite modulus of elasticity
$\mathbf{E_f}$	**:** Fiber modulus of elasticity
$\mathbf{E_m}$	**:** Matrix modulus of elasticity
$\mathbf{E_{flex}}$	**:** Modulus of elasticity in bending
$\mathbf{G_{ij}}$	**:** Shear modulus components
$\mathbf{G_{IIc}}$	**:** Mode-II fracture toughness
$[\mathbf{H}]^{\mathbf{e}}$	**:** Unit microscopic stress field of a unit cell under unit strain loading
$\mathbf{I_{ij}}$	**:** Invariant components of stress tensor
L	**:** Support span
$\mathbf{L_{thickness}}$	**:** Thickness
$\mathbf{M_\varepsilon}$	**:** Strain amplification factor matrix for macro mechanical strains
$\mathbf{M_\sigma}$	**:** Stress amplification factor matrix for macro mechanical stresses
P	**:** Load at a given point on the load-deflection curve
S	**:** Local compliance matrix at a certain internal point of UD
$\overline{\mathbf{S}}$	**:** Macro compliance matrix
$\{\mathbf{S}\}^{\mathbf{e}}$	**:** Unit thermal loading case stress field on the fiber-matrix scale calculated
$\mathbf{V_f}$	**:** Fiber volume fraction ratio
$\mathbf{V_m}$	**:** Matrix volume fraction ratio
$\mathbf{T_g}$	**:** Glass transition temperature
$\mathbf{T_{gmax}}$	**:** Maximum glass transition temperature
$\mathbf{T_M}$	**:** Resin tensile strength
$\mathbf{X_f^c}$	**:** Fiber compressive strength values
$\mathbf{X_f^t}$	**:** Fiber tensile strength values

$\mathbf{X_{mt}}$ **:** Resin tensile strength

a **:** Delamination crack length

b **:** Width of beam tested

d **:** Depth of beam tested

g **:** Standard earth gravity

h **:** Drop height

k **:** Thermal conductiviy

m **:** Slope of the tangent to the initial straight-line portion of the load-deflection curve

p **:** Pressure

r **:** Radius

t **:** Vessel thickness

q **:** Heat flux

α **:** partially cured systems' degree of cure in isothermal temperatures

$\overline{\boldsymbol{\alpha}}$ **:** Macro coefficient of thermal expansion matrix

δ **:** Maximum displacement

$\boldsymbol{\varepsilon}$ **:** Micro strain matrix

$\overline{\boldsymbol{\varepsilon}}$ **:** Macro total strain matrix

$\{\boldsymbol{\varepsilon^{M}}\}$ **:** Macroscopic strains determined by traditional finite element analysis

$\boldsymbol{\varepsilon_{flex}}$ **:** Strain in the outer surface

$\overline{\boldsymbol{\varepsilon}}_{\mathbf{mech}}$ **:** Macro mechanical strain

$\overline{\boldsymbol{\varepsilon}}_{\mathbf{ther}}$ **:** Macro thermal strain

$\boldsymbol{\nu_{ij}}$ **:** Poissons's ratio components

$\boldsymbol{\sigma}$ **:** Micro stress matrix

$\overline{\boldsymbol{\sigma}}$ **:** Macro stress matrix

$\boldsymbol{\sigma_{\text{Fiber Direction}}}$ **:** Macro stress value of ply on fiber direction

$\boldsymbol{\sigma_{flex}}$ **:** Stress in the outer fibers at midpoint

$\boldsymbol{\sigma_{f1}}$ **:** Maximum axial microstress value on fiber

$\boldsymbol{\sigma_{\text{Transverse Direction}}}$**:** Macro stress value of ply on transverse direction

$\{\boldsymbol{\sigma^{u}}\}^{\mathbf{e}}$ **:** Unit cell's microscopic stress field at particular macroscopic stresses

$\boldsymbol{\sigma_{VM}}$ **:** VonMises stress value

$\boldsymbol{\tau_{23}}$**,** $\boldsymbol{\tau_{31}}$**,** $\boldsymbol{\tau_{12}}$ **:** Shear stress components

Δt **:** Falling time

ΔH **:** Enthalpy

$\boldsymbol{\Delta H_{curing}}$ **:** Curing enthalpy

ΔH_r **:** Enthalpy needed to complete cure reaction

ΔT **:** Temperature change

LIST OF TABLES

Page

LIST OF FIGURES

Page

DESIGN, METHODOLOGY DEVELOPMENT AND PRODUCTION OF COMPOSITE CRYOGENIC LIQUID OXYGEN TANK FOR SPACE APPLICATIONS

SUMMARY

The thesis focuses on the development of composite cryogenic liquid oxygen (LOX) tanks for sounding rocket propulsion systems, addressing challenges in aerospace engineering. Traditional composite materials used in these tanks are expensive and subject to various regulations in their supply chain. This thesis explores cost-effective alternatives, emphasizing affordable and sustainable aviation applications.

This is the first study conducted in Turkey on cryogenic composite tank systems. Through this study, numerous infrastructures and laboratory systems were established, marking the first step towards indigenous development of these systems for research and development. All of these efforts will pave the way for structural advancements within Turkey's National Space Program.

Cryogenic temperatures and LOX compatibility are the primary challenges for composite LOX tanks. To ensure the tank's operation in a cryogenic environment, various aspects need to be studied, including epoxy and fiber behavior in cryogenic conditions, thermal expansion coefficient compatibility between liner material and composite material, and LOX compatibility. Although properties of many materials under high and room temperatures are available in the literature, there is a lack of sufficient testing and information for cryogenic environments, especially for composite materials.

For LOX compatibility, it's crucial that the composite structure doesn't trigger the combustive properties of liquid oxygen. The success in developing these innovative tanks relies on designing new materials specifically tailored to meet macro and micro-scale thermomechanical requirements. These materials must address long-term structural integrity, leakage due to microcracks, and contamination concerns in composite materials.

The original contribution of this research is the detailed presentation of the entire process of developing a composite liquid oxygen fuel tank, including material screening, design, analysis methods, manufacturing processes, and quality controls. The thesis aims to deliver all phases of the reliable composite oxygen fuel tank development for use in sounding rockets.

Although significant work on cryogenic composite tanks is currently underway, there is no consistent and comprehensive publication. This research aims to obtain conclusive results using numerical and experimental studies, demonstrating the advantages and disadvantages of using composite LOX tanks.

The study focuses on the thermal and mechanical properties of different epoxy resins under cryogenic conditions and their compatibility with liquid oxygen. It also

examines the fracture toughness of laminate-based testing under both room and cryogenic temperatures. Two types of tank structures were tested: tanks with a metal liner (Type-II) and linerless tanks (Type-V). A method that links micro and macro scales was developed to calculate real stresses on fiber and matrix components, providing insights into the composite structure's damage state.

At the beginning of the study, the properties of epoxy resins were thoroughly examined to evaluate their mechanical performance and compatibility with liquid oxygen in cryogenic conditions. Collaboration with local manufacturers aimed to develop domestic formulations, promoting nationalization in aviation materials and supporting self-sufficiency. The study revealed that the Huntsman 1564-3474 epoxy system showed potential mechanical performance in a cryogenic environment and demonstrated compatibility with LOX. However, a Type-V tank system produced with this resin system suffered complete damage after a liquid nitrogen filling test, indicating its unsuitability for cryogenic environments.

Fracture toughness tests on composite laminates produced by filament winding provided insights into mode-II damage types under room and cryogenic conditions, predicting and preventing critical information on damage. Fractographic analysis revealed differences in damage modes under room and cryogenic conditions. In particular, vacuum infusion and toughened resin systems exhibited similar mode-II fracture toughness values at room and cryogenic temperatures, while the behavior of the cold-curing resin system showed a significant decrease in cryogenic temperatures. Additionally, the study evaluated the negative effects of the wet filament winding method on production quality. These findings emphasized the importance of considering component interactions and production-related issues for cryogenic environment performance.

During the study, a micro stress calculation tool was developed through literature assistance to predict actual stress values on components in composite structures. In this method, fiber and matrix components within the composite structure are modeled using a representative unit cell element, simulating the behavior of all components throughout the laminate with the help of periodic boundary conditions. This enables a connection between stress values on the composite layer modeled as an orthotropic material at the macro scale and stress values at the micro level. Python programming language, MATLAB, Abaqus, and ANSYS softwares were used to develop the calculation tool. The tool's added parameterization capability allowed evaluating the effect of temperature-dependent changes in material properties on micro-scale stress values. This provides foresight for determining the necessary material properties under cryogenic conditions. Additionally, the epoxy systems used in the tests were evaluated using this calculation tool. Considering Von Mises stress, Epotek 301-2 and 301-2FL emerged as a potential systems for cryogenic temperatures based on its temperature-dependent elastic modulus and thermal expansion coefficient. Similarly, the T7110 system stood out in minimizing maximum stress on the matrix but could not provide sufficient strength for pressurized tanks under room temperature conditions. Commercial epoxy systems and the proven cryogenic performance of the IM7-977-3 system were compared, evaluating their cryogenic performances.

One of the main contributions of this study is revealing the effects of various tank geometries and epoxy materials on micro stresses, highlighting the emergence of constituent effects.

Furthermore, the research emphasizes the importance of material selection and design parameters for cryogenic applications by revealing the limitations of specific tank systems. Design, production, and testing studies were carried out for Type-II and Type-V tank systems, and design evaluations were performed.

It was determined that Type-II tank systems are unsuitable for cryogenic applications due to high thermal expansion differences between the metal liner and composite material in cryogenic temperatures. Under cryogenic conditions, the metal and composite shell experienced high delamination forces due to high thermal expansion differences.

For the development of a low-cost cryogenic Type-V tank, innovative methods such as a liquefiable paraffin mandrel and wet filament winding were utilized. At the end of the studies, a successful prototype Type-V pressure tank was produced, capable of withstanding pressures up to 30 bars without any leaks. However, after a liquid nitrogen filling test, the same tank was observed to crack completely, losing its non-permeability.

Throughout the thesis process, the aim was to work on each sub-problem, but due to the scale of the proposed study, some limitations were encountered. There are some recommendations to further expand the study, which include:

Mechanical and thermal tests based on component and component interaction should be expanded to better assess material performance at different temperatures.

The thermal and mechanical properties of each composite component should be determined as a function of temperature.

Manufacturing using the wet filament winding method introduces uncertainties for composite materials. The production of such space systems is generally accomplished with prepreg materials and automated fiber placement systems.

NDT measurement techniques for determining microcrack evolution on composite laminates could be researched and developed under cryogenic environments. Determining fiber/matrix interaction under cryogenic conditions is crucial for developing composite cryogenic pressure vessels.

In conclusion, this thesis makes significant contributions to the development of cryogenic liquid oxygen tanks by exploring new materials, manufacturing techniques, and analytical methods. The findings not only extend the boundaries of cryogenic composite tank technology but also open doors to new possibilities for cost-effective and sustainable aviation applications. The results of the study are intended to provide a solid foundation for future advancements in this critical field.

UZAY UYGULAMALARINA YÖNELİK KOMPOZİT KRİYOJENİK SIVI OKSİJEN TANK TASARIMI, METODOLOJİ GELİŞTİRİLMESİ VE ÜRETİMİ

ÖZET

Tez çalışması, havacılık mühendisliği alanındaki zorluklara odaklanarak özellikle sonda roket itki sistemleri için kompozit kriyojenik sıvı oksijen basınç tanklarının geliştirilmesine odaklanmaktadır. Bu tankların geliştirilmesinde kullanılan geleneksel kompozit malzemeler yüksek maliyetli olmakla birlikte, tedarik edilmesi birçok regülasyona tabidir. Tez çalışmasında bu tür malzemelerin aksine, uygun fiyatlı alternatiflere odaklanarak maliyet etkin ve sürdürülebilir havacılık uygulamalarına yönelik çalışma gerçekleştirilmiştir.

Bu tez, Türkiye'de kriyojenik kompozit tank sistemleri üzerine yapılan ilk çalışmadır. Bu çalışma ile birlikte, birçok altyapı ve laboratuvar sistemi kurulmuş olup, bu sistemlerin yerli olarak araştırılması ve geliştirilmesine yönelik atılan ilk adım olması nedeniyle de önemli bir kilometre taş oluşturmuştur. Tüm bu çalışmalar, Türkiye'nin Ulusal Uzay Programı içinde yapısal ilerlemelerin önünü açacaktır.

Kriyojenik sıcaklıklar ve sıvı oksijen (LOX) uyumluluğu, kompozit LOX tankları için iki temel sorunu oluşturmaktadır. Kriyojenik sıcaklıklarda çalışabilecek kompozit basınçlı tank geliştirilmesinde birçok alt konuda çalışma yürütülmesi gereklidir. Bu kapsamda, kriyojenik koşullarda epoksi ve fiber davranışı, gömlek malzemesi ile kompozit malzeme arasındaki termal genleşme katsayısı uyumluluğu ve LOX uyumluluğu, incelenmesi gereken ana konulardır. Birçok malzemenin yüksek sıcaklık ve oda sıcaklığı koşulları için termomekanik özellikleri literatürde bulunabilirken, özellikle kompozit malzemeler için kriyojenik ortamlara ait yeterli test ve bilgi bulunmamaktadır.

Sıvı oksijen uyumluluğu açısından, kompozit yapının sıvı oksijenin yanıcı özelliklerini hiçbir şekilde tetiklememesi gereklidir. Kriyojenik yakıt uygulamalarında kütlesel ve performans açısından en etkili oksitleyicilerden biri olan sıvı oksijenin depolanmasında kullanılan tankların kompozit malzeme kullanılarak geliştirilmesi ve bu yolla ağırlık azaltılarak itki performansının arttırılması amaçlanmaktadır.

Kriyojenik kompozit tankların geliştirilmesinde malzemelerin makro ve mikro ölçekteki termomekanik davranışlarının anlaşılması büyük önem arz etmektedir. Makro ve mikro seviyede geliştirilecek yüksek performanslı kompozit bileşenleri aynı zamanda uzun vadeli yapısal bütünlük, mikro çatlaklardan kaynaklanan sızıntı ve kompozit malzemelerde oluşabilecek üretim kaynaklı hataları da ele almalıdır.

Bu araştırmanın özgün yanı, kompozit sıvı oksijen tankının geliştirilme sürecinin tüm aşamalarını, malzeme inceleme, tasarım, analiz yöntemleri, üretim süreçleri ve kalite kontrolleri dahil olmak üzere ayrıntılı bir şekilde ortaya koymasıdır. Tez, sonda uzay roketlerinde kullanılmak üzere güvenilir bir kompozit oksijen yakıt tankının geliştirilmesine ait aşamaları sunmayı hedeflemiştir.

Günümüzde kriyojenik kompozit tankların geliştirilmesi amacı ile birçok çalışma gerçekleştirilmekte, fakat literatürde kapsamlı bir yayın bulunmamaktadır. Bu araştırma, teorik ve deneysel çalışmalar kullanarak kompozit LOX tank kullanmanın avantajlarını ve dezavantajlarını açıkça gösteren bir sonuç elde etmeyi amaçlamaktadır. Ayrıca, dünya genelinde nadir bir yeteneğin ülkeye kazandırılması amaçlanmıştır.

Çalışmada çeşitli epoksi reçinelerin termal ve mekanik özellikleri, kriyojenik koşullardaki performansları ve sıvı oksijen ile uyumlulukları incelenmiştir. Buna ek olarak, laminat bazlı kırılma tokluğu testleri oda ve kriyojenik sıcaklık koşullarında gerçekleştirilmiştir. Çalışma içerisinde gömlekli (Tip-II) ve gömleksiz (Tip-V) olmak üzere iki tip tank yapısı incelenmiştir. Literatür yardımıyla geliştirilen, mikro ve makro ölçekleri birbirine bağlayarak fiber ve matris bileşenleri üzerindeki gerçek gerilmeleri hesaplamayı sağlayan yöntem sayesinde kompozit yapı hasar durumu detaylı şekilde incelenmiştir.

İlk aşamada epoksi reçinelerin özellikleri detaylı bir şekilde incelenmiş, bu reçinelerin kriyojenik koşullardaki mekanik performansı ve sıvı oksijen ile uyumlulukları değerlendirilmiştir. Yerel üreticilerle işbirliği yaparak yerli formülasyonlar geliştirilmesi amaçlanmış, havacılık malzemelerinde millileşmeyi ve kendi kendine yeterliliğin desteklenmesi hedeflenmiştir. Test sonuçlarının değerlendirilmesi sonucunda, Huntsman 1564-3474 epoksi sistemi kriyojenik ortamda mekanik olarak potansiyel bir performans göstermekle birlikte bu reçine sisteminin LOX uyumluluğuna da sahip olduğu gözlenmiştir. Ancak, bu reçine sistemi ile üretilen Tip-V tank sistemi sıvı azot dolum testi sonrası tamamıyla hasar aldığından bu reçine sisteminin kriyojenik ortamlar için uygun olmadığı anlaşılmıştır. Ek olarak reçine sistemlerinin kriyojenik ortam performansı değerlendirilirken fiber/matris etkileşiminin de göz önüne alınarak değerlendirilme yapılması gerektiği anlaşılmıştır. Çalışma, epoksi moleküler yapısını ve kriyojenik davranış üzerindeki etkisini araştırarak, literatürün yardımıyla malzemelerin aşırı düşük sıcaklıklardaki performansına dair içgörüler sunmuştur.

Filaman sarım yöntemi ile üretilmiş kompozit laminat kırılma tokluğu testleri, oda sıcaklığı ve kriyojenik ortam altındaki mod-II hasar tiplerine dair içgörüler sunmuş, hasarı tahmin etmek ve önlemek için kritik bilgiler sağlamıştır. Fraktografik analizler, oda sıcaklığı ve kriyojenik koşullar altındaki hasar modu farklılıklarını ortaya koymuştur. Özellikle, vakum infüzyon ve toklaştırılmış reçine sistemleri oda sıcaklığı ve kriyojenik ortamlarda benzer mod-II kırılma tokluğu değerleri sergilerken, soğuk kürlenebilen reçine sistemi davranışı kriyojenik sıcaklıklarda ciddi düşüş göstermiştir. Bunun yanında çalışma, ıslak filament sarma yönteminin üretim kalitesine olan olumsuz etkilerini değerlendirmiştir. Bu bulgular, kriyojenik ortam performansı için bileşen etkileşimleri ve üretimle ilgili konuların göz önüne alınmasının önemini vurgulamıştır.

Çalışma sürecinde kompozit yapılardaki bileşenlerin üzerindeki gerçek gerilme değerlerinin öngörülmesi adına literatür yardımı ile mikro stress hesaplama aracı geliştirilmiştir. Bu yöntemde kompozit yapı içerisindeki fiber ve matris bileşenleri temsili birim hücre elemanı kullanılarak modellenmekte ve periyodik sınır koşulları yardımıyla tüm laminat içerisindeki bileşen davranışı simüle edilebilmektedir. Bu sayede makro ölçekte ortotropik malzeme olarak modellenen kompozit tabaka üzerindeki gerilme değerleri ve mikro ölçekteki gerilme değerleri arasında bağlantı kurulabilmektedir. Hesaplama aracı geliştirilirken Python yazılım dili, MATLAB,

Abaqus ve ANSYS yazılımları kullanılmıştır. Ayrıca, hesaplama aracına parametrizasyon kabiliyeti de eklenerek malzeme özelliklerinin sıcaklığa bağlı değişiminin mikro ölçekteki gerilme değerleri üzerine etkisi değerlendirilmiştir. Bu sayede kriyojenik koşullar altında gerekli malzeme özelliklerinin kolay ve hızlı bir şekilde belirlenmesine yönelik öngörü sağlanabilmektedir. Ek olarak epoksi testlerinde kullanılan reçine sistemleri de bu hesaplama aracı yardımı ile değerlendirilmiştir. Von Mises stresi dikkate alındığında Epotek 301-2 ve 301-2FL sıcaklığa bağlı elastisite modülü ve termal genleşme katsayısı özelinde kriyojenik sıcaklıklar için potansiyel sistemler olarak öne çıkmıştır. Yine T7110 sistemi de matris üzerindeki maksimum stresi en aza indirme konusunda öne çıkmakla birlikte oda sıcaklığı koşullarında basınçlı tanklar için yeterli dayanımı sağlayamamaktadır. Ticari epoksi sistemleri ve kriyojenik yeterliliği kanıtlanmış IM7-977-3 sistemi karşılaştırılarak, kriyojenik performanslar değerlendirilmiştir.

Numune ve prototip seviyelerinde test kapasitelerinin kurulması, düşük maliyetli kriyojenik tank teknolojisinin gelecekteki ilerlemelerine öncülük eden önemli bir kilometre taşı oluşturmuştur. Çalışmanın katkılarından biri de, farklı tank geometrilerinin ve farklı epoksi malzemelerinin mikro gerilmeler üzerindeki etkilerini değerlendirerek, bileşen etkisinin ortaya çıkarılmasıdır.

Ayrıca, araştırma belirli tank sistemlerinin sınırlamalarını ortaya koyarak, kriyojenik uygulamalar için malzeme seçimi ve tasarım parametrelerinin önemini vurgulamaktadır. Tip-II ve Tip-V tank tasarımı, üretimi ve test çalışmaları gerçekleştirilmiş ve tasarım değerlendirmeleri gerçekleştirilmiştir. Testler sonucunda, Tip-II tank sistemlerinin kriyojenik sıcaklıklarda gömlek ve kompozit malzeme arasındaki yüksek termal genleşme farkından dolayı kriyojenik uygulamalar için uygun olmadığı belirlendi. Kriyojenik koşullarda metal ve kompozit kabuk, yüksek termal genleşme farklarından kaynaklanan delaminasyon hasarı ile karşılaştı. Daha sonrasında, düşük maliyetli bir kriyojenik Tip-V tankın geliştirilmesi amacı ile, sıvılaştırılabilir bir parafin mandrel ve ıslak filament sarma yöntemi kullanıldı. Çalışmalar sonunda, 30 bar hidrostatik basınç seviyesine kadar herhangi bir sızıntı yaşamadan dayanabilen başarılı bir prototip Tip-V basınç tank üretildi. Ancak, aynı tankın sıvı azot dolum testi sonrasında kompozit yapının tamamen çatladığı ve sızdırmazlık kabiliyetinin kaybolduğu gözlemlendi.

Tez süreci boyunca her bir alt problem üzerinde çalışma gerçekleştirilmesi amaçlanmasına rağmen önerilen çalışmanın büyüklüğü bazı kısıtlamalara yol açmıştır. Aşağıda verilen önerilerle bu çalışma daha da genişletilebilir:

Bileşen bazlı ve bileşen etkileşimi bazlı mekanik ve termal testler, malzemelerin sıcaklığa bağlı performanslarını daha iyi değerlendirmek adına genişletilmelidir.

Her bir kompozit bileşenine ait termal ve mekanik özellikler sıcaklığa bağlı olarak belirlenmelidir.

Üretim tekniği ıslak filaman yöntemindeki belirsizlik ve üretim hatalarından kaçınmak adına, prepreg malzemeler ile ya da otomatik fiber yerleştirme makinaları yardımı ile yapılabilir.

Kriyojenik ortamlarda mikro çatlak oluşumunu ve ilerlemesini belirlemek için hasarsız ölçüm teknikleri araştırılabilir ve geliştirilebilir.

Sonuç olarak, tez, yeni malzemeleri, üretim tekniklerini ve analitik yöntemleri keşfederek kriyojenik sıvı oksijen tanklarının gelişimine önemli katkılarda bulunmaktadır. Bulgular, kriyojenik kompozit tank teknolojisinin sınırlarını

genişletmekle kalmayıp, aynı zamanda maliyet etkin ve sürdürülebilir havacılık uygulamaları için yeni olanakların kapısını aralamaktadır. Çalışmanın sonuçlarının, bu kritik alanda gelecekteki ilerlemeler için sağlam bir temel oluşturması amaçlanmıştır.

1. INTRODUCTION

Propellant pressure vessels, which are commonly utilized in space missions, play a major role in launch vehicles in terms of weight [1,2]. Today's technology enables the fabrication of these tanks from composite materials, which saves weight. Although there are many studies and manufacturers in the literature about composite pressure vessels, the subject of cryogenic composite pressure vessels requires some more detailed study. Also, one of the most critical issues for space applications is the production of liquid oxygen tanks from composite materials.

Cryogenic temperatures and liquid oxygen (LOX) compatibility can be considered the two main problems for composite LOX tanks. In order to ensure the ability of the tank to work in a cryogenic environment, it is necessary to carry out studies on many sub-issues. Here, epoxy and fiber behavior in cryogenic conditions, compatibility of thermal expansion coefficients between the composite material and liner material, and LOX compatibility are the main issues that need to be investigated [3,4]. Although it is possible to find the properties of many materials in the literature for high temperature and room temperature conditions, sufficient tests and knowledge are not available for cryogenic environments, especially for composite materials. Regarding liquid oxygen compatibility, the composite structure should not trigger the flammable properties of liquid oxygen in any way. Liquid oxygen, which is one of the most effective oxidizers in terms of mass and performance for cryogenic fuel in space applications [5], and this LOX tank will be realized with composite structures, which are one of the most effective methods of weight reduction. In the end, the achievement of creating these innovative tanks relies heavily on the effective development of novel materials designed to meet the specific needs of both macro and micro scales. These materials should also tackle issues related to prolonged structural durability, potential microcracking-induced leakage, and the preservation of composite materials to ensure overall success.

The thesis aims to provide a framework for developing a low-cost composite liquid oxygen-compatible tank. The thesis provides information about the mechanical and

thermal behavior of composite structures, as well as manufacturing procedures. In this study, two different designs are investigated: a tank with liner (Type-II) and linerless tank (Type-V). The study involves many multi-physical interactions.

Many sub-problems were investigated, such as fiber and epoxy thermal interaction in cryogenic medium and their behavior with inner liner, supply/development of epoxy that is suitable for cryogenic environment, liquid oxygen and epoxy compatibility for linerless structure, composite-metal connections, creation of finite element modeling procedures, creation of production methods.

1.1 Purpose of Thesis

The unique aspect of this research is to reveal all phases of a developing low-cost composite liquid oxygen tank, including material screening, design, analyzing methods, and fabrication processes.

Currently, there is a considerable amount of work about cryogenic composite tanks, but there is limited coherent and comprehensive published work. The research aimed to generate a result that clearly shows the advantages and disadvantages of using composite LOX tanks by using numerical and experimental studies.

This research would greatly contribute to the development of the Turkish National Space Program by decreasing the dead weight of space and launch vehicles. Identifying and characterizing the behavior of composites with LOX and production steps for composite LOX tanks will contribute to development of new lightweight space launchers.

Although there have been successful companies that have developed LOX propellant tanks, there is not enough information about issues related to material development, production techniques, design, and analysis methods. This thesis is aimed to present fully open-source information that will contribute to the literature.

The thesis provides a database of mechanical and thermal properties for composite materials by utilizing tests in a cryogenic environment. In addition, knowledge of liquid oxygen compatibility is also obtained. Further developments will pave the way for light and cheap solutions for space missions.

1.2 Literature Review

The literature review is focused on full tank development studies. Previous and ongoing research on cryogenic composite and LOX tanks have sbeen documented in the literature. However, there is a scarcity of detailed studies on this topic.

The CHATT Project [6–9], an EU-funded initiative, commenced in 2012 and concluded in June 2015. Its primary objective was the development of carbon fiber-reinforced (CFRP) cryogenic pressure vessels. The project's key findings and technological advancements are detailed in a published paper, including the design, construction, and testing of four sub-scale tanks. The project's overall budget exceeded €4.2 million, with the EU contributing nearly €3.3 million. The project duration was 42 months, starting in January 2012 and ending in June 2015. Eleven partners from seven European countries participated in the CHATT Project [6–9].

As part of the CHATT Project's framework, four distinct sub-scale CFRP tanks were designed, fabricated, and subjected to mechanical and thermal loading tests (Table 1.1). The primary challenge in designing cryogenic CFRP tanks lies in addressing the issues arising from differences in coefficients of thermal expansion (CTE) at the microscopic level. If a liner is incorporated into the tank design, the CTE compatibility between the liner and the structural shell must also be considered. The study investigated the advantages and disadvantages of linered versus linerless tank designs and addressed the complexities associated with manufacturing tanks with intricate geometric shapes. The TU Delft tank study is not within the scope of this thesis [6–9].

Table 1.1 : Filament winded tanks in CHATT project [6].

Manufacturer	Liner Material	Filament Winding	Tank Diameter	Tank Length	Tank Volume	Fiber Material	Resin System
DLR	Polyethylene	Wet	1m	3m	$1.9m^3$	Glass and Carbon	Huntsman Araldite® LY 564 - Aradur® 22962
ALE	Polyethylene	Dry Winding	0.29m	0.57m	33 L	T700	-

The CHATT Project's testing of CFRP tanks revealed valuable insights into their performance under various conditions. The DLR tank exhibited leakage under pressure during water testing. Cryogenic testing with liquid nitrogen at 77K resulted in minor

leakage at the flange regions. While no visible defects were observed following thermal cycles, cracking sounds were detected [6–9].

Under cryogenic conditions with 12 bar pressure, the ALE tank (Figure 1.1) demonstrated its maximum strain, remaining below the allowable strain limit for T700 (1.03%). Notably, during cooling, the PE liner contracted more than the fibers, creating a gap of approximately 5 to 10 mm between the two materials. Under higher pressures, the fibers would bear the load as the liner expanded, provided it could stretch adequately to close the gap without cracking. However, as a precaution, the CHATT Project did not subject this tank to such high pressures under cryogenic conditions.

As a result, the full potential of carbon fiber reinforcement in aerospace applications was not entirely showcased for the dry-wound tank under relevant conditions. The ALE tank underwent a controlled, slow cooling process to minimize thermal gradients. After filling to around 80% volume, the vessel underwent twelve pressure cycles, including 1 cycle to 0.6 bar, 10 cycles to 0.5 bar, and a final cycle to 1.0 bar, all using LN2 to account for boil-off. Importantly, no structural failures were observed throughout the testing.

Subsequent to cryogenic filling and drying, the two demonstrator tanks, which remained intact, were repressurized at room temperature to at least 12 bar to validate their strength. Encouragingly, no failures occurred during these tests [6–9].

Figure 1.1 : Demonstrator tank of ALE after winding [1].

The linerless tanks created by Swerea SICOMP and FOI in Sweden deviate from closed-volume tanks and instead adopt the form of open-ended tubes with a cylindrical section. In this investigation, a new material, the Carbon Fiber Spread Tow TeXtreme® 50 UD TR50S WO /20:50, unidirectional and with a ply thickness of 50

μm, was employed. The construction involved winding four layers of traditional T700 at ±45° and incorporating 20 layers of thin-ply TeXtreme® at ±25°. The outcomes of mechanical testing confirmed that the chosen design configuration for the linerless tank concept achieved the desired performance [6–9].

McDonnell Douglas Aerospace-West (MDA-W) has dedicated several years to researching composite cryogenic tank technology. MDA-W has conducted tests on the hydrogen permeability of composite materials, the properties of composite materials and structural adhesives in cryogenic environments, and the design, fabrication, and testing of liquid hydrogen tanks. LH2 must be stored and used at −253°C. This study reviews the findings of all these activities and assesses the compatibility of composite materials with liquid oxygen. The study demonstrates promising results for linerless composite liquid hydrogen tanks [10].

Composite material properties tests at liquid hydrogen temperatures and impermeability tests before and after cycling can be considered for the development of composite LOX tanks due to the lower temperature and easier containment of oxygen (Figure 1.2, Figure 1.3 and Figure 1.4). The only remaining concern is material compatibility [10].

	Hydrogen permeation			
	Before thermal cycling		After thermal cycling*	
	Detected	Undetected	Detected	Undetected
Thermosets				
Glass/PC	X			
IM7 Carbon/1808 epoxy		X		X
IM7 Carbon/8551-7 epoxy		X		
Thermoplastics				
Glass/PPS	X			
Glass/PBT	X			
Glass/PEEK	X			
Carbon/PI (KIII)	X			
Carbon/PPS		X	X	
T300 Carbon/F650 BMI		X	X	
G40 Carbon/5145C BMF		X	X	
IM6 Cabon/V378A BMI		X		X
AS4 Carbon/APC-2 PEEK		X		X
IM6 Carbon/APC-2 PEEK		X		X
AS4 Carbon/PAS 2		X		
C3000 Carbon/PEI		X		
Cypac 7005		X	X	

*Room temperature to 94 K (–290°F)

Figure 1.2 : Summary of permeability testing at 78K [10].

Material system	Type	Uncycled permeation at 4 K (scc/sec/in.²)	Permeation at 4 K after thermal cycling (scc/sec/in.²)	Permeation at 4 K after thermal and mechanical cycling (ssc/sec/in.²)	Material layup
IM6/APC-2 (Peek)	Thermo-plastic	<2 E-6	<2 E-6	<2 E-6	[+45°, –45°, 0°, 0°, 0°, –45°, +45°]
AS4/8551-7	Thermo-set	<2 E-6	<2 E-6	<2 E-6	[+45°, –45°, 0°, 0°, –45°, +45°]
IM6/18271-E	Thermo-set	<2 E-6	<2 E-6	<2 E-6	[+45°, –45°, 0°, 0°, +45°, +45°]
IM6/1827	Thermo-set	<2 E-6	<2 E-6	<2 E-6	[+45°, 0°, –45°, +45°, 0°, +45°]
T40/9405 w/FM1000 Interleaf	Thermo-set	<2 E-6	<2 E-6	<6 E-4	[0°, 90°, FM1000, 90°, 0°]

Note 1: Thermal cycling consisted of 150 cycles from room temperature to 4 K—performed by MDAC-HB.
Note 2: Mechanical cycling consisted of 150 cycles at 4 K from 0 to 43 ksi—performed by Materials Research and Engineering, Boulder, CO.

Figure 1.3 : Summary of permetion tests [10].

Material system	Type	Uncycled tensile at R.T. (ksi)	Uncycled tensile at 4 K (ksi)	Tensile at 4 K after thermal cycling (ksi)	Tensile at 4 K after thermal and mechanical cycling (ksi)	Material layup
IM6/APC-2 (Peek)	Thermo-plastic	145.2 (2)	153.0 (4) S.D. = 24.4	172.8 (4) S.D. = 27.8	172.2 (6) S.D. = 13.1	[+45°, −45°, 0°, 0°, 0°, −45°, +45°]
AS4/8551-7	Thermo-set	—	152.0 (4) S.D. = 3.3	—	164.6 (4) S.D. = 7.0	[+45°, −45°, 0°, 0°, −45°, +45°]
IM6/18271-E	Thermo-set	—	127.2 (4) S.D. = 4.9	—	116.6 (2)	[+45°, −45°, 0°, 0°, −45°, +45°]
IM6/1827	Thermo-set	—	100.4 (4) S.D. = 8.4	—	109.8 (2)	[+45°, 0°, −45°, +45°, 0°, +45°]
T40/9405 w/FM1000 Interleaf	Thermo-set	—	94.8 (2)	—	121.0 (2)	[0°, 90°, FM1000, 90°, 0°]

Note 1: Numbers in ( ) indicate quantity of specimens tested.
Note 2: S.D. represents Standard Deviation.
Note 3. Thermal cycling consisted of 150 cycles from room temperature to 4 K—performed by MDAC-HB
Note 4: Mechanical cycling consisted of 150 cycles at 4 K from 0 to 43 ksi — performed by Materials Research and Engineering, Boulder, CO.

Figure 1.4 : Summary of tensile tests [10].

Composite materials offer superior oxidation resistance compared to metals. Oxidation resistance tests were conducted by submerging three common composite materials in LOX and measuring weight loss after extended exposure (Figure 1.5). The mass loss of composite samples was negligible (<0.1%) after 184 hours, attributed to the loss of absorbed moisture present in the composites prior to exposure. After 190 hours in GOX at 6.89 bar and −183°C, four composite samples averaged only 0.12% weight loss and only 0.65% after 450 hours. These studies demonstrate the applicability of composite cryogenic tanks [10].

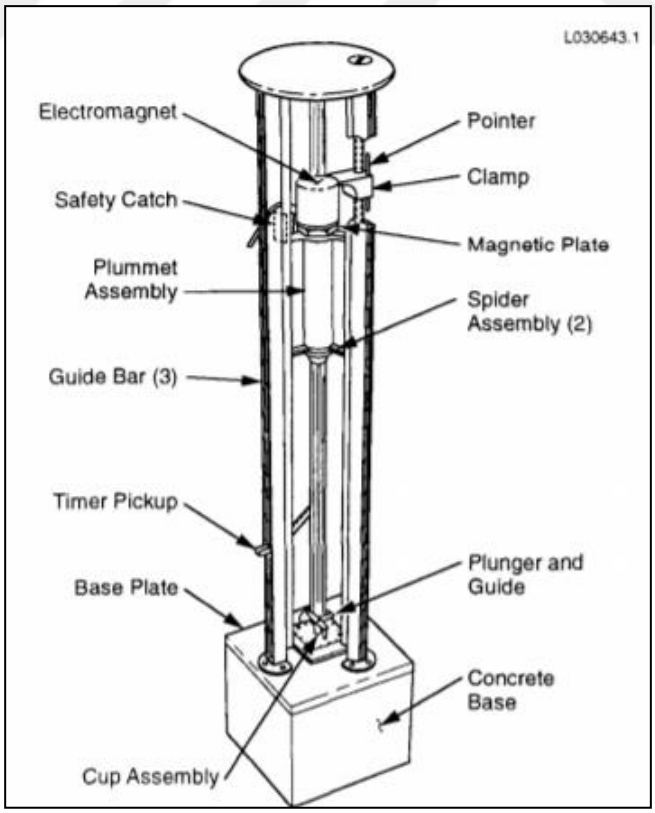

Figure 1.5 : LO_2 impact sensivity tester [10].

In 1987, McDonnell Douglas Aerospace developed the initial prototype composite cryotank for the National Aerospace Plane (NASP) program. Subsequently, in 2001, a collaborative effort between Lockheed Martin and NASA achieved the successful initial testing of a composite tank in LO_2, marking a significant milestone as the first subscale LO_2 cryogenic composite tank. The inaugural LO_2 cryogenic proof tests were completed successfully [11].

The composite fuel tank featured a cylindrical geometry, measuring 251 mm in length, with isotension domes at both ends (Figure 1.6). T1000 carbon fibers were wound around aluminum liners, with winding angles ranging from 9.1° to 65.6° for the upper and lower domes and from 17.2° to 74.1° [11].

The construction involved six layers in various directions using helical winding and nine layers in the hoop direction. The layer arrangement in the cylindrical region from outer to inner was $[90_3/\pm 13]_3 90_3$. Notably, each CFRP layer had a thickness of 0.2 mm, while the aluminum liner had a thickness of 1 mm.

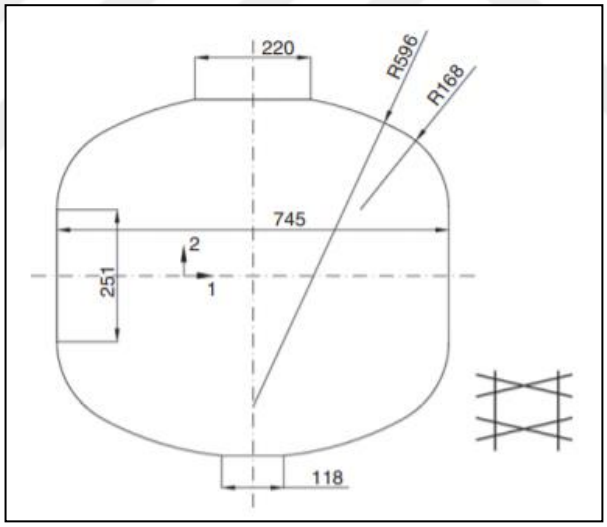

Figure 1.6 : Schematic drawing showcasing the composite fuel tank along with its underlying fiber structure [11].

The study also proposed vibration-based monitoring techniques (VBMT) for damage detection and safety evaluation of composite fuel tanks. However, it also acknowledged the need for improvements due to the dynamic fluid property effects on mechanical systems [11].

Failure reasons of NASA and Lockheed Martin Corporation's X33 RLV composite LH2 tank was discussed also in literature. The tank was 8.68m in length, 6.1m in width, and 4.3m in height. Investigations identified four primary failure reasons [12,13]:

i) Inner face-sheet cracking, leading to the potential leakage of both liquid and gaseous hydrogen

ii) Elevated core pressure attributed to the presence of liquid and gaseous hydrogen

iii) Diminished bond-line strength and toughness

iv) Presence of manufacturing flaws and defects

The structure of the X-33 fuel tank wall comprised two layers of IM7/977-2 graphite/epoxy composite encasing a honeycombed Kevlar core (KorexTM+3-pcf) (Figure 1.7). The primary cause of failure was extensive transverse cracking in the inner IM7/977-2 face-sheet. These cracks resulted from combined mechanical and thermal residual stresses. The coupling and merging of these cracks facilitated hydrogen leakage into the honeycombed Kevlar core.

Upon emptying the tank and subsequent temperature increases, the cracks closed, trapping hydrogen between the two layers of IM7/977-2 laminate. As temperature continued to rise, the trapped hydrogen expanded, leading to pressure buildup within the honeycombed Kevlar core, ultimately causing the rupture of the outer layer of graphite/epoxy composite [12,13].

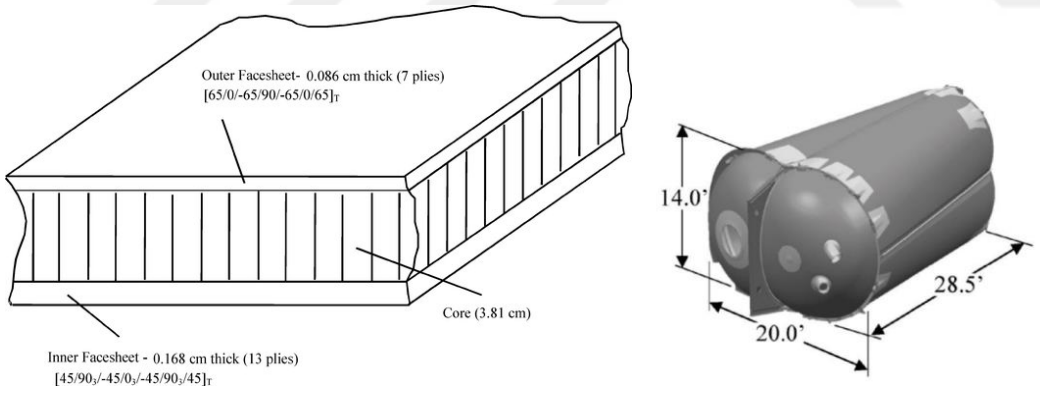

Figure 1.7 : LH2 cryotank (Lockheed X-33 composite) (a) honeycomb sandwich structure configuration and (b) dimensions of the tank [13].

The stress analysis showed that thermal residual stresses account for 80-98% of the total stress when applied with pressures ranging from 65 to 1500 kPa. The 21-46% of fiber stress in the fiber direction was caused by pressure at 1500 kPa. The acceleration loads from launching had a minor effect [13]. The study proposed a fuel leakage-based progressive failure analysis. The progressive failure behavior of laminates is notably influenced by updates in instantaneous temperature, temperature gradients resulting

from fuel leakage, and adjustments in laminate stiffness matrices. In the case of IM7/5250-4 at −253°C and 1500 kPa, an analysis based on fuel leakage-induced progressive failure revealed that the conventional method of updating laminate stiffness matrices may not capture the complete laminate cracking caused by the initial ply failure during the early stages [13].

The first part of the Type IV multi-spherical composite-overwrapped pressure vessel development study examines the mechanical performance of this vessel type for cryogenic storage in hypersonic aircraft. Employing a finite element-based model coupled with progressive failure analysis, the research evaluates the pressure window of the multi-sphere at ambient conditions and examines heat transfer mechanisms during cryogenic operations. The noteworthy finding is the absence of damage in the composite overwrap at cryogenic temperatures, indicating the potential suitability of Type IV multi-spherical COPVs for cryogenic storage. Complementing this, the second segment of the study focuses on experimental assessments, including hydrostatic testing and pressure cycling with LN2. Monitoring strain and damage progression through techniques such as Digital-Image-Correlation and Acoustic Emission, the research validates the suitability of stiffness and thermal expansion fitting functions for cryogenic storage. Together, these study segments offer a comprehensive evaluation of conformal Type IV multi-spherical COPVs, combining numerical modeling and experimental validation to assess their viability in cryogenic environments [14,15].

The composite LH2 tank for DC-XA was indeed a remarkable achievement, demonstrating the potential of composite materials in cryogenic applications. Its successful development and testing paved the way for further advancements in composite cryogenic tanks (Figure 1.8). The tank's lightweight design, achieved through the use of automated fiber placement and lightweight internal insulation, highlights the significant weight savings that can be achieved with composites. Moreover, its successful completion of ground and flight tests, withstanding around 55 pressure cycles, underscores reliability and durability of composite cryogenic tanks. The DC-XA composite LH2 tank stands as a testament to the engineering ingenuity and technological advancements in the field of composite cryogenic tank development [16–18].

Figure 1.8 : DC-XA composite LH2 cryotank [13].

The TRL (Technology Readiness Level) phases outlined in the Composites Australia Conference presentation provide a structured approach to composite cryogenic tank development [19]. TRL 1-3 focuses on the fundamental building blocks, such as developing innovative resins and fibers, refining composite tow preparation techniques, and establishing advanced manufacturing and NDE (Non-Destructive Evaluation) processes. This lays the groundwork for the subsequent stages of development.

TRL 4-6 involves the practical application of these advancements in the design, fabrication, and evaluation of composite structures. This encompasses the entire process from initial design concepts to post-cure techniques, in-situ NDE, rigorous testing, and comprehensive analyses. This phase bridges the gap between laboratory research and real-world applications.

Finally, TRL 7+ represents the culmination of the development process, where the technology is mature enough for manufacturing flight vehicle structures. This involves scaling up production processes, ensuring adherence to stringent aerospace standards, and demonstrating the feasibility of integrating composite cryogenic tanks into actual launch vehicles.

Another novel approach as the AL-Li orthogrid stiffened tank geometry details provided highlight the specific design considerations for composite cryogenic tanks (Figure 1.9). The 29.7m diameter, 0.707 elliptical dome, 634.17 m^3 volume, 5 tonnes weight, and 10.5m length demonstrate the potential scale and complexity of these structures [19]. The planned demonstration composite tank with a diameter of

approximately 5.5 meters represents a significant step towards realizing the potential of composite cryogenic tanks in launch vehicles. This demonstration will give useful information on the performance and viability of these tanks in real-world applications [19].

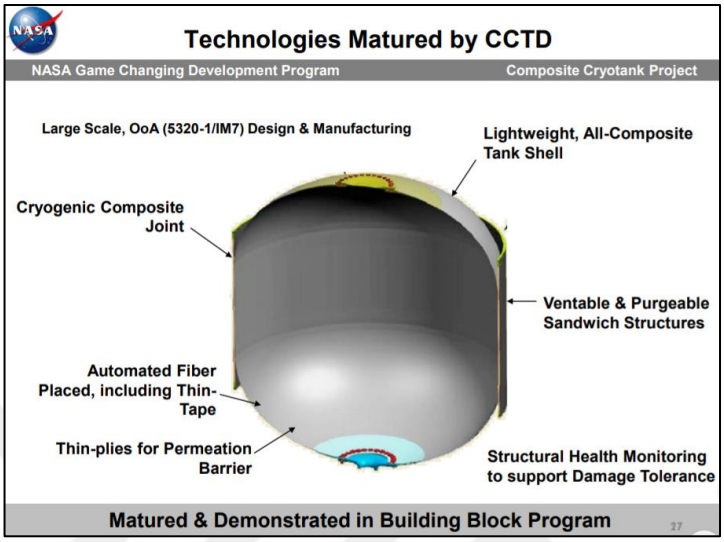

Figure 1.9 : Matured & demonstrated in building block program [19].

Particle micromechanical models have shown promise in achieving the thermomechanical requirements for cryogenic temperatures using thermoset materials with particle additives. Infinite Composites Technologies has developed the CryoSphere introduces a linerless cryotank constructed from carbon fiber and epoxy, manufactured through a filament winding process and cured in an industrial oven at their Oklahoma facility (Figure 1.10). The company asserts that this cryotank is designed to address and eliminate microcracking issues [20].

The tank successfully underwent 10 cycles of liquid nitrogen (LN2) at a pressure of 6.89 bar, encompassing temperature variations from −178.89°C to ambient temperature. After each LN2 cycle, the tank endured a 6.89 bar cryo burst and consistently maintained a pressure drop of no more than 0.69 bar during a 30-minute helium check. It was crafted using T800 carbon fiber and a room temperature cured epoxy system. To combat microcracking issues, the chemically toughened epoxy was reinforced with two different additives [20].

Graphene, purchased from Applied Graphene Materials (Cleveland, U.K.), was incorporated for nanoscale reinforcement. Graphene platelets span the space between the fibers, creating obstacles for crack formation in the laminate and enhancing the

bonding between layers. A critical consideration for cryogenic tanks is maintaining fiber alignment under thermomechanical loadings. In cryogenic conditions, the resin becomes brittle and prone to cracking. When pressure is exerted on the fibers, there is a tendency for them to slide against each other, leading to the rupture of chemical bonds. The presence of graphene platelets serves as a mechanical reinforcement between the layers of fibers, diminishing the probability of movement and fracture [20]. An additional proprietary additive was included to enhance ductility and provide further insulation for the laminate. The sphere geometry also contributes to mitigating the microcracking issue. During the filling process, the sphere geometry minimizes thermal gradients between the bottom and upper sides of the tank. The CryoSphere tank demonstrates the potential of composite materials to address the challenges of cryogenic applications. The combination of particle micromechanical models, innovative additives, and optimized geometry has led to a promising solution for cryotanks [20].

Figure 1.10 : CryoSphere developed by Infinite Composites [20].

In another study, a comprehensive approach integrating experimental and numerical methods was applied to anticipate damage and permeability in linerless cryogenic tape-laid tanks subjected to internal pressure. The study delved into understanding the temperature-dependent material characteristics of tape-laid CF/PEEK, spanning from processing to cryogenic temperatures. Optical micrography and 3D X-ray CT were utilized to evaluate defect content and damage induced by thermal cycling in the composite. The tape-laid material exhibited a vacuum content an order of magnitude higher than comparable autoclave-processed material, despite exhibiting similar trends in vacuum morphology. Finite Element Analysis (FEM) indicated that the combination of hoop and high-angle helical plies proved most effective in minimizing transverse stress levels under combined thermo-mechanical loading. A sub-model for the cryo-

tank was developed using the XFEM-SCZM methodology to predict intra- and inter-ply damage formation. Two approaches were employed to model microcrack initiation: a Weibull distribution of fracture strengths and a void-based stiffness reduction method. The optimized design featuring high-angle helical plies demonstrated reduced susceptibility to microcrack formation, consequently enhancing resistance to cryogenic leakage [21].

Composite Technology Development, Inc. (CTD) presents a comprehensive systematic approach that integrates material, design, and manufacturing processes for linerless tanks (Figure 1.11). The study showcases the application of micromechanics-based analysis in two key stages: initially, to pinpoint critical material-performance parameters guiding the development of new toughened matrices; and subsequently, to forecast the formation of microcracks and permeability in composite laminates subjected to biaxial load [4,22].

The CTD approach highlights the importance of considering all aspects of the tank development process, from material selection to manufacturing techniques, to create reliable and high-performance linerless cryogenic tanks [4,22].

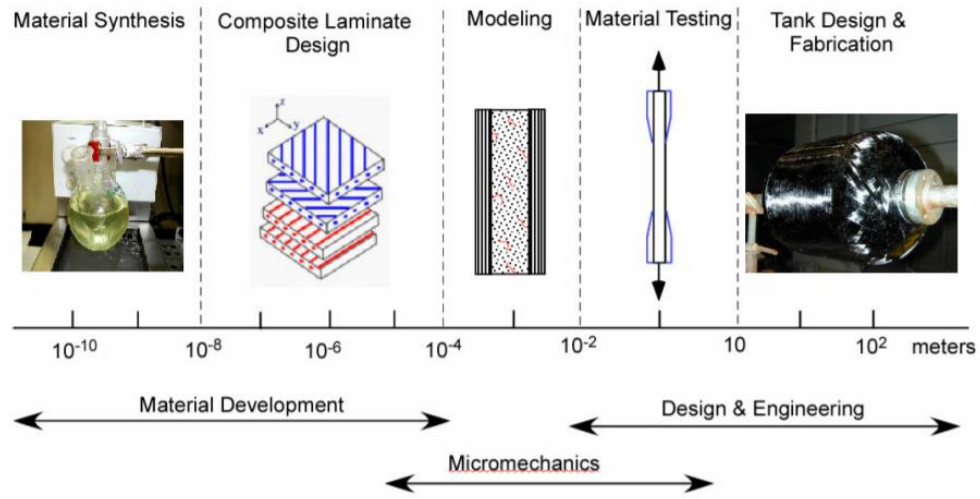

Figure 1.11 : Phases of the integrated systematic approach [4].

The material development phase primarily concentrates on the enhancement of toughened epoxy matrices to resist microcrack formation. Researchers have explored various material types for matrix formulation, including rubbers and commercially available block copolymer impact modifiers. Additionally, vapor-grown carbon fiber (VGCF) nano-reinforcements have been integrated into the matrix to improve modulus

and enhance inter-laminar shear strength at ply interfaces. Experimental results indicate that cross-ply laminates manufactured with VGCF-reinforced epoxy matrices exhibit significantly improved resistance to microcracks compared to traditional materials like Cytec's 977-2 and 977-3, commonly used in composite tanks. Moreover, for tank applications, an isostrain dome design has been proposed [4,22].

In another study, the leakage characteristics of microcracked laminates were investigated under both cryogenic and room temperature conditions using helium gas. The study utilized IM600/#133, an intermediate-modulus carbon fiber, in conjunction with a toughened epoxy system. Laminated tubular specimens were prepared to assess through-the-thickness permeability. All tubular specimens shared a common geometry, featuring a length of 200 mm with 50-mm CFRP end-tabs, leaving a 100-mm gauge section and a 30 mm inner radius. Four types of specimens were manufactured: $[45/-45/90]_s$, $[45/-45/90_2]_s$, $[90_2/-45/45]_s$, and $[90_2/0/90_2]_s$. Each ply within these specimens had a nominal thickness of 0.15 mm [23,24].

Figure 1.12 depicts the correlation between applied mechanical loadings and helium leak flux for a $[45/-45/90]_s$ specimen under cryogenic conditions.

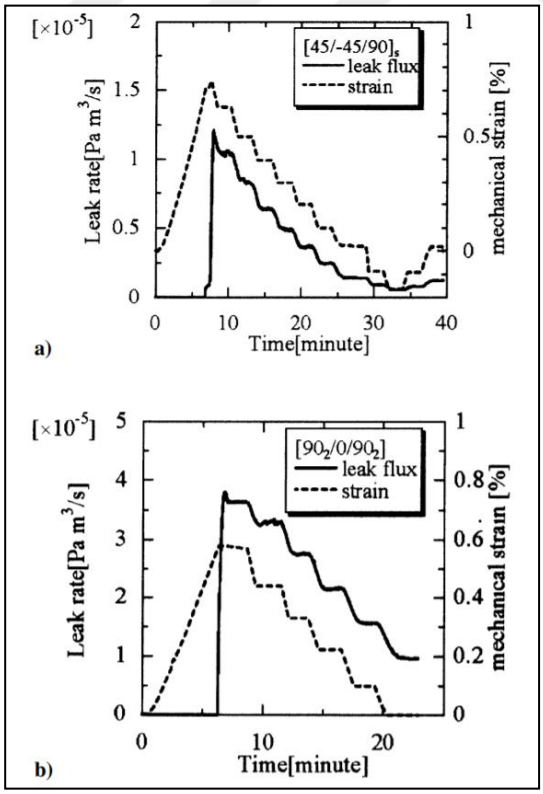

Figure 1.12 : Results of cryogenic permeation test, combined with tensile loadings, are presented in a plot illustrating leak rates and applied loadings over time: a) $[45/-45/90]_s$ and b) $[90_2/0/90_2]_s$ [24].

The measured leakage rates at room and LN2 temperatures obtained in this study encompass both "thermal" and "mechanical" effects. The results indicate that cryogenic conditions lead to higher leak rates due to increased leak path sizes resulting from residual thermal strains. Additionally, the tests suggest that cryogenic conditions have a lesser impact on damage-induced gas leakage due to reduced molecular kinetics, while the mechanical effect primarily drives the increase in leakage. In the absence of mechanical effects, only a minimal difference in leakage between the two temperatures is observed [23,24].

Zheng et al. present a comprehensive overview of carbon fiber composite applications in liquid hydrogen (LH2) and liquid oxygen (LOX) fuel tanks. The study extensively covers the materials, processing methods, and design aspects of various cryogenic tanks, including the DC-XA LH2 tank, X-33 LH2 tank, SLI LH2 tank, CCTD Program tank, Lockheed Martin LOX tank, and SpaceX LOX tank. The authors explore technological advancements, material innovations, and emerging trends in cryogenic fuel tanks, emphasizing the potential of thin-ply hybrid laminates and out-of-autoclave tanks for future space missions [13].

Northrop Grumman has played a pivotal role in advancing composite cryotank technology. Specifically, the company was involved in the design, development, and manufacturing of a composite LH2 cryotank for the Space Launch Initiative Composite Cryotank Program. The tank featured a sandwich structure, incorporating carbon fiber composite skins bonded to a nonmetallic honeycomb core. Notably, the implementation of thinner carbon fiber laminates and an increased number of cross laminates led to a remarkable 16-fold reduction in microcracks within the composite skins. This innovation signifies a significant improvement in the durability and performance of composite cryotanks [13].

The tank by Northrop Grumman integrated advanced features, such as a versatile sandwich core and a manufacturing process outside the autoclave. To prevent hydrogen permeation, the tank employed aluminum foil as a barrier between the inner skin and the honeycomb core. In case of potential hydrogen leakage, the perforated honeycomb core directed it while also serving as a thermal insulation layer. The utilization of an ultrasonic tape lamination method offered a more economical manufacturing process compared to traditional autoclave methods. The composite cryotank, with dimensions of 1.8 m in diameter and 4.5 m in length, underwent

successful tests with liquid hydrogen at an internal pressure of 827 kPa and axial loading along the launch vehicle's vertical axis. This tank, a quarter-scaled version of a typical reusable launch vehicle cryotank, underwent 40 cycles of filling, internal and external loading, and draining to evaluate structural integrity and reusability. Notably, no damage was observed during these extensive tests [13].

The Composite Cryotank Technology Demonstration Project (CCTD) was an integral component of NASA's Space Technology Program and the Game Changing Development (GCD) Program. This initiative successfully executed the design, fabrication, and testing of a full-composite LH2 cryotank. Notably, the composite cryotank achieved remarkable outcomes, including a 30% reduction in weight and a 25% reduction in cost compared to the baseline aluminum alloy cryotank. This project underscored the potential benefits of advanced composite materials in enhancing the efficiency and cost-effectiveness of cryogenic fuel tank technologies [13].

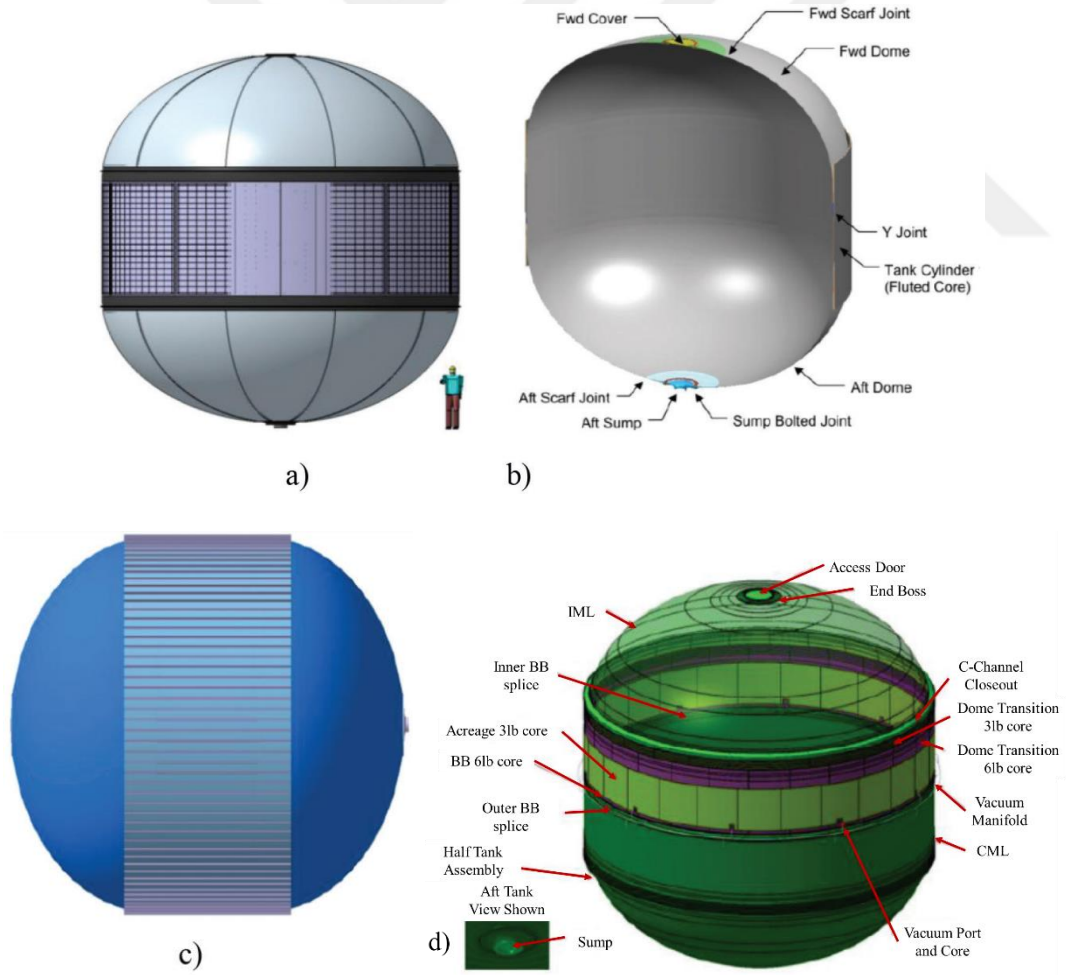

Figure 1.13 : Cryotank concepts (a) NASA al-Li concept, (b) Boeing fluted core sandwich Wall concept, (c) the Lockheed-Martin externally stiffened concept, and (d) Northrop Grumman composite honeycomb sandwich concept [13].

The NASA team developed a cryotank concept using a metallic aluminum alloy as a benchmark against three industry composite concepts utilizing IM7/977-2. While the overall dimensions of the three industry concepts were identical, their designs varied: Boeing fluted core, Lockheed-Martin externally stiffened, and Northrop Grumman sandwich (Figure 1.13). All three composite concepts realized mass reductions exceeding 30%, and their designs ensured that the laminates remained within the 5000 με strain limit specified by the CCTD Project. The manufacturing process for all three tanks involved automated fiber placement [13].

These studies and advancements highlight the significant progress in composite cryotank technology, demonstrating the potential for lighter, more efficient, and cost-effective cryogenic storage solutions for aerospace applications.

Phase II of the Composite Cryotank Technology Demonstration (CCTD) project marked a significant step forward in the development of large-scale composite cryotanks. During this phase, two large-scale composite cryotanks were designed, analyzed, built, and tested: a 2.4 meter diameter precursor tank and a 5.5 meter diameter demonstration tank (Figure 1.14). Several notable accomplishments emerged from this phase:

Cycom 5320-1 OoA Epoxy Resin Matrix: Boeing introduced a new material, Cycom 5320-1, a toughened epoxy prepreg resin system specifically tailored for out-of-autoclave (OoA) processing. This resin offered several advantages, including its ability to be cured without the need for expensive autoclave equipment. Cycom 5320-1 could be processed using the same methods as standard prepreg, but the vacuum-bag-only cured composites achieved comparable property to autoclave-cured materials, exhibiting minimal porosity and competitive mechanical properties (Figure 1.15).

Thin Ply Prepreg and Hybrid Laminate Structure: The CCTD tanks employed a hybrid laminate structure that combined thick plies (145 g/m²) for rapid placement with thin plies (70 g/m²) to enhance microcrack resistance and hinder hydrogen permeation. The report indicated that utilizing thin plies and achieving standard laminate consolidation resulted in permeation performance levels that significantly exceeded the required criteria.

Out-of-Autoclave (OoA) Cure Processing: The adoption of OoA cure processing for the composite cryotanks represented a significant advancement in manufacturing efficiency and cost-effectiveness. This method eliminated the need for autoclaves, which are costly and energy-intensive machines.

Robotic Automated Fiber Placement (AFP): The CCTD project utilized robotic AFP technology for the precise and efficient placement of composite fibers. AFP offers several advantages over manual layup techniques, including enhanced accuracy, consistency, and repeatability.

Fluted-Core Composite Skirt: The CCTD tanks incorporated a fluted-core composite skirt, a novel design that provided structural support and thermal insulation while reducing weight. The fluted-core design also facilitated the integration of plumbing and electrical components.

These advancements in materials, manufacturing methods, and design contributed significantly to the successful development of large-scale composite cryotanks. The CCTD project paved the way for the future of composite cryogenic storage solutions in aerospace applications.

Figure 1.14 : Process of out-of-autoclave curing [13].

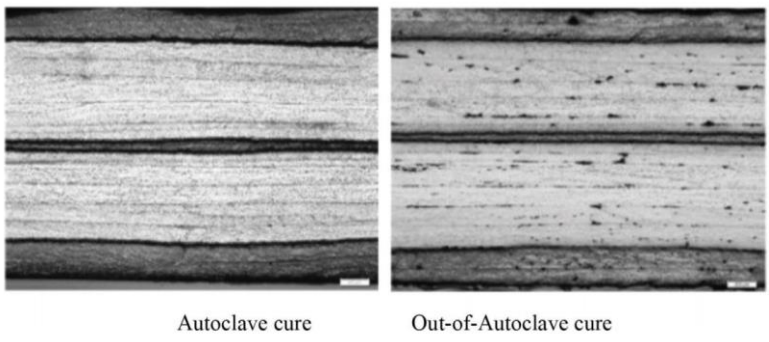

Figure 1.15 : Difference between autoclave cured and out-of-autoclave cured laminates [13].

NASA and Lockheed Martin collaborated on creating the inaugural composite cryogenic tank specifically designed for storing liquid oxygen (Figure 1.16). Lockheed Martin undertook the responsibility of designing and manufacturing a sub-scale liquid oxygen (LOX) cryotank, while NASA conducted thorough testing at its MFSC facility. The composite tank, with dimensions of 2.7 meters in length and 1.2 meters in diameter, had a weight of less than 225 kilograms, showcasing an 18% reduction compared to a similar metal tank. Rigorous cyclic tests involving liquid oxygen loading and thermomechanical simulations of space launch conditions were conducted on the tank. After undergoing 52 cycles of fill-drain liquid oxygen testing, the tank showed no signs of permeation or crack formation, confirming its successful and dependable performance [13].

This groundbreaking achievement marked a significant milestone in the development of composite cryotanks for aerospace applications. The collaboration between NASA and Lockheed Martin showcased the potential of composite materials to provide lightweight, durable, and high-performance solutions for cryogenic storage.

Composite LOx tank Composite LOx tank testing

Figure 1.16 : Lockheed Martin composite liquid oxygen pressure vessel [13].

SpaceX has made significant strides in the development of composite cryotanks for its ambitious Interplanetary Transport System (ITS). The company designed, developed, and manufactured a composite LOX tank, the largest vessel ever produced, with a diameter of 12 meters (Figure 1.17). The tank successfully passed two-thirds of the

exploration pressure test in November 2016. Toray provided the carbon fiber used in the tank's construction.

Figure 1.17 : SpaceX liquid oxygen composite tank with a diamater 12m [13].

The paper also discusses the materials commonly employed in cryogenic composite tanks. IM7, a product of Hexcel, has been widely used in NASA's cryogenic tanks. IM600, manufactured by Toho, has been utilized in Japanese cryotanks. T800H, produced by Toray, exhibits properties comparable to IM7 and IM600. All three fibers are intermediate modulus, high tensile strength, PAN-based fibers. Intermediate modulus carbon fibers with high tensile strength have gained widespread use in composite cryotank fabrication. However, higher modulus carbon fibers typically exhibit higher crystallinity, which can lead to a reduction in surface active functional groups and a degradation of the interlaminar shear strength of composites.

Toughened resins, such as Hercules' 8552 epoxy resin, ICI's 977-2 resin, and ICI's 5320-1 resin, are preferred for LH2 tanks due to their enhanced impermeability following thermomechanical cycling. Toughened resins generally demonstrate superior ignition resistance, making them suitable for LO_2 tank manufacturing.

The rapid evolution of the space market has prompted ongoing efforts to enhance the competitiveness of the Ariane 6 launcher. A pivotal facet of advancing the next generations of European Launcher Upper Stages involves the integration of composite materials and related technologies, specifically targeting cryogenic propellant tanks and various primary and secondary structures. In a collaborative initiative, ArianeGroup and MT Aerospace are actively engaged in the development of a ground demonstrator named PHOEBUS, representing a crucial stride in preparing for the evolution of a composite Upper Stage, often referred to as the "Black Upper Stage." The overarching objective of the PHOEBUS project is to elevate the Technology Readiness Level of essential Carbon Fiber Reinforced Polymer technologies to TRL

6. This multifaceted endeavor encompasses the comprehensive design, manufacturing, and testing of a CFRP demonstrator, with a focal emphasis on tanks and main structural elements. Notably, due to limitations in manufacturing capabilities, budget constraints, and time considerations, a full-scale demonstrator is unfeasible, prompting the adaptation of the PHOEBUS LH2 tank diameter to a representative 2/3rd-scale, while maintaining an almost full-scale LOX tank. A critical component of the project involves addressing intricate challenges associated with the compatibility of CFRP materials with liquid oxygen and mitigating the permeation of liquid hydrogen through thin-walled CFRP materials under conditions of high strain [25].

Adamant Composites and HyImpulse have collaborated on the development and testing of linerless CFRP LOX compatible tanks for small space launch vehicles. Utilizing Toray thermoset uni-directional prepregs, these tanks achieve significant mass and cost savings compared to traditional aluminum tanks, thereby contributing to the affordability of space access in the European market. Successful testing of the Ø600mm tank, which realized a remarkable 30% mass savings compared to aluminum, serves as a proof of concept for the design and manufacturing of these innovative CFRP tanks. The use of Toray's epoxy-based carbon fiber composite materials, selected for their mechanical properties and processability, ensures the integrity of the tanks during the challenging conditions of cryogenic temperatures. The recent validation of the Ø600mm demonstrator, slated to fly on the HyImpulse SR-75 sounding rocket, paves the way for the development of a full-scale Ø2-meter tank, a crucial component for HyImpulse's Small Launcher (SL1) set to launch in 2025. The successful hydrostatic testing of the 2 meter tank attests to its capability to withstand pressures well beyond its intended use, marking a significant milestone in the relatively new and untested application of linerless CFRP tanks in European space endeavors [26].

Commercially available patents for composite cryogenic LOX tanks exist in the literature. US Patent 6,158,605 [27] describes a method for manufacturing a pressure vessel for LOX storage using a nickel liner, graphite fibers, and foam insulation (Figure 1.18). A water-soluble mandrel with the geometry of the designed tank configuration, including boss regions, is coated with nickel. The mandrel is then wound with epoxy-wetted graphite fibers and cured. The insulating foam is placed on the mandrel, and epoxy-wetted aramid fibers are wound around it. After curing, the

water-soluble mandrel is washed away. The tank's bosses are made of nickel-plated aluminum.

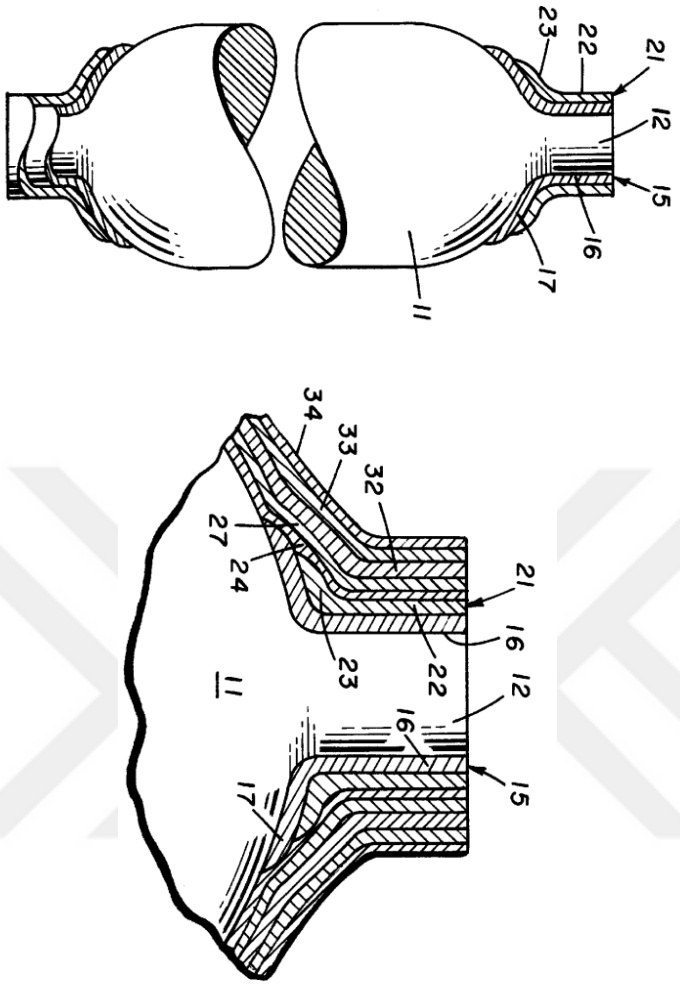

Figure 1.18 : Composite LOX tank with nickel liner [27].

US Patent 6,334,589 [28] proposes a resin-based solution for composite LOX pressure vessels. Traditionally, polymer materials have been considered non-oxygen compatible due to their higher flammability compared to metals. However, cyanate ester composites have undergone rigorous testing and demonstrated remarkable resistance to ignition in the presence of oxygen, making them a viable option for LOX storage applications.

Figure 1.19 clearly illustrates the significant weight savings achieved by utilizing composite tanks compared to aluminum tanks. The chart indicates that composite tanks can achieve weight reductions of 41% and 28% compared to 2219 aluminum and 2195 aluminum tanks, respectively. These substantial weight savings are particularly

advantageous in aerospace applications where every kilogram saved translates into increased payload capacity or improved fuel efficiency [28].

Traditionally, oxygen tanks have been predominantly manufactured from metals. A notable example is the space shuttle external tank, which was fabricated using Al2219 and 2195 aluminum/lithium alloys. These aluminum alloys offered the necessary strength and durability for cryogenic oxygen storage while maintaining a relatively lightweight structure. However, the advancements in composite materials have opened up new possibilities for lighter, more efficient, and more durable cryogenic storage solutions [28].

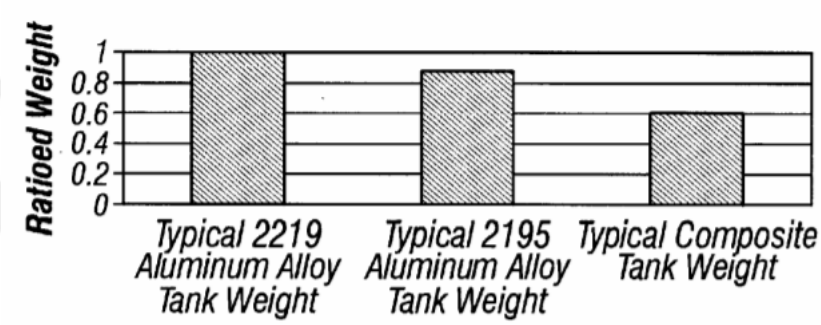

Figure 1.19 : Weight advantage of composite tank against Al alloys [28].

According to the ASTM D2512 standard [29], oxygen compatibility is described as the capability of a substance to exist alongside both oxygen and potential sources of ignition within the acceptable risk limits determined by the user. While polymer materials are generally considered non-oxygen compatible due to their higher flammability compared to metals, certain inert polymeric materials, such as cyanate esters, have demonstrated remarkable resistance to ignition in the presence of oxygen, making them viable options for LOX storage applications [28].

Cyanate ester resins offer several advantages for LOX storage applications, including their exceptional oxygen compatibility and thermal cycle endurance. These resins are formed from cyanate monomers or oligomers, which contain reactive cyanate end groups (OCN) on an aromatic ring. Upon application of heat, the cyanate monomers undergo cyclotrimerization, forming a polymer structure composed of oxygen-linked triazine rings (cyanurates) and ester groups. This unique structure imparts excellent oxygen compatibility and thermal stability to cyanate ester resins [28].

US Patent 6,375,125 B1 [30] proposes a hybrid composite structure for LOX tanks that utilizes different materials for the inner and outer layers. The inner layers are

composed of oxygen-compatible materials, such as cyanate esters, while the outer layers employ materials tailored to meet specific mechanical requirements. This hybrid approach can optimize both oxygen compatibility and mechanical performance.

US Patent 6,491,259 B1 [31] focuses on halogenated composites for oxygen systems. Halogenated composites are fiber-reinforced composites that incorporate elements from group 7A of the periodic table, such as bromine, chlorine, and fluorine. These elements form chemically stable bonds that enhance the material's ignition resistance and compatibility with oxygen and other reactive fuels.

US Patent 6,494,405 B1 [32] highlights the potential of PEAR (polyetheramide resin) composites for oxygen systems. PEAR resins exhibit high toughness and low flammability, making them suitable for LOX tank applications. These resins are characterized by the presence of multiple ether and amide groups, which contribute to their desirable properties.

US Patent 7,389,890 B1[33] introduces an innovative design for composite cryogenic tanks that incorporates an integrated floating compliant liner. This liner is composed of a layer of polytetrafluoroethylene (PTFE) or other LOX-compatible materials, such as Teflon R, in the form of microparticles. These microparticles are designed to fill in microcracks as they form, preventing the propagation of cracks and enhancing the tank's structural integrity.

In addition to the microparticle layer, the floating compliant liner also includes a microparticle sandwich structure that forms a thermal barrier between the cryogenic liquid and the tank wall. This thermal barrier helps to minimize temperature fluctuations and reduces the risk of thermal stress on the tank structure.

The development of composite cryogenic tanks for LOX storage has been driven by the need for lightweight, high-performance, and oxygen-compatible materials. Advancements in resin technology, such as cyanate esters, PEAR resins, and halogenated composites, have provided viable solutions for LOX storage applications. Additionally, innovative designs, such as hybrid composite structures and integrated floating compliant liners, have further enhanced the capabilities of composite cryogenic tanks. These advancements have opened up new possibilities for the use of composite materials in aerospace and other applications that demand high-performance cryogenic storage solutions [33].

1.3 Hypothesis

The field of aerospace engineering has long been captivated by the quest for lightweight, high-performance materials that can withstand the extreme conditions of space travel. Cryogenic liquid oxygen tanks, essential components of rocket propulsion systems, pose unique challenges due to their exposure to both extremely low temperatures and high pressures. The transition from metallic tanks to composite materials ushers in unparalleled weight advantages for aerospace vehicles. Traditionally, the fabrication of these tanks with composite materials has relied on expensive, specialized materials and intricate manufacturing techniques. However, this study has explored the feasibility of producing carbon-reinforced (CFRP) composite cryogenic liquid oxygen tanks using readily available and low-cost materials, opening up new possibilities for cost-effective and sustainable aerospace applications.

The study initiated with a comprehensive investigation into the material properties of various epoxy resins, evaluating their mechanical performance under cryogenic conditions and their compatibility with liquid oxygen. This assessment proved to be crucial in identifying suitable materials that could withstand the harsh environment of cryogenic liquid oxygen storage.

Recognizing the limitations of relying solely on commercially available epoxy systems, the study embarked on a collaborative effort with local producers to develop domestic epoxy formulations suitable for cryogenic applications. This initiative aligns with the broader goal of fostering nationalization and self-reliance in the field of aerospace materials.

The study's exploration of the epoxy molecular structure and its influence on cryogenic behavior provides valuable insights into the underlying mechanisms that govern the performance of materials at extremely low temperatures. This understanding is essential for developing new and improved epoxy formulations tailored for cryogenic applications.

Through laminate-based testing, a deeper understanding of mode-II damage type in cryogenic environments has been gained. Fractography images revealed the distinct characteristics of cryogenic damage, highlighting the differences from room temperature damage modes with varying epoxy systems. This knowledge is crucial for

predicting and preventing damage in cryogenic systems. The study's findings extend beyond the area of cryogenic liquid oxygen tanks, offering broader insights into the behavior of materials under cryogenic conditions.

Next, the study delved into the development of production techniques tailored for the fabrication of composite cryogenic liquid oxygen tanks. Two distinct tank structures were evaluated: with Liner-Type-II and Linerless-Type-V. The Type-V tank configuration, in particular, received significant attention, within the study refining and optimizing its production processes to ensure consistent quality and reproducibility.

To support the experimental investigations, a series of analytical and FEA calculations were performed. These computational simulations provided valuable insights into the stress distribution and structural behavior of the tanks under various loading conditions. Additionally, an in-house calculation method was developed to bridge the gap between micro and macro scales, enabling a more accurate assessment of the material behavior at the microscale for each constituent. The well known material system IM7-977-3, commonly used in cryogenic applications, compared with conventional epoxy systems using micro calculations. This comparison revealed the distinct advantages of the IM7-977-3 system in terms of its ability to withstand cryogenic temperatures and maintain structural integrity. Also, it was provided potential conventional candidate to substitute this system.

The establishment of test capabilities at the sample and prototype level represents a significant milestone in the study's achievements. The study equipped laboratory and field facilities with the necessary infrastructure to conduct comprehensive testing of cryogenic systems, paving the way for future advancements in cryogenic tank technology.

In tandem with the experimental efforts, study provided increase in design and analysis skills, gaining expertise in the intricate aspects of composite tank technology. This expertise will undoubtedly prove invaluable in the development of future generations of cryogenic tanks.

Furthermore, the study shed light on the limitations of tank with liner systems, demonstrating their unsuitability for cryogenic applications. This finding underscores

the importance of careful material selection and design considerations when developing cryogenic tanks.

Finally, the study critically evaluated the negative effects of the wet filament winding method on production quality. By identifying these drawbacks, researcher paves the way for the development of alternative production techniques that can ensure consistent quality and minimize defects.

In conclusion, the study has made significant contributions to the development of cryogenic liquid oxygen tanks using readily available and low-cost materials. By exploring novel materials, production techniques, and analytical methods, study has expanded the horizons of cryogenic tank technology, opening up new avenues for cost-effective and sustainable aerospace applications. The study's findings serve as a valuable foundation for future advancements in this critical field.

2. RESIN PERFORMANCE UNDER CRYOGENICS

As declared in literature, the constituent behavior and interaction with each other under cryogenic environment is crucial. For that reason epoxy and composite laminate studies conducted both under room and cryogenic temperatures.

2.1 Material Procurement

Initial studies focused on examining the behavior of epoxy under both room temperature and cryogenic conditions. To achieve this, nine different epoxy systems were procured from three distinct manufacturers (EPO-TEK® Epoxy Technology, USA; CET Kompozit ve Epoksi Teknolojileri A.Ş, TR; Huntsman International LLC, UK), each possessing diverse thermomechanical properties. The selection of nine epoxy types was based on considerations of cost and accessibility. Tables 2.1 and 2.2 present detailed information on all the epoxy systems.

Table 2.1 : Purchased epoxy systems.

Epoxy System	Origin	Manufacturer	Main Industries	Cost Unit
EPOTEK 301-2	Belgium	EPOTEK	Optic, Electronic	High
EPOTEK 301-2FL	Belgium	EPOTEK	Optic, Electronic	High
EPOTEK T7110	Belgium	EPOTEK	Optic, Electronic	Very High
EPOTEK T7109-19	Belgium	EPOTEK	Optic, Electronic	High
CE-A 1565 / CE-B 1971 / CE-S 700	Turkey	CET-TECH	Industrial	Moderate
CE-A 11546 / CE-B 13447	Turkey	CET-TECH	Industrial	Low
CE-A 105025 / CE-B 105025	Turkey	CET-TECH	Aerospace	Low
HUNTSMAN ARALDITE 1564-3474	UK	HUNTSMAN	Industrial	Moderate
HUNTSMAN ARALDITE 1564-917-960	UK	HUNTSMAN	Industrial	High

The primary considerations for epoxy systems include viscosity for filament wetting, pot life, and gel time for efficient manufacturing, stress/strain properties to meet mechanical requirements, and thermal properties for cryogenic behavior. Resin types intended for electronic system applications were chosen based on their low glass transition temperature (T_g) and varying viscosity properties. Two-component structural resin systems with amine hardeners were preferred for their accessibility and

low viscosity. Additionally, three-component structural resin systems with anhydride hardeners were selected for comparison with amine hardener systems, particularly concerning cryogenic performance.

Table 2.2 : Properties of purchased epoxy systems.

Epoxy System	Hardener Type and Mix Ratio by Weight	Pot Life @ 23 C	Nominal Curing Cycle	Viscosity (23˚C - 100rpm)	Elasticity Modulus @RT (MPa)	T_g (˚C)
EPOTEK 301-2	Amine (100:35)	8 hours	80˚C/ 3h	225-425cPs	2060	>80
EPOTEK 301-2FL	Amine (100:35)	10 hours	80˚C/ 3h	100-200cPs	3100	>45
EPOTEK T7110	Amine (10:1)	3.5 hours	80˚C / 2h	1400-2200cPs	5440	>40
EPOTEK T7109-19	Amine (100:15)	2 hours	80˚C/ 2h	40000-70000cPs	206	>40
CE-A 1565 / CE-B 1971 / CE-S 700	Anhydride (100:90:0.5-2)	1-3 hours	90˚C/1-3h + 120˚C/ 4 8h	600-900 cPs	3100-3300	125-145
CE-A 11546 / CE-B 13447	Amine (100:26)	4 hours	80˚C/ 1h +120˚C/ 4h	350-450 cPs	2750-2900	115-120
CE-A 105025 / CE-B 105025	Polyamines (100:38)	1.5 hours	23˚C/ 1d + 50˚C/ 15h	500-700 cPs	3450-3650	52-134
HUNTSMAN ARALDITE 1564-3474	Amine (100:26)	3-4 hours	80˚C/ 1h + 120˚C/ 4h	350-450cPs	2750-2900	115-120
HUNTSMAN ARALDITE 1564-917-960	Anhydride (100:98:3)	80-90 hours	80˚C/ 4h + 120˚C/ 4h	450-700Ps	3100-3200	88-120

2.2 Mechanical and Thermal Characterization of Thermosetting Resins

2.2.1 Thermal analysis

2.2.1.1 Thermoset curing

Uncured thermoset polymers typically consist of a combination of monomers and hardener molecules. The curing process, characterized by the exothermic formation of longer chains and branches from linear monomers, initiates the creation of an interconnected network with infinite molecular mass, as illustrated in Figure 2.1. Gelation, a crucial phase, denotes the irreversible shift from a liquid to an elastic gel state. This transition occurs as new chemical bonds form between monomers during the curing reaction.

Gelation serves as a defining feature of thermoset materials, representing the early stages of crosslinked network formation. As the curing process advances, thermosets gradually lose their ability to flow, eventually reaching a point where further changes come to a halt. Importantly, the curing rate remains constant during gelation,

unaffected by the ongoing cure reaction. Ultimately, this intricate process culminates in the creation of fully cured and rigid structures as the reaction progresses beyond the gel point [34,35].

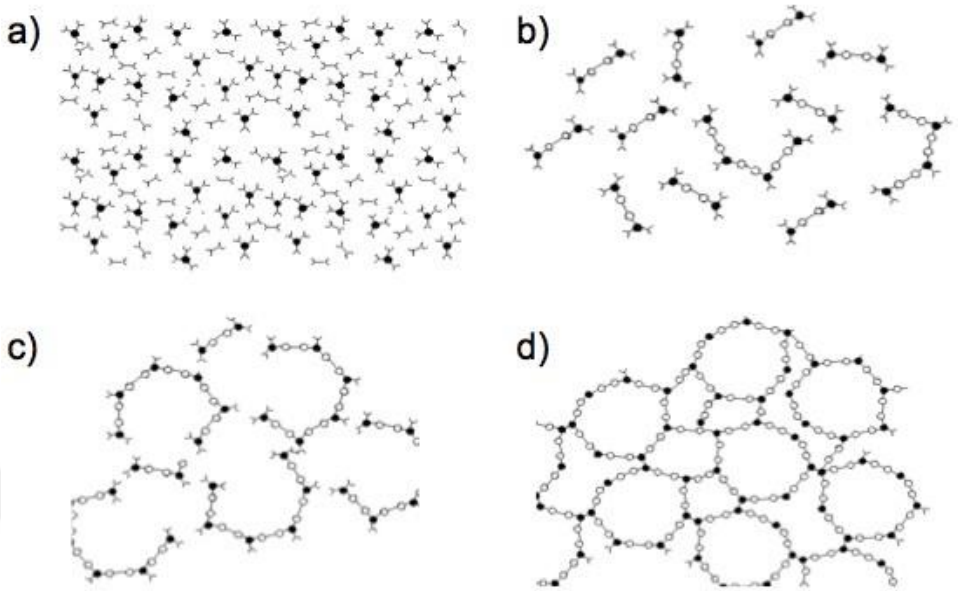

Figure 2.1 : Curing of thermosets a) Monomers b) Linear expansion and branching c) Crosslinked network structuring (not completed) d) Completely cured thermoset [34].

Epoxy resin, a widely employed thermoset polymer, is known for its distinctive structure, featuring at least two oxirane rings (C_2H_4O) or epoxy groups. These epoxy groups are recognized for their high reactivity, attributed to the inherent ring strain. In the curing process, epoxy groups engage in reactions, both intramolecularly with themselves and intermolecularly with other groups, resulting in the formation of intricate crosslinked networks. As illustrated in Figure 2.2, a nucleophilic attack on the terminal carbon (C-O) induces bond cleavage, leading to the opening of the oxirane ring [36,37].

During curing, primary amine groups present in the hardener interact with epoxy, leading to the formation of secondary amine groups. The subsequent reaction involves these secondary amine groups reacting with the residual epoxy resin, as depicted in Figure 2.3. Simultaneously, the interaction between the hydrogen of secondary amine and epoxy produces hydroxyl groups, facilitating the creation of ether links through a process known as etherification (shown in Figure 2.4). However, in cases where there is an excess of epoxy rings or a low activity of amine groups, etherification may compete with the primary curing reaction. To prevent such situations, it is imperative

to carefully consider the cure temperature and maintain the stoichiometric ratio of the epoxy/amine system [34,36]. Furthermore, the creation of secondary alcohols and hydroxyl groups can speed up the total cure reaction, giving additional reactive sites in the process.

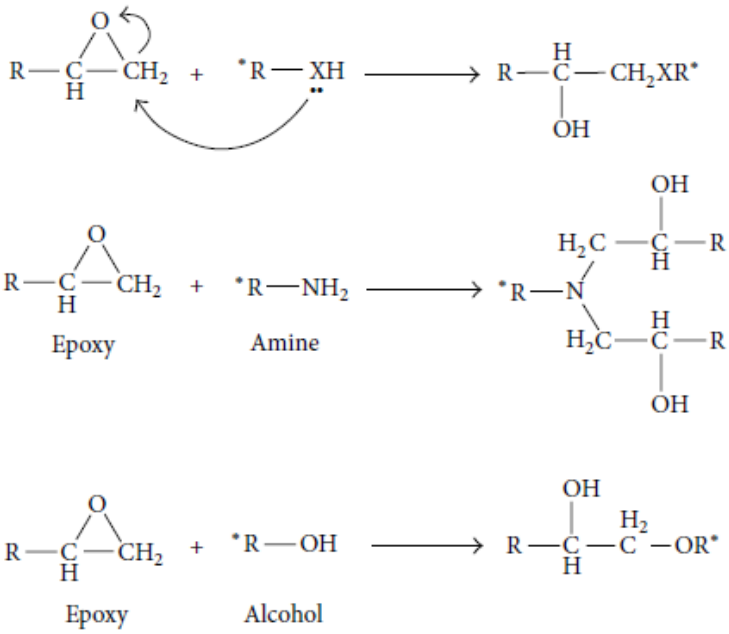

Figure 2.2 : Nucleophilic addition and oxirane opening mechanism [36].

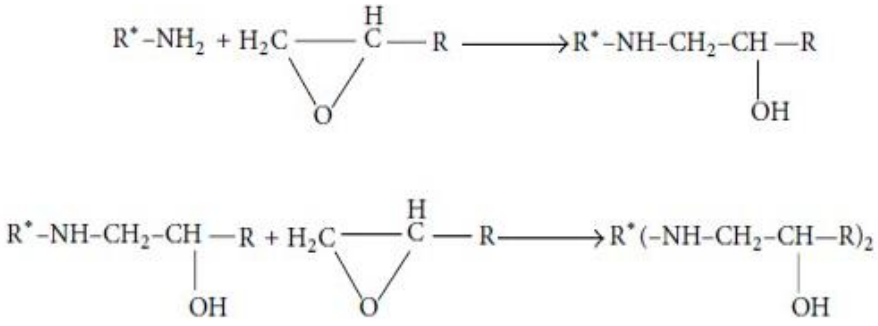

Figure 2.3 : Curing with amine-based hardeners [36].

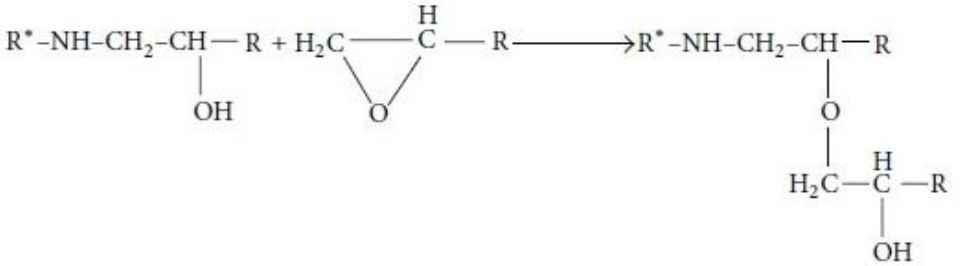

Figure 2.4 : Etherification reaction [36].

The enthalpy value of the reaction (ΔH) is determined by the area under the exothermic crosslinking curve, and as the reaction progresses and the system undergoes partial curing, the necessary enthalpy for completing the cure process (residual enthalpy, (ΔH_r)) is anticipated to reduce. The partial cure degree can be assessed by calculating the area under the exothermic curve after the isothermal process, as described in Equation 2.1 for isothermal cure analyses [34]. Equation 2.1 is employed for calculating the degree of cure in isothermal cure analyses.

$$\alpha = \frac{\Delta H - \Delta H_r}{\Delta H} \tag{2.1}$$

Within this equation, the variable α is employed to denote the degree of cure pertinent to partially cured systems undergoing isothermal temperatures. The symbol ΔH represents the enthalpy of the reaction, as determined through dynamic measurements, and ΔH_r indicates the requisite enthalpy amount needed to finalize the cure reaction following the isothermal process [34].

2.2.1.2 Crosslinking and mechanical response

Crosslinking reaction is process of 3D network formation due to chemical bonding occuring between resin and hardener molecules. Transformation is governed by stiochiometric ratio of both reactants, curing time and curing temperature. As depicted in Time-Temperature-Transformation (TTT) diagram below (Figure 2.5a) it exists several pathways for transformation from liquid phase to solid phase determined by the nature of crosslinking at the end of phase transformation.

Glass transition temperature (T_g) is an important parameter to be investigated as it reflects the transition temperature from solid to rubbery phase in thermosetting materials after which mobility of formed crosslinked structure increases which causes a relaxation in the solid structure. As depicted in Figure 2.5b this transition may cause significant reduction in the elastic properties of thermosetting resins. In the similar figure the transition difference between a highly crosslinked and lightly crosslinked solid to rubber is shown where relaxation for lightly crosslinked 3D netwoks is higher than highly crosslinked structure (Figure 2.6).

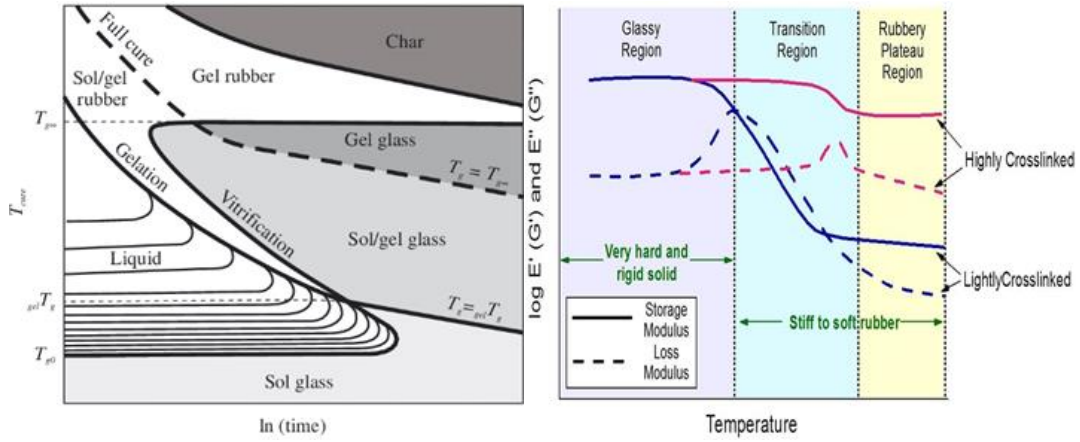

Figure 2.5 : TTT diagram (a) and thermoset transition curve(b).

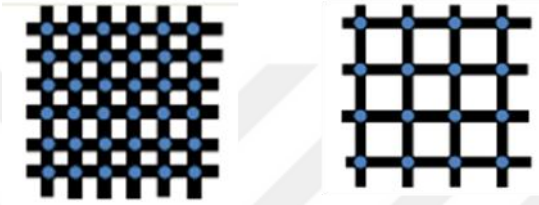

Figure 2.6 : Highly and lightly crosslinked structure demonstration.

In composite materials, resin phase is an important constituent that is responsible of load transfer between reinforcing fibers. From a very simple perspective, a simple rule of mixtures suggests that the elastic properties of a composite material is a factor of constituent volume fractions and elastic modulus values (Equation 2.2).

$$E_c = E_f * V_f + E_m * V_m \tag{2.2}$$

When considered with above mentioned elastic property dependency on the nature of crosslinking, it can be concluded that the mechanical response of any composite structure is dependent on how the resin phase has been processed. In other words, Young's modulus of composite materials made out of highly crosslinked and lightly crosslinked will be different. This feature is of crucial importance when determining the mechanical response of any composite pressure vessel (large scale structure) that is a result of rather robust and large scale manufacturing where ideal conditions for a proper crosslinking may not be achieved. From this perspective curing behavior was analyzed in two different steps that would pave way to better understanding of mechanical repsonse of epoxy systems under cryogenic conditions:

- Determination of maximum glass transition temperatures before testing

- Curing quality control via Differential Scanning Calorimetry (DSC) analysis of tested solid samples

2.2.1.3 Crosslinking and cryogenic temperatures

Cryogenic behavior is higly dependent on the available free space and free volume in 3D network structure. When subjected to cryogenic environment the mobility of crosslinked network significantly reduces which subsequently causes an increase in the binding intermolecular forces [38]. At a larger length scale, extreme cooling results in the reduction of free volume available in 3D network structure that may suppress the stress relaxation (Figure 2.7) [38].

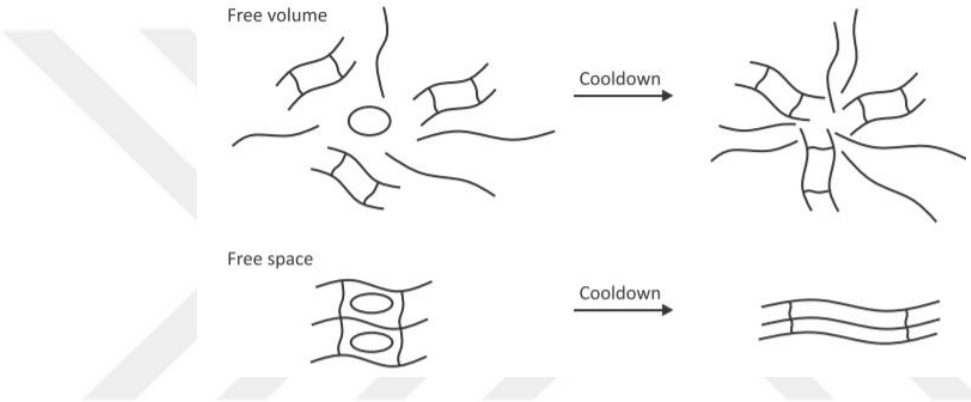

Figure 2.7 : Exemplification of free volume and free space [38].

2.2.1.4 Ideal liquid to solid transition (dynamic DSC scans)

In order to demonstrate above approach two cases of experiments were performed on selected resin samples in DSC. In first set, resin and hardener components were introduced to DSC in liquid form (prior curing) and curing reaction was performed with a dynamic temperature increase rate of 5°C/min up to 250°C in liquid nitrogen (LN2) environment. As depicted in Figure 2.8, typical exotherm curves for thermosetting resins were obtained.

The enthalpy value of the reaction (ΔH) can be determined by calculating the area under the exothermic crosslinking curve. Each resin type has given a different exotherm curve depending on its interaction with their hardener. Total enthalpy of curing values are reported in Table 2.4. This energy value is considered as the enthalpy required for a complete crosslinking with perfect 3D network structure since it has been performed under ideal conditions. At the end of the first heating cycle thermoset samples are %100 cured and in solid form. Obtained solid samples (still in DSC) are

than cooled back to −25^{0}C and re-heated again to 250°C now to determine their maximum glass transition (T_{gmax}). As depicted in Figure 2.8, it does not exist any type of exotherm which confirms that liquid samples were totally transformed into solid. Instead, T_g of obtained solids are now obtained as secondary transition differentiated by the slope change in heat vs temperature curves. T_{gmax} values are also reported in Table 2.4. Except highly thixotropic 7109 and 7110 resins all of the samples showed a smooth transition due to molecular relaxation. Absence of such peaks may be related with the relatively high heating rate. Similarly these two types of resins exhibited a slow reaction enthalpy upon solidification signaling the fact that EPOTEK 7109 and 7110 resins loosely change their molecular structures upon crosslinking reaction. That may be attributed to the presence of already crosslinked (possibly an elastomer like) component in resin formulation.

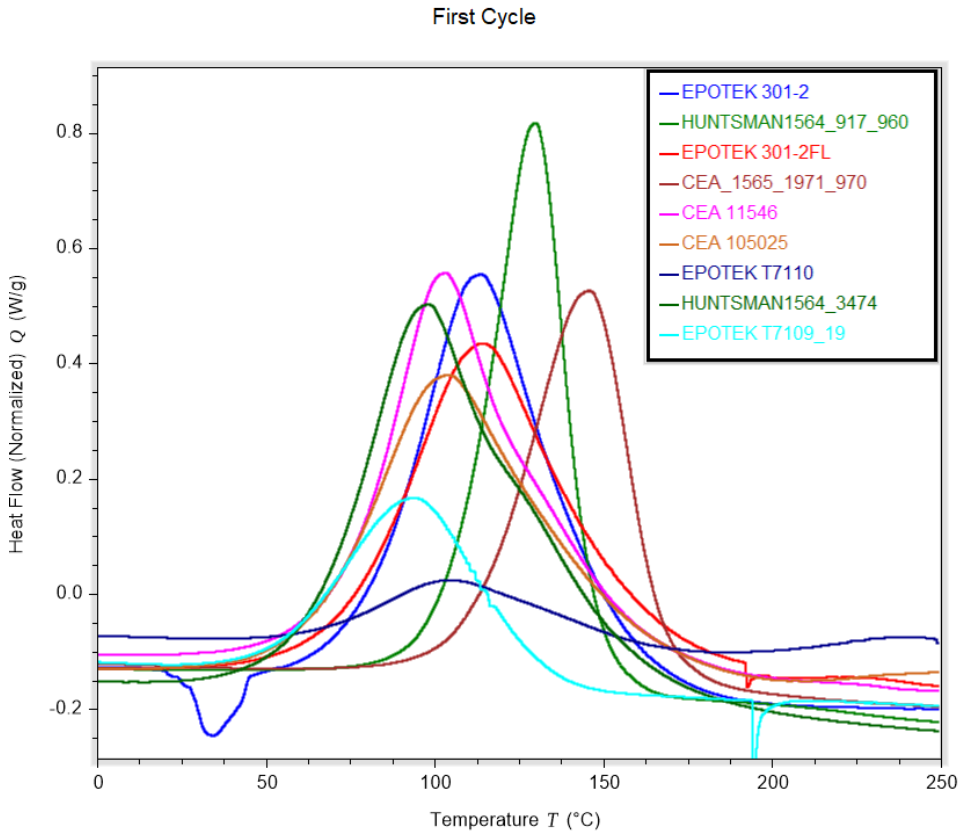

Figure 2.8 : Typical exotherm curves for thermosetting resins.

2.2.1.5 Specimen preparation

The data sheets for the specified resin systems (refer to Table 2.1) served as the foundation for preparing resin mixtures. Before engaging in stoichiometric mixing, each sample underwent a gentle mixing process lasting 15 minutes to improve the

homogeneity of the resin/hardener/initiator components. Subsequently, these well-mixed formulations were carefully placed into pre-prepared silicon molds, which were created in line with the ASTM D790-17 standard [39]. The nominal sample dimensions are 56x12.8x3.2 mm (Figure 2.9).

Figure 2.9 : Three-point bending tests specimens.

Liquid samples are than subjected to step wise curing steps again as suggested by supplier data sheets (Table 2.3) in a temperature controlled oven.

Table 2.3 : Applied Curing Steps for liquid samples.

Epoxy System	Curing Cycle
EPOTEK 301-2	80˚C - 3h
EPOTEK 301-2FL	80˚C - 3h
EPOTEK T7110	80˚C - 2h
EPOTEK T7109-19	80˚C - 2h
CE-A 1565 / CE-B 1971 / CE-S 700	90˚C - 3h+ 90˚C – 4h+ 8h 120˚C
CE-A 11546 / CE-B 13447	80˚C - 1h+ 120˚C - 4h
CE-A 105025 / CE-B 105025	23˚C - 1d + 90˚C - 15h 50˚C
HUNTSMAN ARALDITE 1564-3474	80˚C - 1h+ 120˚C - 4h
HUNTSMAN ARALDITE 1564-917-960	80˚C - 4h + 120˚C - 4h

2.2.1.6 Applied liquid to solid transition

In the scope of crosslinking discussion, application of these curing receipts is supposed to result in epoxy specimens having T_g's close to their maximum T_g. Since it is nearly impossible to mimic the testing conditions in DSC, formed crosslinking structures due to manufacturing may be different. It may exist two type of defects due to crosslinking reaction in thermosetting resins.

Firstly, applied temperature and time may not be sufficent for complete crosslinking leaving some chemically unreacted groups inside the solid specimen. This incomplete crosslinking is typically chareacterized by the appearance of excess exothermic heat in heating cycle of solidifed specimens (See Figure 2.10 EPOTEK 7109-19).

If the curing is complete (no excess heat is observed in solidified samples) a lower T_g than maximum glass transition temperature would suggest that formed solid structure has a relatively low crosslinking density.

Except EPOTEK 7109-19 samples, all of the tested samples have achieved a complete chemical crosslinking and have characteristic T_g values that are reported in Table 2.4. The crosslinking quality of manufactured samples may be expressed as the ratio of their manufactured T_g and T_{gmax}.

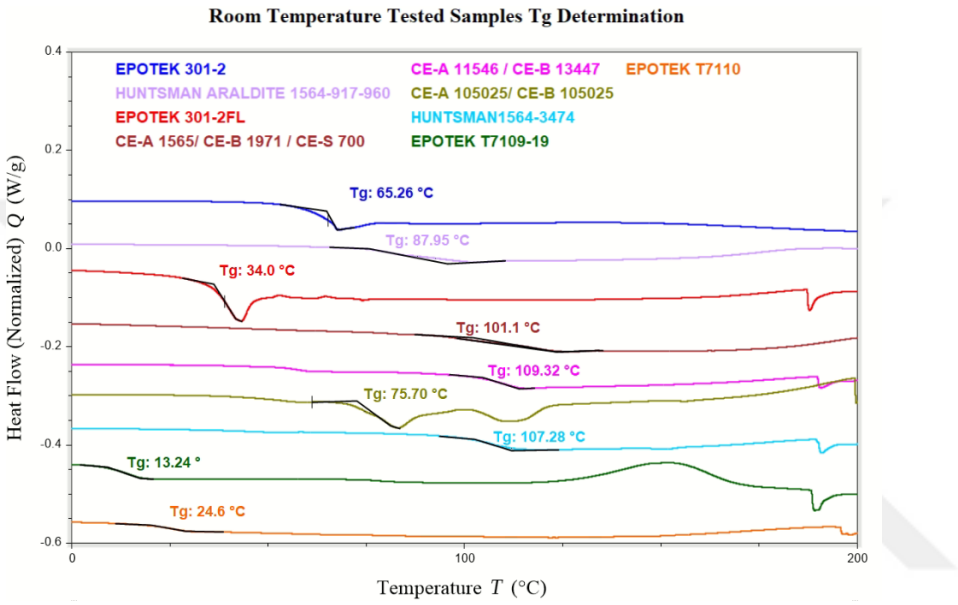

Figure 2.10 : DSC heating cycle graph of all epoxy system specimens tested under room temperature.

Table 2.4 : Thermal characteristics of epoxy system at room and cryogenic temperatures

Epoxy system	Manufacturer, T_g, ˚C	Enthalpy, J/g	Ultimate Glass Transition, (˚C)	Test Specimen T_g , ˚C	Crosslink Quality
EPOTEK 301-2	>80	430.5	67.1	65.3	0.97
EPOTEK 301-2FL	>45	402.2	39	34	0.87
EPOTEK T7110	>40	78.2	-	24.6	-
EPOTEK T7109-19	>40	179.4	-	13.2	-
CE-A 1565 / CE-B 1971 / CE-S 700	125-145	145.7	112.7	101.1	0.9
CE-A 11546 / CE-B 13447	115-120	454	114.4	109.3	0.95
CE-A 105025 / CE-B 105025	120 - 134	465	119.4	75.7	0.63
HUNTSMAN ARALDITE 1564-3474	115-120	482.9	118.4	107.3	0.9
HUNTSMAN ARALDITE 1564-917-960	120-130	341	106.9	88	0.82

Crosslinking quality measurements suggested that CE-A 105025 / CE-B 105025 has the lowest crosslinking density among other resin types that suggests that its 3D network formation is highly susceptible to manufacturing conditions. However, this case may be advantegous to provide information on how Tg changes upon cryogenic temperature application since its less connected network structure maybe disturbed even more.

2.2.2 Mechanical tests

2.2.2.1 Three-point bending tests

Three-point bending tests were performed according to ASTM D790-17 [39]. These tests were carried out for two conditions: room temperature and liquid nitrogen temperature. By this way, the mechanical performances of epoxies at room temperature and cryogenic temperatures were compared. In order to perform the tests novel testing grips were in house manufactured. CAD desing and test performing can be seen in Figure 2.11 and 2.12, respectively.

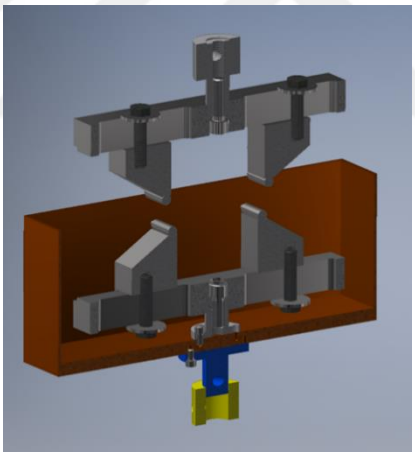

Figure 2.11 : Three-point bending test jaw and cryogenic dewar.

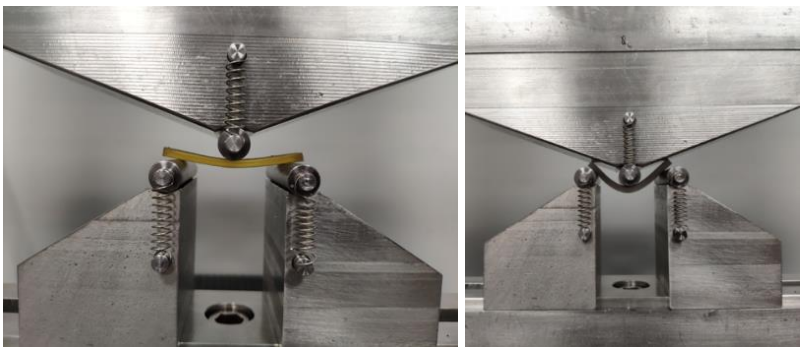

Figure 2.12 : Three-point bending test of a) T7109-19 epoxy system b) CE-A 1565 / CE-B 1971 / CE-S 700 epoxy system under room temperature

By means of this test, following mechanical properties of epoxies at room temperature and under cryogenic temperature were obtained;

Flexural Strength (σ_{fM}): Equation 2.3 is utilized to determine the maximum flexural stress experienced by the test specimen in a bending test [39]:

$$\sigma_{flex} = 3PL/2bd^2 \tag{2.3}$$

Where;

σ_{flex} = stress in the outer fibers at midpoint, MPa

P = load at a given point on the load-deflection curve, N

L = span length between supports, mm

b = beam width, mm

d = beam depth, mm

Flexural Strain, ε_f : Equation 2.4 is employed to calculate the nominal fractional change in the length of an element situated on the outer surface of the test specimen at midspan, where the maximum strain is encountered, and this calculation is applicable for any given deflection [39]:

$$\varepsilon_{flex} = 6Dd/L^2 \tag{2.4}$$

Where;

ε_{flex} = strain in the outer surface, mm/mm

D = maximum deflection of the center of the beam, mm

L = Span length between supports, mm

d = beam depth, mm

Tangent Modulus of Elasticity: The tangent modulus of elasticity, commonly referred to as the "modulus of elasticity," represents the stress-to-strain ratio within the elastic limit. It is determined by drawing a tangent to the steepest initial straight-line segment of the load-deflection curve and applying Eq. 2.5 [39]:

$$E_{flex} = L^3m/4bd^3 \tag{2.5}$$

Where;

E_{flex} = modulus of elasticity in bending, MPa

L = Span length between supports, mm

m = slope of the tangent to the initial straight-line segment of the load-deflection curve is measured in N/mm of deflection

b = beam width, mm

d = beam depth, mm

2.2.2.2 Liquid nitrogen (LN2) submerged tests

The bending tests in the cryogenic environment were carried out by designing a liquid nitrogen container for the test grips. In order to keep the liquid nitrogen in the container, insulation was provided by covering it with XPS foam. Figure 2.13 shows the LN2 submerged 3 point bending test.

Figure 2.13 : LN2 submerged three-point bending test of Epotek T7110 epoxy system.

2.2.2.3 Mechanical test results and discussion

The primary focus of the bending tests was to evaluate the variation in the flexural performance of epoxy samples tested under room temperature (RT) and liquid nitrogen (LN2) environments. A common observation during the mechanical testing revealed that all samples underwent significant embrittlement when subjected to LN2 conditions [40]. This embrittlement is evident in the reduction of flexure strain values and an increase in the flexural modulus of the samples [41,42]. Cryogenic performance is subsequently defined as the maximum flexural stress a sample can endure, directly related to manufacturability (e.g., viscosity) and the resulting macromolecular structure.

Electronic grade epoxy systems (Epotek 7109-19 and Epotek 7110)

When exposed to cryogenic temperatures, the T7109-19 resin specimens demonstrated a notable increase in stiffness (+14800%), strength (+30%), and a decrease in flexibility (−82%) compared to room temperature tests (Table 2.5). Similarly, T7110 specimens exhibited changes of (+3300%), (+400%), and (−96%), respectively (Table 2.5). This finding indicates that the T7109-19 resin is more susceptible to cryogenic embrittlement than T7110, an anticipated outcome linked to the constrained movement of the formed 3D network structures in extremely cold environments [41,43,44]. Notably, the stress-strain curves illustrate distinctively low flexural stress values for T7109-19 (Figure 2.14 and 2.15).

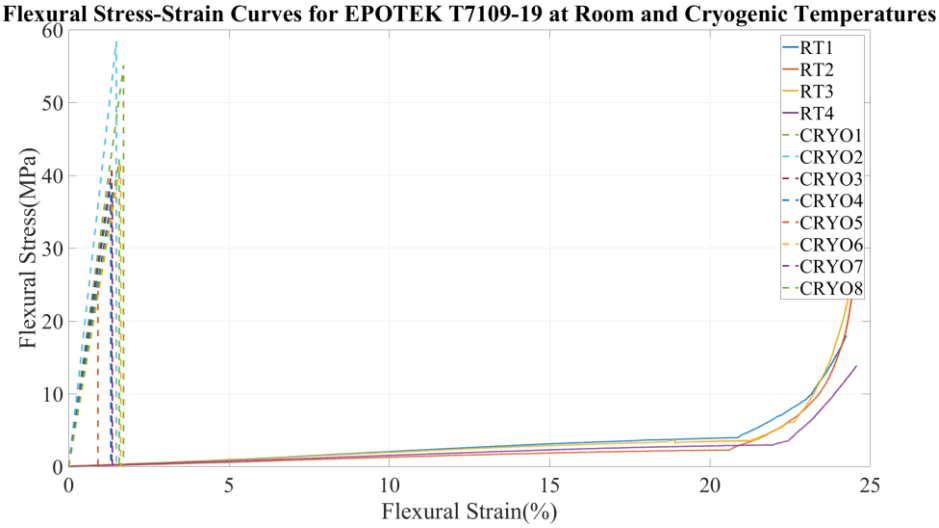

Figure 2.14 : Flexural stress-strain curves for Epotek T7109-19 at room and cryogenic temperatures.

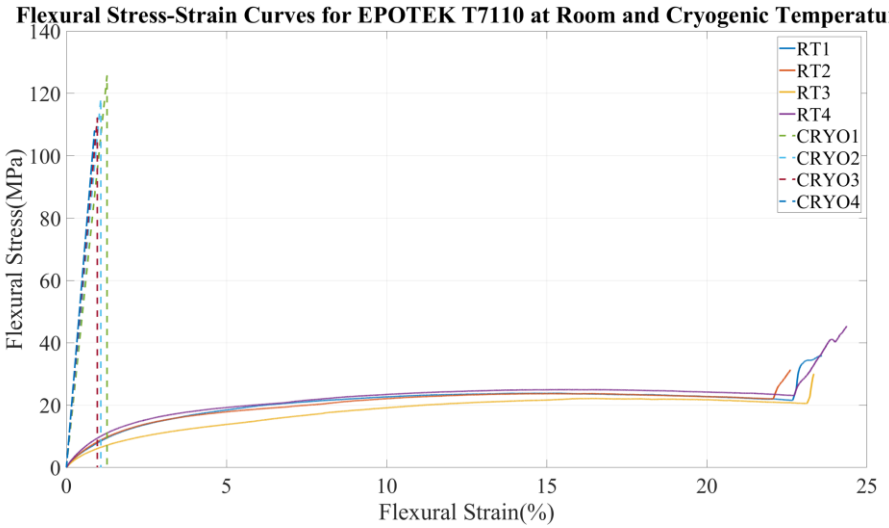

Figure 2.15 : Flexural stress-strain curves for Epotek T7110 at room and cryogenic temperatures.

To comprehend the substantial differences in flexural strength values between the two resins, an examination of the fracture surfaces of the failed samples under cryogenic conditions was conducted. For each set of samples, three fracture surface images are provided to formulate a general comment on the type of failure. As depicted in Figure 2.16, the fracture surfaces of both T7109-19 and T7110 samples appeared very smooth, indicating rapid crack propagation during failure. This observation underscores the pronounced embrittlement effect for these resin types. One notable disparity between the two resins was the increased presence of air bubbles and shape inhomogeneities in the T7109-19 resin. This is attributed to the extremely high viscosity of the T7109-19 resin, leading to manufacturing-related defects.

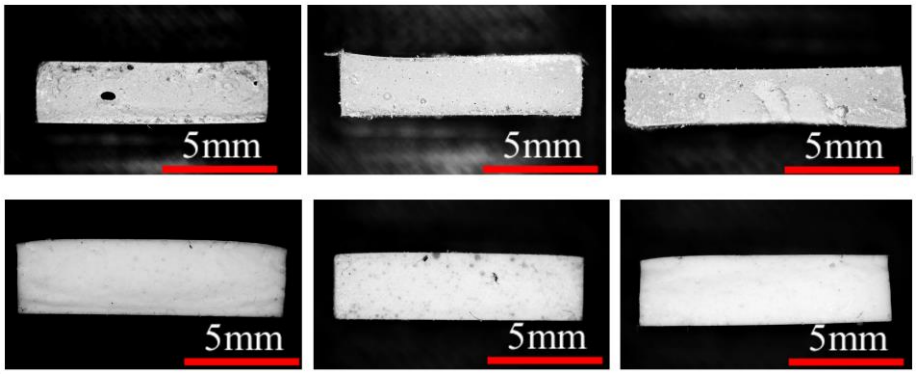

Figure 2.16 : Fracture surfaces of selected samples from Epotek T7109-19 (top row) and Epotek T7110.

In summary, the T7109-19 resin presents processing challenges, is susceptible to microcracking under cryogenic conditions, potentially limiting its suitability for cryogenic applications. However, it is worth noting that these resin types offer the highest flexural modulus among other resin samples, making them a potential preference in applications prioritizing high flexural modulus.

Optic grade epoxy systems (Epotek 301-2FL and Epotek 301-2)

Exposure to cryogenic temperatures resulted in notable changes in the mechanical properties of the 301-2 and 301-2FL specimens (Figure 2.17 and 2.18). In the case of 301-2FL, there was a considerable increase in stiffness (+240%), strength (+215%), and a decrease in flexibility (−26%) compared to tests conducted at room temperature (Table 2.5). Unlike the electronic grades, the 301-2FL resin, despite having similarly low T_g, exhibited a minor effect of cryogenic embrittlement.

A significant difference between 301-2FL and T7109-19 must be addressed at this point, considering the ΔH_{curing} (Table 2.4) and stoichiometric mixing ratios (Table 2.1).

While T7109-19 and T7110 have a suggested stoichiometric ratio of 100:15, it is 100:30 for 301-2FL. The ΔH_{curing} of 301-2FL is almost twice as high as that of T7109-19, indicating that fewer chemical bonds are formed for the solidification of T7109-19. The high viscosity of T7109-19 further suggests that crosslinking occurred between longer macromolecular chains compared to 301-2FL. This comparison is crucial for a better approximation of the cryogenic response of a resin type with given viscosities and T_g values in resin data sheets.

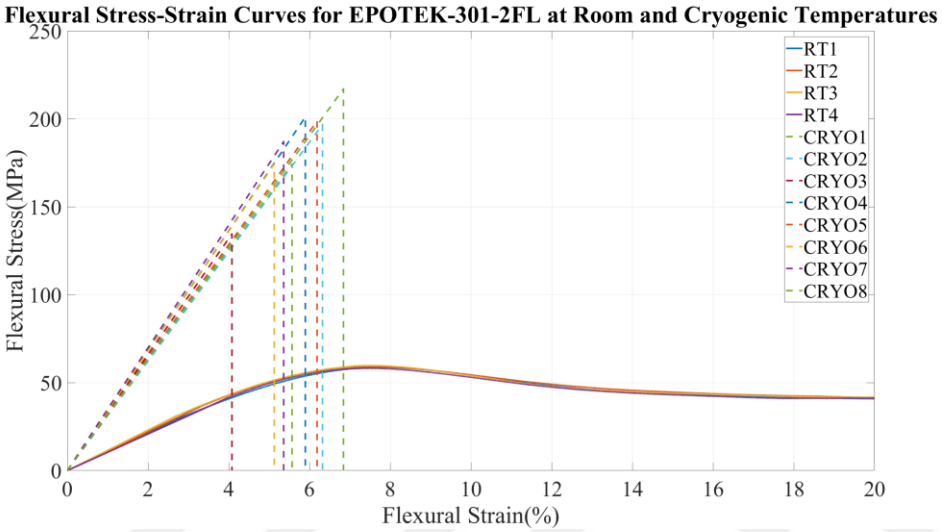

Figure 2.17 : Flexural stress-strain curves for Epotek 301-2FL at room and cryogenic temperatures.

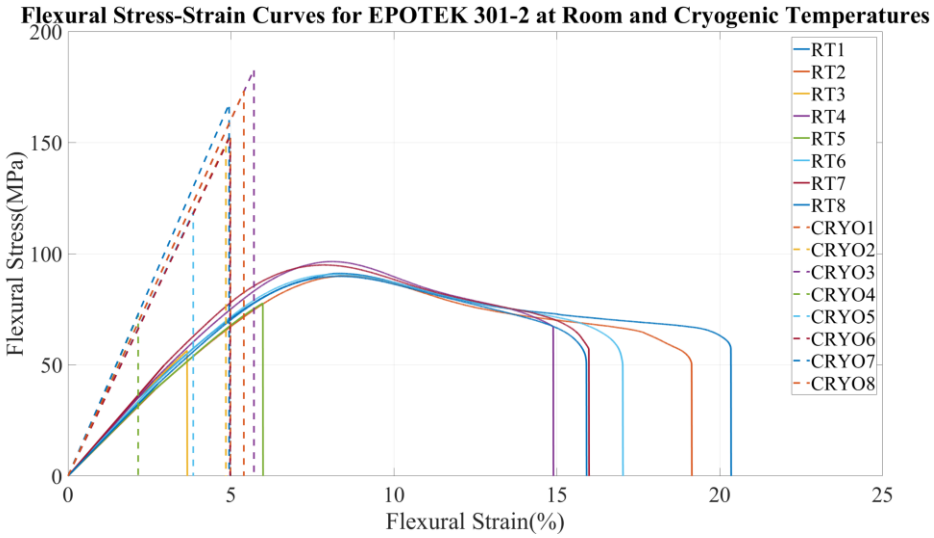

Figure 2.18 : Flexural stress-strain curves for Epotek 301-2 at room and cryogenic temperatures

The primary difference between 301-2 and 301-2FL lies in their Tg values. The higher Tg of 301-2 suggests that the macromolecular structure of this resin is harder to

disturb. This distinction is reflected in the room temperature flexural modulus values of both resins, with 301-2 having a higher modulus.

When exposed to cryogenic temperatures, 301-2 specimens exhibited relatively smaller changes: +136% in flexural modulus, +74% in strength, and −38% in flexural strain (Table 2.5). In comparison with 301-2FL, the 301-2 resin experienced a significant reduction in flexural strain and did not show similar increases in strength and modulus. The rationale behind the varied changes in the mechanical response has been evaluated by comparing the fracture surfaces of the tested samples. As depicted in Figure 2.19, the failure surfaces of the investigated samples are divided into two sections, namely the compression and tension regimes, due to the applied bending load.

The tensile failure regime is typically characterized by the appearance of mirror-mist-hackle formations [45]. In the provided micrographs, this region is the bottom part, where linear hackle lines originating from mirror regions are clearly distinguishable. The compressive regime, on the other hand, is the top part, where very fast crack propagation from the top of the surface towards the tensile failure regime is present. Due to the nature of the bending test, such features usually coincide in the middle of the specimen (neutral axis).

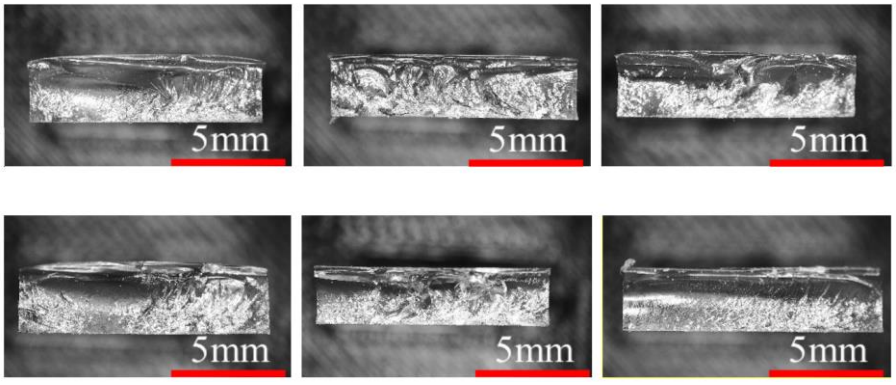

Figure 2.19 : Fracture surfaces of selected samples from 301-2FL (top row) and 301-2 (bottom row)

Three-component structural grade epoxy systems (CE-A 1565 / CE-B 1971 / CE-S 700 and Huntsman araldite 1564-917-960)

The comparison of these two epoxy systems must be approached differently than other systems due to their distinct curing mechanism involving three components. In three-component epoxy systems, the curing reaction is typically initiated by an initiator at an elevated temperature [46]. Anhydrides are commonly used as bulk hardener agents,

becoming reactive beyond 120°C [47]. The crosslinking reaction is usually initiated by a smaller and more reactive amine-based component [46]. The rate of crosslinking is determined by the size of amine-based initiator. As deduced from the difference in pot life between the two resins, the CE system employs a smaller amine (Pot life: 1-3 hours), whereas the Huntsman system employs a larger amine molecule (Pot Life: 80-90 hours). Given the three-component nature, the microstructure of these resins is more dependent on manufacturing conditions than two-component systems. Curing enthalpies and ideal maximum T_g values are similar for both resin systems. However, when subjected to manufacturing conditions, it becomes evident that the Huntsman 1564-917-960 system has a significantly lower T_g compared to the CE-1565 system, suggesting that the 3D network structure of the former is rather loosely connected.

In terms of mechanical performance at room temperature, both resin systems exhibited a similar flexural modulus, whereas Huntsman 1564-917-960 was significantly less strong and less flexible.

When tested under cryogenic conditions (Figure 2.20), it is evident that the Huntsman system drastically suffers from chain immobility, resulting in a reduction in strength, which is dissimilar to previously reported cases. In contrast, the CE system is less affected in terms of flexural strength while losing flexibility, underscoring an important mechanical response that can be achieved from three-component epoxy systems (Figure 2.21).

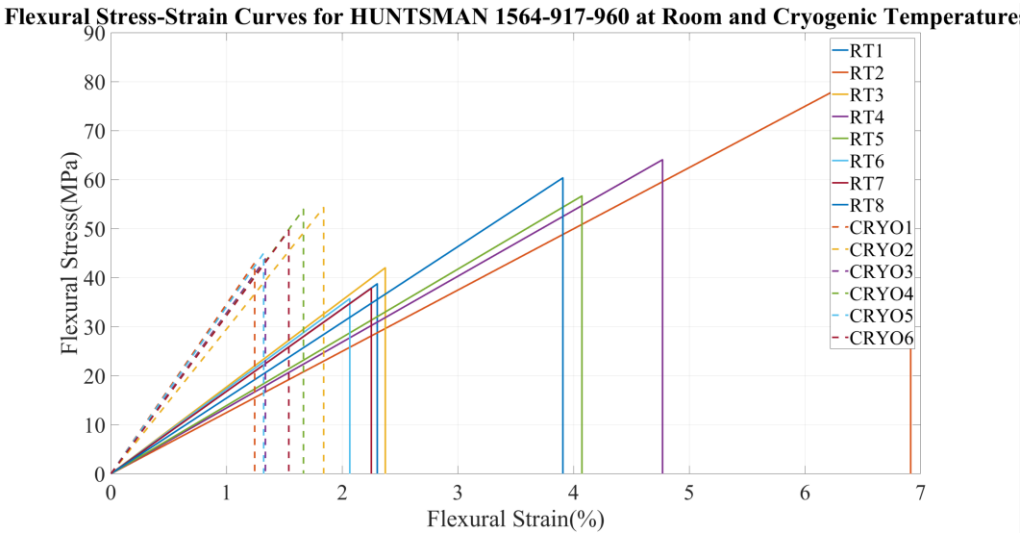

Figure 2.20 : Flexural stress-strain curves for Huntsman 1564-917-960 at room and cryogenic temperatures.

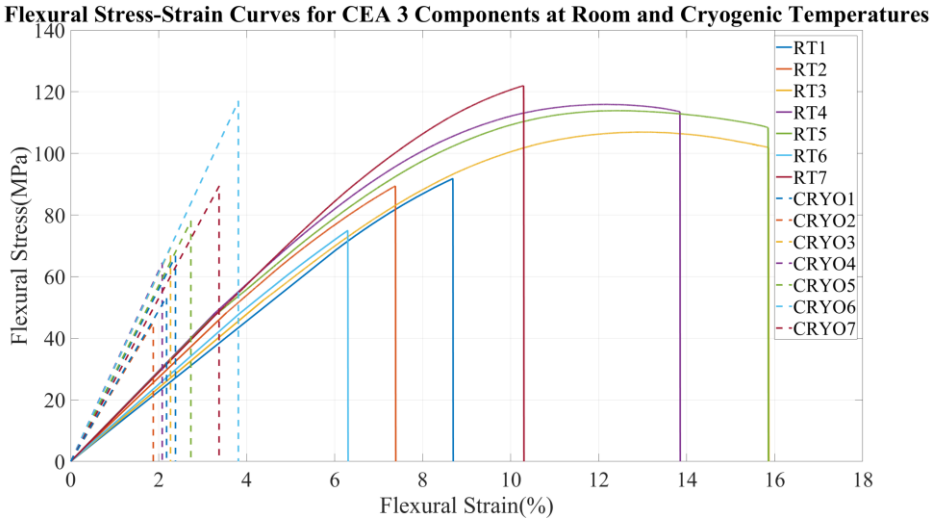

Figure 2.21 : Flexural stress-strain curves for CE-A 1565 / CE-B 1971 / CE-S 700 at room and cryogenic temperatures.

Two-component structural grade epoxy systems (CE-A 11546/ CE-B 13447 and Huntsman araldite 1564-3474)

The CE-A 11546/CE-B 13447 and Huntsman 1564-3474 systems exhibit similar behavior under thermal analysis, sharing identical curing profiles. Furthermore, the mechanical behaviors of the two systems are consistent under both room and cryogenic conditions (Fig. 2.22 and 2.23). In cryogenic conditions, strength increased by around 40%, flexural modulus increased by around 250%, and elongation capability decreased by around 65%. The observed brittle behavior in cryogenic conditions is evident in these epoxies. Overall, these two epoxy systems demonstrate promising results in cryogenic bending tests.

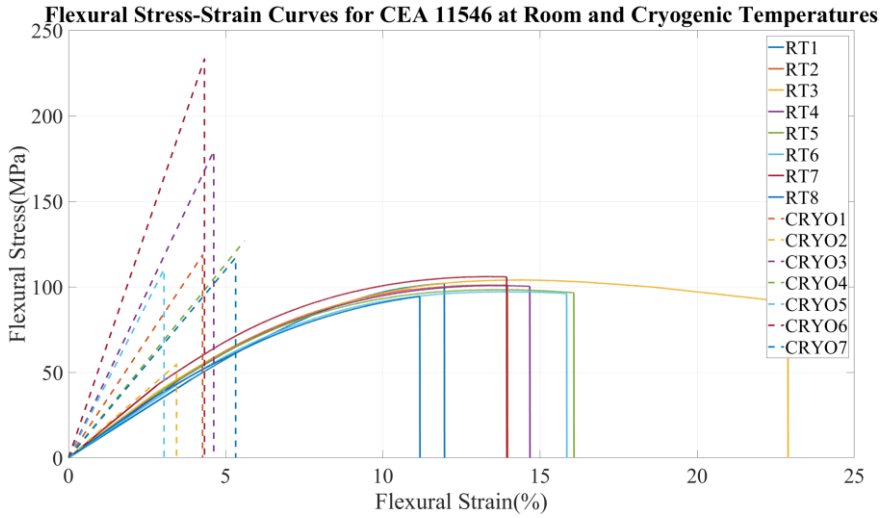

Figure 2.22 : Flexural stress-strain curves for CEA 11546 at room and cryogenic temperatures.

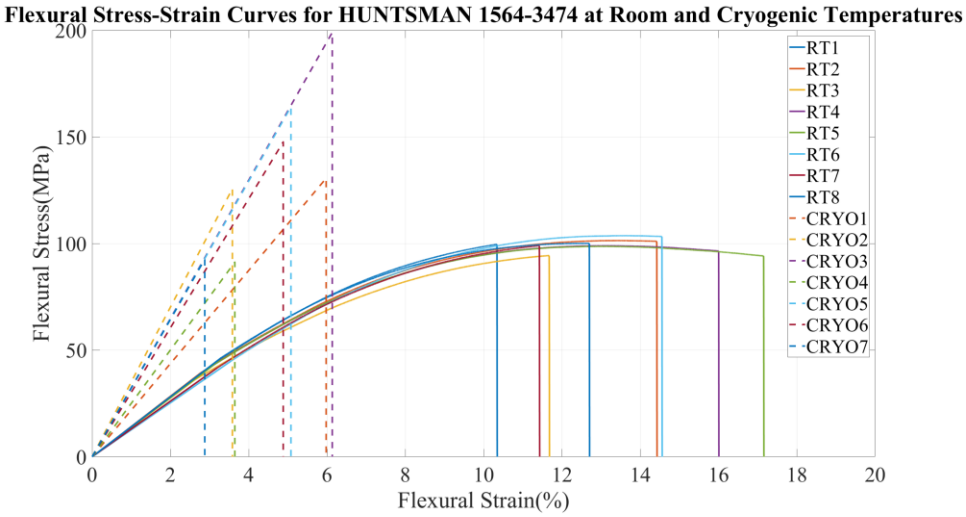

Figure 2.23 : Flexural stress-strain curves for Huntsman 1564-3474 at room and cryogenic temperatures.

Cold curing aerospace grade epoxy system (CE-A 105025 / CE-B 105025)

This system incorporates several different amine hardeners to provide curing capability even at low curing temperatures, allowing curing in a wide range of temperatures from 23°C to 130°C. The behavior of this epoxy changes drastically according to the curing temperature cycle.

The mechanical behavior of this epoxy is average for both room and cryogenic conditions when compared to other tested epoxies. Changes in mechanical properties when subjected to cryogenic conditions are around +67% in strength, −55% in elongation, and 260% in flexural modulus. The mechanical behavior of the CE-A 105025/CE-B 105025 system is illustrated in Figure 2.24.

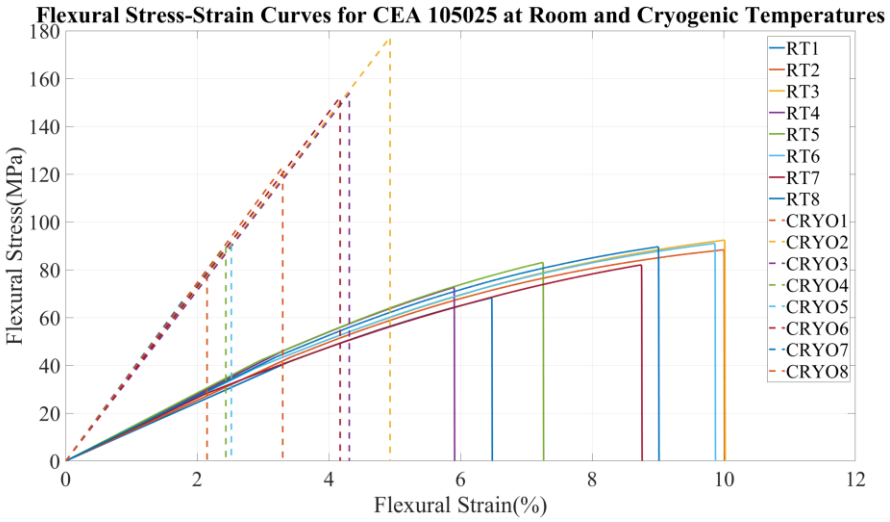

Figure 2.24 : Flexural Stress-Strain Curves for CEA 105025 at room and cryogenic Temperatures.

Table 2.5 : Average flexural test results of the epoxy systems at room and cryogenic temperatures

Epoxy system	RT Test Mechanical Results			LN2 Test Mechanical Results		
	σ_{flex}	ε_{flex}	E_{flex}	σ_{flex}	ε_{flex}	E_{flex}
	MPa	%	MPa	MPa	%	MPa
EPOTEK 301-2	90 ± 6	7.4 ± 1.7	2674 ± 472	157 ± 21	4.6 ± 1.1	6298 ± 929
EPOTEK 301-2FL	59 ± 1	7.7 ± 0.2	1984 ± 465	185 ± 25	5.7 ± 0.8	6745 ± 644
EPOTEK T7110	23 ± 1	22.3 ± 0.7	365 ± 46	116 ± 7	1.0 ± 0.2	12396 ± 1155
EPOTEK T7109-19	32.6 ± 7.6	7.3 ± 0.1	31 ± 7	42 ± 10	1.3 ± 0.6	4622 ± 1312
CE-A 1565 / CE-B 1971 / CE-S 700	102 ± 17	9.9 ± 2.6	2109 ± 344	73 ± 22	2.6 ± 0.7	4180 ± 955
CE-A 11546 / CE-B 13447	100 ± 4	13.2 ± 1.1	765 ± 61	146 ± 26	4.5 ± 1.1	3180 ± 90
CE-A 105025 / CE-B 105025	83 ± 9	8.4 ± 1.6	1012 ± 123	139 ± 32	3.8 ± 0.9	3643 ± 63
HUNTSMAN ARALDITE 1564-3474	99 ± 3	12.4 ± 1.1	1853 ± 237	136 ± 38	4.4 ± 1.1	5741 ± 1265
HUNTSMAN ARALDITE 1564-917-960	52 ± 17	3.4 ± 1.4	2596 ± 461	48 ± 5	1.5 ± 0.2	4445 ± 518

2.2.2.4 Overall comments on mechanical and thermal characterization efforts

The overall results suggest that the mechanical response of epoxy resin systems is highly dependent on their microstructure, which is particularly determined by the quality of manufacturing. This relationship is crucial for selecting and designing desirable epoxy systems to be employed as matrix phases in large structural systems operating under cryogenic conditions. This study does not focus on detailed molecular structure analysis; instead, its aim is to contribute to an evidence-based research approach. Based on the above-mentioned discussion, the following conclusions will pave the way for further epoxy trials:

The presence of particles in the epoxy structure results in structures that are more susceptible to cryogenic conditions in terms of strength and strain properties [42–44]. However, their presence offers significant design capabilities in terms of micro-crack density reduction and improvement in fracture toughness in epoxy systems [48]. It is worth noting that these benefits were not observed for the investigated epoxy types in this study. The properties of particles, such as type and geometrical features, as well as their distribution in the resin phase, are critical factors that determine the performance of mechanical properties under cryogenic conditions [42].

The length and distribution of epoxide monomers are crucial factors as they determine the available free space and volume in specimens, which may negatively impact

cryogenic behavior. Specifically, in terms of flexural performance, larger monomer chains are preferred [42,44,49].

For three-component epoxy systems, the mechanical behavior is largely governed by the crosslinking reaction rate, specifically the size of the amine initiator. Larger amine initiators result in a rather loosely connected 3D network. However, it is vital to underline the fact that resin systems with small initiator molecules have a very short pot life, which may hinder their application in large-scale production.

2.3 Lox Compatibility Tests

In oxygen or oxygen-enriched environments, lower energy inputs and at lower temperatures than in air will cause ignition of fuel-oxygen mixtures. For instance, hydrogen in air needs a minimum spark energy of 0.019 mJ (4.54 x 10-6 cal) at 1 atm [50] to be ignited, but in 1 atm of oxygen this energy for the ignition of hydrogen decreases to 0.0012 mJ (2.8662 x l0e-7 cal) [51].

In an oxygen-rich environment, most polymers and their composites are prone to ignition, making them unsuitable for oxygen applications. The limited polymers deemed compatible with Liquid Oxygen (LOX) include certain fluorocarbons like polytetrafluoroethylene, polychlorotrifluoroethylene, and fluoroethylene. These fluorocarbons are commonly employed in LOX systems for purposes such as seals, gaskets, and lubricants [52]. However, they are not suitable for LOX composite pressure vessels. Consequently, the development of LOX-compatible polymer matrix resins necessitates addressing the inherent compatibility of the polymer matrix with LOX in the initial stages [53,54]. While epoxy resins have found application in various cryogenic fields, cyanate ester, another high-performance matrix resin, exhibits the potential for compatibility with LOX due to its ability to self-polymerize and form a unique triazine ring structure [28].

Nonmetals, for example polymers, generally have ignition points at lower temperatures and pressures than metals; oxygen pressures lower than 7 kPa (1 psia) can cause burning of nonmetals [55].

The Gas Oxygen (GOX) mechanical impact test is typically more sensitive in assessing materials compared to the LOX mechanical impact test due to the elevated pressure conditions. Nevertheless, the LOX mechanical impact test has contributed

significantly to a substantial database for nonmetals, offering valuable insights into their suitability for oxygen service [55].

For tested materials, the mechanical impact test and the pneumatic impact test typically yield the same findings. Because the temperatures attained by adiabatic compression are below the AIT of most polymeric materials, polymeric materials are rarely burned by pneumatic impact at pressures below 1.7 MPa (250 psia). However, at pressures less than 1.7 MPa (250 psia), they may respond as a result of mechanical impact. [55].

Test conditions of mechanical and pneumatic impact are generally more violent than those in actual use. Because of that the data gathered from these tests have a reasonable margin of safety.

In Figure 2.25 pressure sensivity of nonmetallic materials can be seen under oxygen environment.

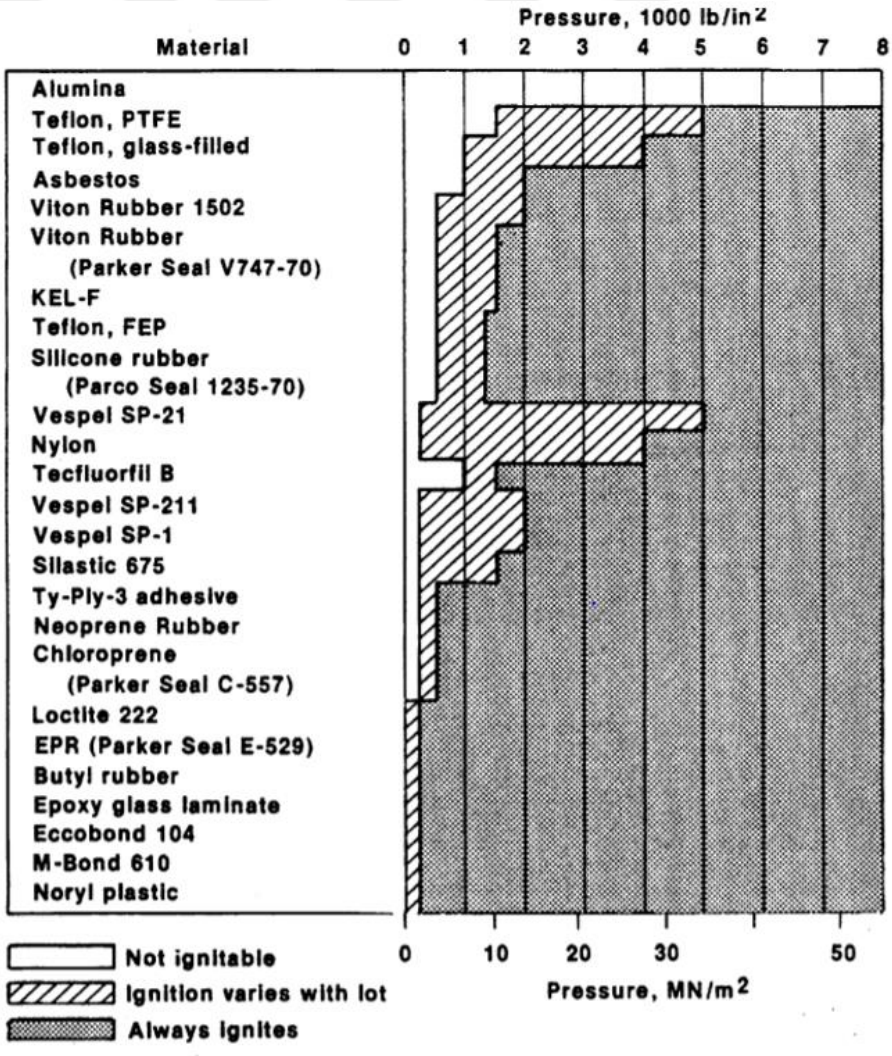

Figure 2.25 : Range of ignitability for nonmetallics [56].

The criteria for selecting a preferred nonmetal for oxygen service include the following [55]:

(a) minimal reactions under mechanical impact testing,

(b) a high Autoignition Temperature (AIT),

(c) a low heat of combustion,

(d) a high oxygen index,

(e) a low flame temperature,

(f) a high threshold pressure

(g) a low burn rate.

2.3.1 Methods applied- LOX impact tester design

A LOX impact test stand has been developed at DeltaV Space Technologies. This setup will be employed to assess the LOX compatibility of parts and materials intended for use in systems containing liquid oxygen. Commonly referred to as the 'ABMA Tester' in the literature, this stand is utilized to determine the tendency of samples to react with liquid oxygen. The CAD view of the stand is depicted in Figure 2.26. During the test, a mass of 9.09 kg is released from a height of 1.1 meters, transferring approximately 10 kg-m (98 J) of impact energy to the sample [29].

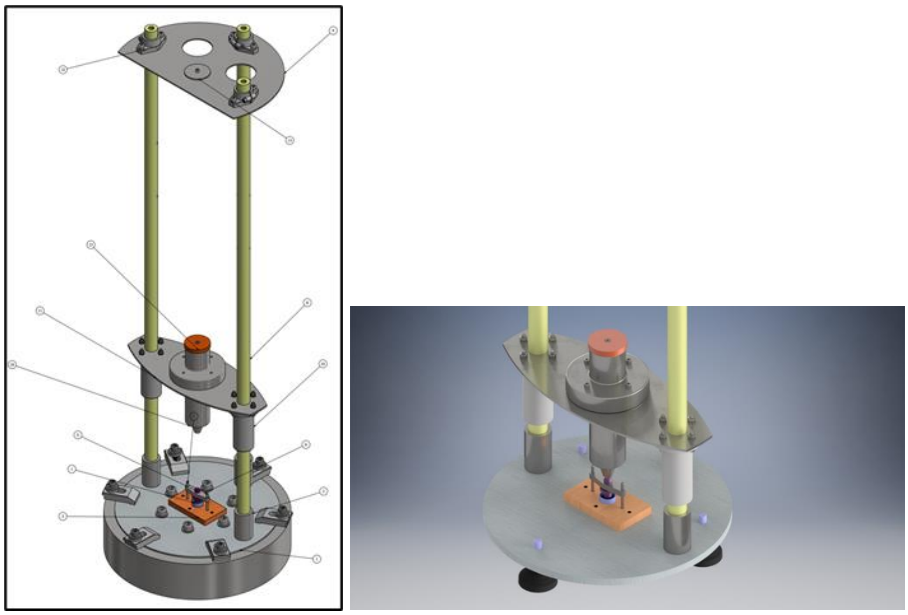

Figure 2.26 : LOX impact tester CAD design view.

In this study, tests were conducted using samples with a diameter of 19mm and a thickness of 1.6mm [29].

2.3.2 Specimen preparation-LOX impact

Previous studies [54,57] have emphasized the crucial role of sample preparation in achieving reproducible test results for LOX impact sensitivity. It has been observed that the impact sensitivity in LOX tests varies with the thickness of the samples, with reactivity generally increasing as the sample thickness decreases. However, this relationship is not universally directly proportional and may, in fact, reverse with certain materials. For instance, in the case of some sheet titanium samples, there seemed to be a trend towards increased reactivity with thicker samples [58]. Determining the intrinsic relationship between thickness and sensitivity to impact is challenging due to the involvement of multiple factors, including sample hardness, flexibility, and ductility at LOX temperatures.

Samples were prepared by casting into Teflon mold. Each epoxy system has been cast according to its curing profile. After the epoxy samples were removed from the mold, oxygen cleaning processes were carried out with the help of an ultrasonic bath (Figure 2.27).

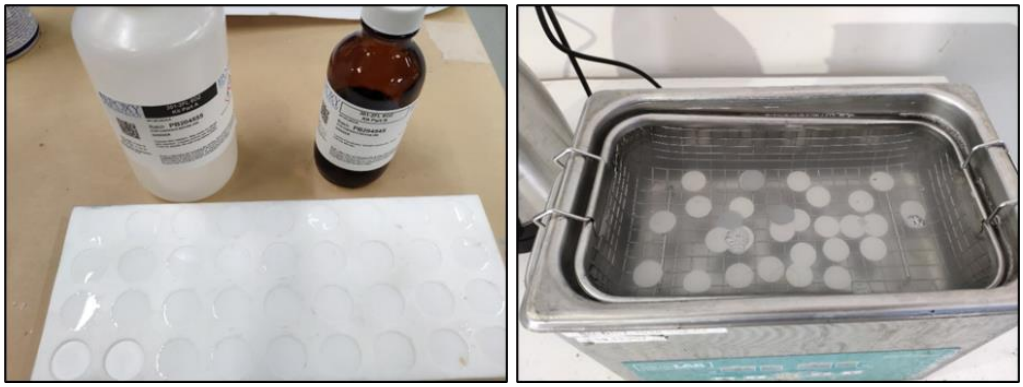

Figure 2.27 : LOX specimen mold and ultrasonic bath oxygen cleaning of specimens

2.3.3 Calibration

ASTM D2512 standard Section 9 [29] states that the free falling time can deviate ±3% from the theoretical value. Theoretical falling time can be calculated as:

$$\Delta t = \sqrt{\frac{2h}{g}} \tag{2.6}$$

Where;

Δt: Falling time (s),

h: Drop height(m),

g: standard earth gravity(m/s^2)

The calibration of the system was verified using a high-speed camera. In this process, when the test system is released from a certain height, the time it takes to fall to the ground is compared with the theoretical free fall time. The system was released from a height of 1.15m, and according to the free fall formula, a decrease of 0.4843 seconds should occur.

The measurements were taken with a high-speed camera at 1057 frames per second (fps). When evaluating the images in a 60 fps video player, 1 second in the video corresponds to 1 / (1057/60) = 0.05676 seconds. The four images captured were examined separately, and the system check was completed successfully.

2.3.4 Test acceptance criteria

The test is repeated for 20 separate coupons. In one of these repetitions, if an indication such as glare or explosion is observed, signifying that the sample is sensitive to LOX, the test is repeated 40 times with new coupons. A sample showing more than one indication can be interpreted as 'oxygen sensitive,' and this material is not used in systems containing liquid oxygen [29]. In addition, the oxygen sensitivity of the sample is evaluated based on "reaction frequency" and "impact sensitivity" [59].

The results gathered can be used to rate materials as follows in Table 2.6, using equations 2.7 and 2.8:

Table 2.6 : Lox impact material rating classifications.

Classification	Definition
S	Considered suitable for Liquid Oxygen (LOX) service when cleaned and/or processed in accordance with applicable Marshall Space Flight Center (MSFC) standards
BT	Deemed satisfactory as mentioned above, with the stipulation that each manufacturer's batch of the product must undergo individual testing and be found acceptable
C	Conditionally evaluated due to insufficient test experience to adequately assess the sample
U	Deemed unacceptable as it has the potential for vigorous burning or exploding upon contact with Liquid Oxygen (LOX)

Furthermore, the sensitivity of materials to mechanical impact increases with pressure. Given that this test is conducted at atmospheric pressure, it does not fully reflect the LOX sensitivity of the material under operating conditions involving pressure [29].

$$Reaction\ Frequency = \frac{Reacted\ Specimen}{Total\ Tested\ Specimen} \tag{2.7}$$

$$Impact\ Sensivity = \frac{Explosion * 1 + Combustion * 1 + Light * 0.7 + Spark * 0.6 + Char * 0.4}{Total\ Tested\ Specimen} \tag{2.8}$$

2.3.5 Test perform

The tests were conducted on several separate days. On the first day, 1 set of epoxy systems was tested to verify the test setup and procedures. Initial tests were performed with the Huntsman Araldite 1564-3474 system, and no explosion, burning, light, or spark formation occurred. Once the system was deemed reliable and calibrated, all epoxy systems were tested.

Oxygen soaking of specimens is critical for accurate testing. If the sample is not soaked for a sufficient duration, the test may not yield combustion, light, or sparks. To ensure the reliability of the tests, specimens were submerged in liquid oxygen for a minimum of 5 minutes (Figure 2.28).

Figure 2.28 : Oxygen soaking of epoxy samples in cups before test

To create a liquid oxygen environment, a modification was made to the test system. A dewar was bolted to the system to hold a sufficient amount of liquid oxygen (Figure 2.29).

Figure 2.29 : LOX impact tests system and video recording.

2.3.6 Results and discussion

Twenty specimen tests were conducted using nine different epoxy systems. No combustion, light, explosion, spark, or carbonization was observed for the Huntsman Araldite 1564-3474 epoxy system and the Epotek T7109-19 epoxy system. In the first stage, both the Huntsman Araldite 1564-3474 and Epotek T7109-19 epoxy systems can be deemed LOX compatible.

he Huntsman 1564 resin system showed LOX compatibility with the 3474 hardener but was found to be non-compatible with LOX when using the 917 hardener. Since the Aradur 917 hardener is a methyl tetrahydrophtalic anhydride system, while Aradur 3474 hardener is an amine system, it is evident that the chemical structure of the hardener significantly influences the LOX compatibility of the resin systems. Information from the literature generally suggests that halogen groups are more compatible with liquid oxygen environments, which may be the case for the Aradur 3474 system [60–62]. Additionally, improving the anti-oxidation properties of polymers with modifiers could enhance LOX compatibility [63]. The low T_g of the Epotek T7109-19 may be one of the reasons for its demonstrated LOX compatibility, as low T_g effect stated in Harrison's study [62]. These results provide practical information about LOX compatibility of the tested specimens. Figure 2.30 illustrates the LOX impact test system and the explosion moment of the Epotek 301-2FL epoxy system.

Table 2.7 : Summary of LOX impact tested epoxy systems.

Epoxy system	Number of tested specimen	Count of explosion, combustion, light, spark and char occurence	Reaction frequency (%)	Lox compatibility
EPOTEK 301-2	10	9	90	U/ Non-Compatible
EPOTEK 301-2FL	10	9	90	U/ Non-Compatible
EPOTEK T7110	20	14	70	U/ Non-Compatible
EPOTEK T7109-19	20	0	0	BT/ Compatible
CE-A 1565 / CE-B 1971 / CE-S 700	10	9	90	U/ Non-Compatible
CE-A 11546 / CE-B 13447	20	8	40	U/ Non-Compatible
CE-A 105025 / CE-B 105025	10	6	60	U/ Non-Compatible
HUNTSMAN ARALDITE 1564-3474	20	0	0	BT/ Compatible
HUNTSMAN ARALDITE 1564-917-960	15	10	66.67	U/ Non-Compatible

Figure 2.30 : The explosion moment of Epotek 301-2FL epoxy system.

2.4 Epoxy Selection Criteria for Cryogenic Systems

A suitable selection criteria must be established for the application of epoxy systems in large-scale applications. This criteria should include :

1. Manufacturability:
    - Initial Sub-Criteria: Pot life of the resin system – Sufficient pot life for large-scale applications where resins are used in large quantities.

- Viscosity of the resin system – Applicability to conventional composite manufacturing methods; low viscosity to avoid fiber wetting problems.

2. Lox Compatibility:
    - Pass or fail requirement for LOX pressure vessels.
3. Mechanical performance:
    - Ability to endure pressure-driven deformations at cryogenic temperatures.
    - Strain-bearing capability and high strength in selected epoxies.
    - Tunable elastic modulus through the correct choice of epoxy system.
    - Endurance of loadings under both room temperature and cryogenic conditions.

Candidates are ranked based on their applicability to LOX pressure vessel manufacturing, with separate rankings for room temperature and cryogenic conditions. A total ranking is then derived from these two results.

Flexural strength, modulus, and elongation values are normalized according to the maximum values found in tests for all epoxy systems. Table 2.8, Table 2.9, and Table 2.10 indicate these rankings.

The mechanical tests and LOX compatibility assessments indicate that the Huntsman 1564-3474 epoxy system outperforms the other 9 epoxy systems. Consequently, further detailed investigations will be conducted on this system, and the consideration of tank production using this epoxy system will be explored

Table 2.8 : Maximum mechanical property normalization for room temperature across all epoxy systems

Epoxy System	Flexural Strength (RT)	Flexural Modulus (RT)	Elongation (RT)	Rank for (RT)
EPOTEK 301-2	0.88	1.00	0.33	0.293
EPOTEK 301-2FL	0.58	0.74	0.35	0.148
EPOTEK T7110	0.23	0.14	1.00	0.031
EPOTEK T7109-19	0.32	0.01	0.33	0.001
CE-A 1565 / CE-B 1971 / CE-S 700	1.00	0.79	0.44	0.350
CE-A 11546 / CE-B 13447	0.98	0.29	0.59	0.166
CE-A 105025 / CE-B 105025	0.81	0.38	0.38	0.116
HUNTSMAN ARALDITE 1564-3474	0.97	0.69	0.56	0.374
HUNTSMAN ARALDITE 1564-917-960	0.51	0.97	0.15	0.075

Table 2.9 : Maximum mechanical property normalization for cryogenic temperature across all epoxy systems

Epoxy System	Flexural Strength (CRYO)	Flexural Modulus (CRYO)	Elongation (CRYO)	Rank for (CRYO)
EPOTEK 301-2	0.85	0.51	0.81	0.348
EPOTEK 301-2FL	1.00	0.54	1.00	0.544
EPOTEK T7110	0.63	1.00	0.18	0.110
EPOTEK T7109-19	0.23	0.37	0.23	0.019
CE-A 1565 / CE-B 1971 / CE-S 700	0.39	0.34	0.46	0.061
CE-A 11546 / CE-B 13447	0.79	0.26	0.79	0.160
CE-A 105025 / CE-B 105025	0.75	0.29	0.67	0.147
HUNTSMAN ARALDITE 1564-3474	0.74	0.46	0.77	0.263
HUNTSMAN ARALDITE 1564-917-960	0.26	0.36	0.26	0.024

Table 2.10 : Total Rank according to mechanical rank and lox compatibility

Epoxy System	Total Rank	Lox Compatible or Not	Result
EPOTEK 301-2	0.102	No	
EPOTEK 301-2FL	0.081	No	
EPOTEK T7110	0.003	No	
EPOTEK T7109-19	0.000	Yes	
CE-A 1565 / CE-B 1971 / CE-S 700	0.021	No	
CE-A 11546 / CE-B 13447	0.027	No	
CE-A 105025 / CE-B 105025	0.017	No	
HUNTSMAN ARALDITE 1564-3474	0.098	Yes	Pass
HUNTSMAN ARALDITE 1564-917-960	0.002	No	

3. COMPOSITE LAMINATE TESTING - CONSTITUENT INTERACTION

The microcrak evolution and delamination are key points to understand composite laminate behavior under cryogenic contidions. For that reason, the cryogenic temperature effect on fiber-epoxy interaction delamination behavior has been investigated by end-notched flexure tests.

The vulnerability of composite structures is often associated with the formation and accumulation of micro-cracks in the matrix, representing the weakest links. These micro-cracks, stemming from matrix-related issues, can lead to leakage problems and a reduction in pressure-bearing capacity, even under room temperature conditions [4,64]. Particularly at cryogenic temperatures, the inspection and comprehension of the thermomechanical response become crucial, especially concerning failure modes driven by the matrix and matrix/fiber interface [65–67].

The advancement of composite pressure vessels necessitates a comprehensive and integrated approach, encompassing composite laminate design, modeling, material testing, and large-scale manufacturing.

On the macroscopic scale, research on cryogenic composite pressure vessels has primarily concentrated on permeability characteristics under cryogenic conditions. Notably, Flanagan et al. [68], conducted recent studies on the impact of cryogenic cycling on the permeability of PEEK matrix composite pressure vessels, taking into account variations in pressure, thickness, and fiber and matrix types. Grogan [21] delved into the experimental and numerical exploration of damage and permeability in tape-laid thermoplastic composite tanks. Additionally, Yokozeki [23] assessed helium leakage in carbon-fiber-reinforced plastic (CFRP) tubes, subjecting the composite tubes to tensile loading both at room temperature (RT) and cryogenic liquid nitrogen (LN2) temperature.

At the microscale, the thermomechanical properties of individual components play a crucial role in enhancing the composite laminate's response under cryogenic conditions, with particular emphasis on matrix materials. Numerous research studies have been conducted, and ongoing efforts persist to comprehend how matrices

contribute to the mechanical behavior of composite laminates. A prominent area of focus for matrix materials is toughened epoxy systems designed for cryogenic environments. These systems exhibit improved fracture toughness values due to molecular movement capabilities under cryogenic conditions, a phenomenon explained by the "free volume-free space" theory [38]. The prevailing trend in the literature involves toughening epoxy systems with additives/fillers such as multi-walled carbon nanotubes (MWCNT) [69], graphene platelets and rubbery particles [1,70,71]. Liu et al. [72] found that incorporating nanosheet boehmite (AlOOH) increases interlaminar fracture toughness at room temperature but does not show improvement under cryogenic temperatures. The type and weight ratio of fillers are critical for maximizing properties, and optimal values can vary between room temperature and cryogenic conditions [49,73]. Chemical toughening methods offer another approach for cryogenic environments, reducing transverse cracking under such conditions [67,74,75]. Coronado et al. [74] explored the low-temperature fatigue resistance of untoughened and toughened matrix systems, reporting the favorable impact of toughening on mode-I fatigue resistance. Various damage morphologies, including river markings, broken fibers, and hackle patterns, have been documented. However, the occurrence of transverse cracking in chemically toughened epoxy systems under cryogenic conditions has not been reported at the meso-mechanical scale, with accompanying fractographic images.

Theoretical investigations have explored the influence of manufacturing parameters, such as fiber width and fiber undulation parameters, on the mechanical properties and damage modes of composite laminates [76–78]. Numerical analyses have delved into meso-scale effects, particularly examining fiber undulations and winding patterns [79–81]. A recent study conducted at the mesoscale, utilizing a three-dimensional (3D) repeated unit cell (RUC) by Pourahmadi [82], suggests that fiber bundle crossovers and undulations can induce changes in mechanical and thermal properties of up to 15.7%, compared to predictions based on composite lamination theory. Shen et al. [83] also explored the effects of fiber crossover and undulation on stiffness failure through numerical and analytical calculations, noting that strain levels are approximately 1.07–1.13 times higher in undulation regions compared to laminate regions. It's important to note that these works are centered on mesoscale winding pattern analysis and do not specifically address tow undulation effects at the microscale level.

Assessing fracture toughness through measurements to understand crack formation and propagation in composite structures has become a complex task, mainly due to the aforementioned variations across different length scales. Extensive investigations into these effects have been conducted at room temperature for various composite structures. Barcikowski and Rybkowska [84] delved into the characterization of reactive rubber-added toughened epoxy resins. Rased [85] explored the impact of an asymmetrical stacking sequence on the fracture toughness values of carbon fiber composites, employing double-cantilever beam (DCB), end-notched flexure (ENF), and mixed-mode bending (MMB) tests. Morais [86] focused on the mode-II behavior of angle-ply glass/polyester filament-wound specimens. Bonhomme et al. [87] conducted an investigation into the mode-I and mode-II interlaminar fracture surfaces of a unidirectional AS4/8552 carbon/epoxy laminate, employing both fractographic and numerical analyses at room temperature.

Research on fracture toughness testing under cryogenic temperatures is comparatively limited in contrast to testing efforts conducted at room temperature. Li et al. [88] delved into the investigation of micro-crack progression, discussing the impact of a flexible molecular-structured epoxy on the cryogenic mechanical performance of both the matrix and CFRP laminates. Tensile and flexural tests were conducted under both room temperature and cryogenic conditions. Shindo [89] focused on studying the delamination growth of woven glass-reinforced epoxy with mode-II fatigue loadings and four-point ENF tests at cryogenic temperatures. Choi and Sankar [90] performed four-point bending tests on single-notched graphite–epoxy laminates at both room and cryogenic temperatures. While these studies offer valuable insights, the current state of the art lacks an experimental approach that concurrently performs resin (ex-situ) and laminate (in-situ) testing. Additionally, the presented fractographic analyses have primarily aimed at explaining selected laminate behaviors rather than elucidating the impact of resin choice and how corresponding fracture mechanisms are affected under cryogenic environments..

Commencing from this point, this section endeavors to underscore the impact of resin type and manufacturing-related irregularities, such as resin bagging, fiber undulations, and fiber wetting, on the mode II delamination behavior of wet-wound unidirectional (UD) composite specimens. Emphasis is placed on the fractographic identification of these anomalies, which holds paramount significance for the failure analysis of

composite pressure vessels. Three distinct resin systems, low viscosity-cold curing (CC), low viscosity-warm-to-hot curing (VI), and toughened epoxy systems (T) were utilized for both neat epoxy tests and manufacturing of carbon fiber-reinforced polymer (CFRP) laminates. Conventional filament winding was executed using a 4-axis winding machine. The end-notched flexure (ENF) specimens were crafted from $(0)_{16}$ laminates, formed through filament winding on a flat mandrel. Subsequent testing of these specimens was carried out to determine their mode II strain energy release rates (G_{IIc}) under room temperature (RT) and cryogenic (LN2) conditions. The modes of failure in filament-wound CFRP laminates, manufactured with different resin types, and the temperature-dependent effects on resin morphologies were investigated through detailed fractographic analyses. This thorough examination of fracture surfaces aims to provide a comprehensive understanding of the intricate interplay between epoxy system behavior and the damage mechanisms inherent within mesoscale architecture filament-wound composite laminates.

It is important for the reader to acknowledge that while this study concentrated on G_{IIc} determination, further exploration involving other standardized mechanical tests for constituent interaction should be considered. The limitations of this study are acknowledged, as the focus was primarily on G_{IIc} determination based on the testing capabilities available to the authors.

3.1 End-Notched-Flexure Tests

The End Notched Flexure Test is used for determining the mode II interlaminar fracture toughness, G_{IIc}, of unidirectional fiber reinforced polymer matrix composite laminates under mode II shear loading. ASTM D7905/D7905M-19 [91] standard has been used for test procedure.

3.1.1 Test standard

The ENF (End Notched Flexure) specimen, illustrated in Figures 3.1 and 3.2, comprises a rectangular, uniformly thick, unidirectional laminated composite specimen with a non-adhesive insert at the midplane, functioning as a delamination initiator. Forces are applied to the specimen using an ENF fixture under displacement-controlled loading.

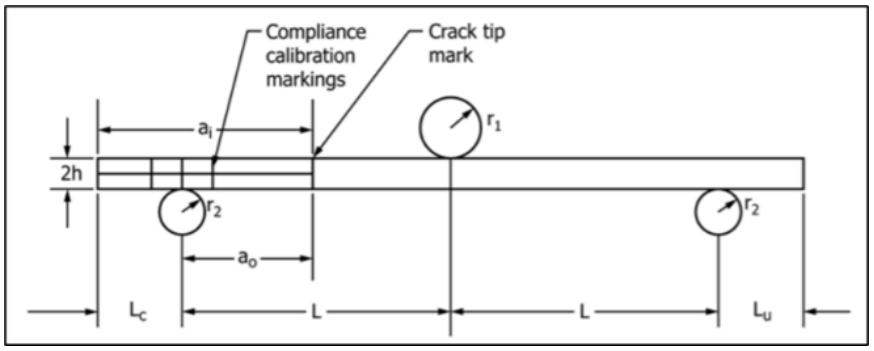

Figure 3.1 : ENF specimen, fixture, and dimensions [91].

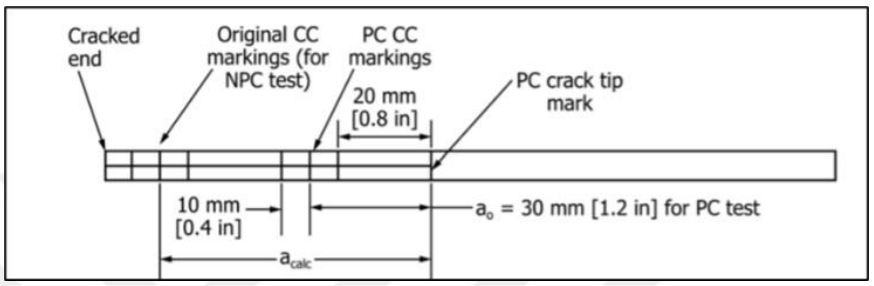

Figure 3.2 : Configuration of specimen for precracked test when the same specimen is used for NPC and PC testing [91].

The experimental procedure begins with compliance calibration tests, which aim to establish the specimen's compliance in relation to crack length. This is achieved by loading and unloading the specimens within the elastic range of behavior. Subsequently, tests to failure are conducted to ascertain the interlaminar fracture toughness of the examined composite interface, quantified in terms of the critical energy release rate. These tests are performed utilizing a Shimadzu AG-X Plus mechanical testing machine (Shimadzu, Kyoto, Japan) equipped with a 10 kN load cell. The three-point bending fixtures employed in the tests were designed and manufactured in-house.

3.1.1.1 Materials and methods

This study utilized three distinct DGBEA epoxy systems. The first, MARKUT 5025 (CC resin), is a cold-curing system designed for aerospace applications. The second, BASAT 11546 (VI resin), is a warm-to-hot-curing vacuum-infusion resin system obtained from CET Epoksi Teknolojileri A.Ş. (Istanbul, TR). The third, CTD 7.1 Toughened Epoxy Resin (T resin), is a cryogenic resin system known for its high microcrack fracture toughness, sourced from Composite Technology Development Inc. (Lafayette, Louisiana, USA). Ensuring the suitability for the filament-winding

process, particular attention was devoted to the viscosity values of the chosen resin types. The characteristics of the purchased resin samples are outlined in Table 3.1.

For the manufacture of CFRP laminates, A-49 12K tow carbon fiber was procured from Dow-Aksa (Istanbul, TR), as illustrated in Figure 3.3.

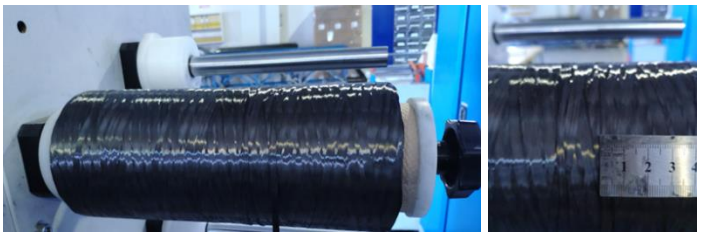

Figure 3.3 : (a) Carbon fiber tow; (b) carbon tow bandwidth.

Table 3.1 : Epoxy systems, pot life, curing cycle and viscosity properties.

Resin System	Pot Life at 23 °C (hours)	Nominal Curing Cycle	Resin Viscosity (cPs)	Hardener Viscosity (cPs)	Measured T_g (°C)	Data Sheet T_g (°C)
MARKUT 5025 (CC resin)	2–3	1 day 23 °C + 4 h 100 °C	1000–1500 at 5 °C	40–60 at 25 °C	98.8	118–124
BASAT 11546 (VI resin)	4.5	1 h 80 °C + 4 h 120 °C	1200–1400 at 25 °C	10–30 at 25 °C	109.3	115–120
CTD 7.1 Toughened Epoxy Resin (T resin)	3.5	2 h 80 °C	1500–5000 at 50 °C	12 at 25 °C	66.3	80

The viscosity of the selected resin systems varied significantly, which was impacted by both the resin and hardener viscosities. The VI resin system demonstrated the lowest mixed viscosity, whereas the T system demonstrated the highest.

3.1.1.2 Specimen preparation

Initially, neat epoxy samples were crafted for testing under both room-temperature and cryogenic conditions. Prior to stoichiometric mixing, all samples underwent a gentle mixing process lasting 15 minutes to increase the homogeneity of the resin, hardener, and initiator components. Subsequently, these mixtures were carefully introduced into silicon molds shaped in accordance with ASTM D790-17 [39]. The curing process occurred in a temperature- and humidity-controlled oven, adhering to the

recommended curing specifications provided by the manufacturers (as detailed in Table 3.1). The glass transition temperature (T_g) values from the in-house manufactured samples fell within an acceptable range, considering the scale of production.

ENF (end-notched flexure) test specimens were manufactured following the guidelines outlined in ASTM D7905/D7905M-19 [91] (Figure 3.4). The filament winding of the $(0)_{16}$ unidirectional (UD) laminates adhered to ISO 1268-5 [92] standards and was conducted using a specially designed mandrel. In this process, a single row of fiber with a 3.1 mm bandwidth was employed (see Figure 3.5a). The winding tension was set to 20 N, and the average winding speed was maintained at 15 rpm. Four hoop layups were wound, with a 12µm Teflon-based insert material positioned at both ends of the mandrel (depicted in Figure 3.5b). Subsequently, four more hoop layups were added to achieve a symmetrical and balanced laminate. CFRP specimens were then obtained from the manufactured laminates through water jet cutting, as illustrated in Figure 3.5c, showcasing the undulations resulting from the filament-winding process.

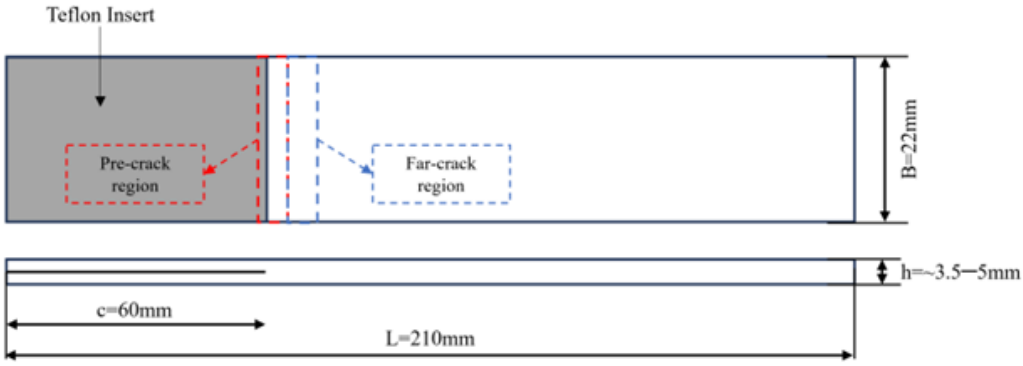

Figure 3.4 : Dimensions of ENF laminates (dashed line regions represent investigated fracture regions.

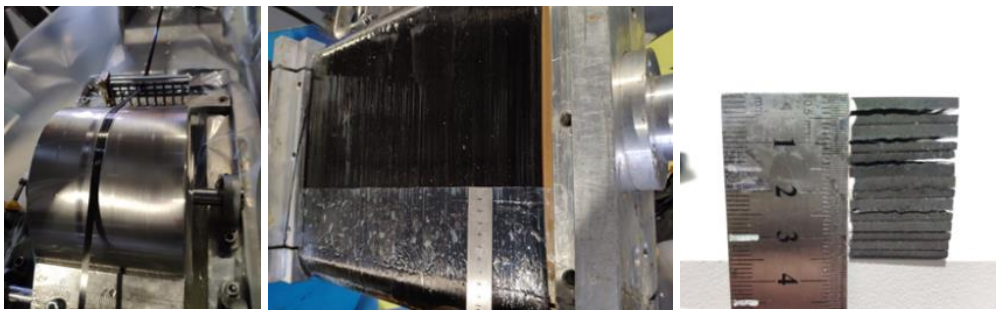

Figure 3.5 : (a) One row of tow; (b) filament-winding process; (c) cross-section view of ENF specimens.

3.1.1.3 Mechanical tests

The initial emphasis was on conducting cryogenic tests specifically on the neat epoxy samples, aiming to explore the inherent behavior and in-situ responses of the selected resins.

Subsequent to ASTM D790 [39] standards, three-point bending tests were executed on the neat epoxy samples to assess their mechanical characteristics under both room-temperature and cryogenic conditions. These tests were carried out using a 10kN Shimadzu AGS-X universal testing machine located in Kyoto, Japan, with a crosshead displacement rate set at 5mm/min. The recorded force-versus-displacement values were utilized for subsequent computations, including parameters such as the maximum flexural strain (ε_{max}), maximum flexural stress (σ_{max}) and E_{flex} flexural modulus. These parameters were determined using the equations 2.3, 2.4, 2.5.

The identical three-point bending fixture was used for the ENF testing, with a constant crosshead displacement rate of 5mm/min. As a result, the non-precracked G_{IIc} values were computed using direct beam theory, as described in [93]. The following is the formula for calculating G_{IIc} (Equation 3.1):

$$G_{IIc} = \frac{9a^2 P\delta}{2b(2L^3+3a^3)} \tag{3.1}$$

where P represents the maximum force, δ is the maximum displacement, a is the delamination crack length, b is the specimen width and L is the span length. Both RT and LN2 tests were carried out (See Figure 3.6).

Figure 3.6 : ENF test performed in (a) RT environment; (b) LN2 environment.

The room-temperature testing were carried out in a temperature range of 20-25°C, whereas the cryogenic tests entailed immersing the specimen in liquid nitrogen (LN2).

The temperature of the LN2 was monitored using a thermocouple and kept constant at −196±1 °C. To avoid thermal shock, the specimens were pre-cooled in boiling liquid nitrogen before being tested in LN2.

3.1.1.4 Microscopy

The tested ENF specimens were thoroughly examined from all sides to determine the type of cracking events caused by temperature changes.

A Zeiss LEO Supra VP35 field emission scanning electron microscopy (SEM) was used to analyze the fracture surfaces of the ENF samples (Sabanci University, Istanbul, TR). A thin conductive Au/Pd layer was sputtered over the samples prior to examination. The examination was divided into two parts: the pre-crack front (crack initiation zone) and the remote regions (crack propagation zone). During testing, samples were obtained from both the end of the insert and the fracture surface, allowing for observations and comments on variations in crack initiation and propagation. The fracture surfaces were examined in the secondary electron mode with a gun voltage of 5 kV.

3.1.2 Results

3.1.2.1 Three-point bending tests

Figure 3.7 depicts example flexural stress/strain curves derived from testing on clean epoxy samples, demonstrating a shift from elastoplastic to completely elastic behavior at cryogenic temperatures. Table 3.2 displays the summary findings. Under cryogenic circumstances, E_{flex} increased by around 280-400% for all three resin systems, owing mostly to embrittlement.

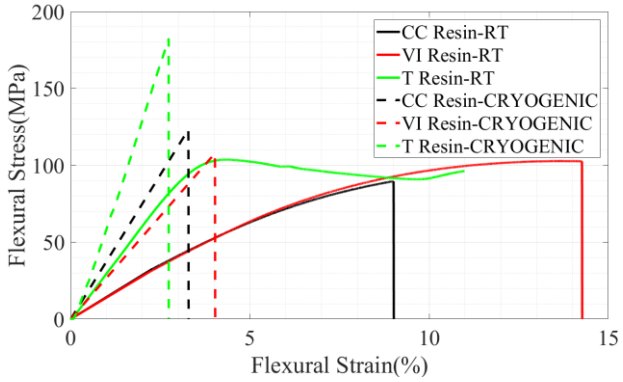

Figure 3.7 : Representative flexural stress–strain curves of three-point bending tests of neat epoxy.

Table 3.2 : Three-point bending and ENF results of epoxy specimens at room and LN2 temperatures.

Resin Type	Test Environment	σ_{flex} (MPa)	ε_{flex} (%)	E_{flex} (MPa)	G_{IIc} (kJ/m^2)	Vf
CC Resin	RT	83 ± 9	8.4 ± 1.6	1012 ± 123	1.74 ± 0.17	0.5
	LN2	139 ± 32	3.8 ± 0.9	3643 ± 63	0.88 ± 0.05	
VI Resin	RT	100 ± 4	13.2 ± 1.1	765 ± 61	0.97 ± 0.21	0.55
	LN2	146 ±26	4.5 ± 1.1	3180 ± 90	0.94 ± 0.08	
T Resin	RT	102 ± 7	4.7 ± 0.4	2243 ± 322	1.27 ± 0.09	0.45
	LN2	171 ± 28	2.7 ± 0.3	6331 ± 578	1.22 ± 0.12	

Strength values increased at cryogenic conditions for all three systems as compared to room temperature values. Maximum elongation values did, however, fall noticeably after moving to cryogenic conditions. This discovery implies that the chain mobility of the resin systems has decreased, resulting in an increase in intermolecular binding pressures. These modifications had a direct impact on the observed E_{flex} and elongation values [43,94–96].

During the room-temperature test, the toughened resin system (T resin) displayed exceptional toughness, effectively sustaining contact with the test fixtures, showing a clear proof of its beneficial toughening impact. However, in cryogenic circumstances, this toughness effect was lost, rendering the resin brittle. In the CC resin and VI resin systems, a comparable temperature-induced brittleness effect was found. Notably, the toughened resin system's E_{flex} value at normal temperature roughly matched the cryogenic temperature E_{flex} values of the other resin systems. The T system was the most influenced by cryogenic temperatures, exhibiting the highest strength value and the lowest strain under these circumstances.

3.1.2.2 End-notched flexure tests

Figures 3.8 and 3.9 illustrate the force-elongation and flexural-stress–flexural-strain curves of the tested ENF specimens, respectively. The G_{IIc} values for the CC resin system showed a decrease from 1.74 ± 0.17 (kJ/m^2) at room temperature to 0.88 ± 0.05

(kJ/m^2) at cryogenic temperature. In contrast, the VI and T resins did not exhibit such a substantial decrease in G_{IIc} values (see Table 3.2). The VI resin demonstrated G_{IIc} values of 0.97 ± 0.21 (kJ/m^2) at room temperature and 0.94 ± 0.08 (kJ/m^2) at cryogenic temperature. Notably, the T resin system displayed a consistent force–elongation curve under both room and cryogenic conditions, yielding G_{IIc} values of 1.268 ± 0.091 (kJ/m^2) and 1.216 ± 0.121 (kJ/m^2), respectively. The underlying reasons for the measured G_{IIc} values will be discussed in more detail in the subsequent section covering fractographic analysis.

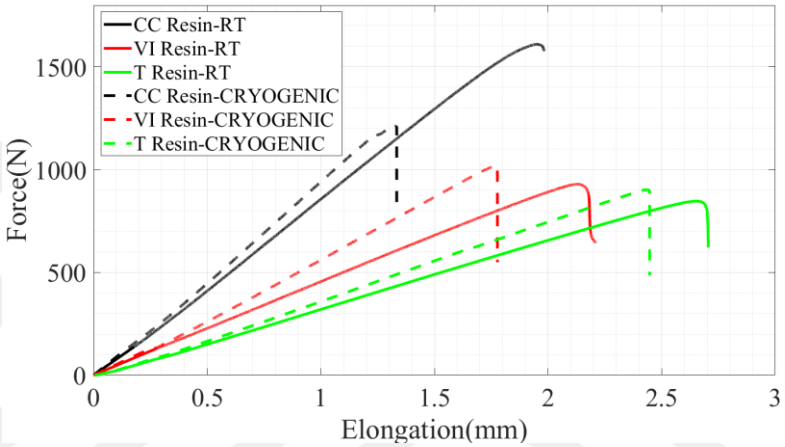

Figure 3.8 : Representative force–elongation curves of ENF specimens.

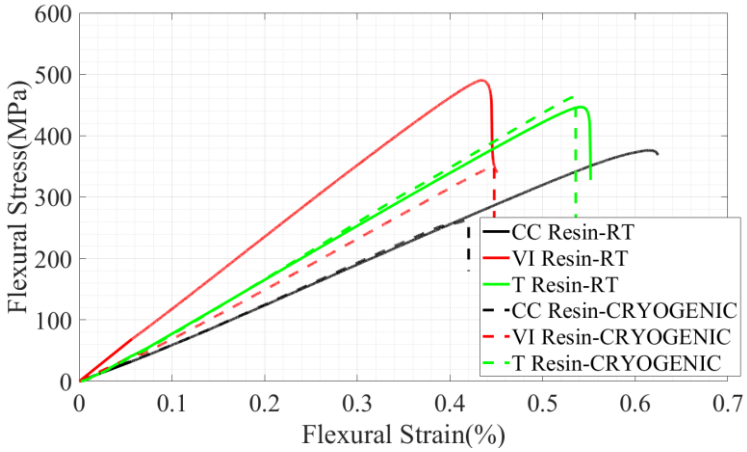

Figure 3.9 : Representative flexural-stress–flexural-strain curves of ENF specimens.

3.1.3 Discussion

3.1.3.1 Macro-scale interpretation of the main mode of failure

The effect of tow undulation was visible in cross-sectional views of the studied specimens, as shown in Figure 3.5c. The specimens' side views (Figure 3.10) revealed

a linear fracture propagation pattern at ambient temperature, which was replaced by a zig-zag crack propagation pattern under LN2 conditions. At room temperature, the expected linear fracture propagation was consistent with ENF testing, confirming mode-II crack propagation along the interlaminar plane [85]. The periodic zig-zag fracture propagation in the LN2 environment, on the other hand, revealed the coexistence of intra- and interlaminar damage propagation. The decrease in G_{IIc} values, together with the presence of intra-laminar cracking, revealed the major mechanism of failure as fiber/matrix debonding at LN2 settings as a result of the high cold impacting standard resin types. This is due to the considerable disparity in thermal expansion coefficients between the investigated resins and carbon fibers [88–90].

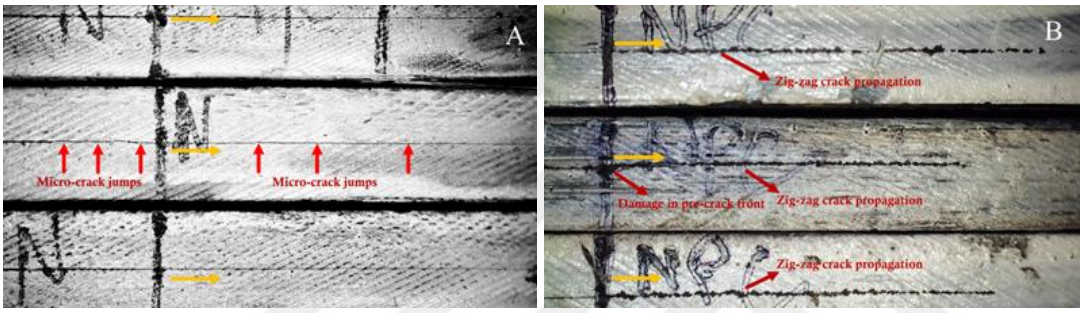

Figure 3.10 : Side views of tested specimens: (A) CFRP-CC resin at RT with linear crack propagation; (B) CFRP-CC resin at LN2 with zig-zag crack propagation.

3.1.3.2 Crack propagation surfaces and resin morphologies

Pre-crack region (crack initiation zone)

Inserting pre-cracks during conventional filament winding presents challenges compared to other mold-based manufacturing techniques like pre-preg laying or RTM. This process requires a temporary halt in the entire manufacturing operation, introducing pre-cut non-sticking films at the crack-initiation regions on one part of the flat mold. During this pause, variations in resin viscosities may lead to changes in the amount of liquid resin on the pre-tensioned carbon fibers. As the process is continuous, the tows subjected to this interruption form the upper part of the interlaminar region. Consequently, the amount of resin on the interlaminar plane may vary, resulting in resin bagging [74]. SEM analysis of the pre-crack fronts of selected samples revealed resin bagging as the primary characteristic on samples that fractured at room temperature (Figure 3.11A–C). This issue led to the formation of periodic tow undulation, creating hills on the fracture surface and causing non-planar mode-II crack propagation. This, in turn, resulted in nearly perpendicular shear cusps at the side of

the hills and simultaneous fiber/matrix debonding on the plateau. The damage shape of the matrix was influenced by the local stress state and the orientation of the hackles, indicating the direction of crack propagation [97]. In the case of the toughened T resin system, local out-of-plane crack deflections revealed instances of crack jumping to other planes, and non-uniform crack initiation occurred at the crack front characteristics unique to the conventional filament-winding process. [82,83,85].

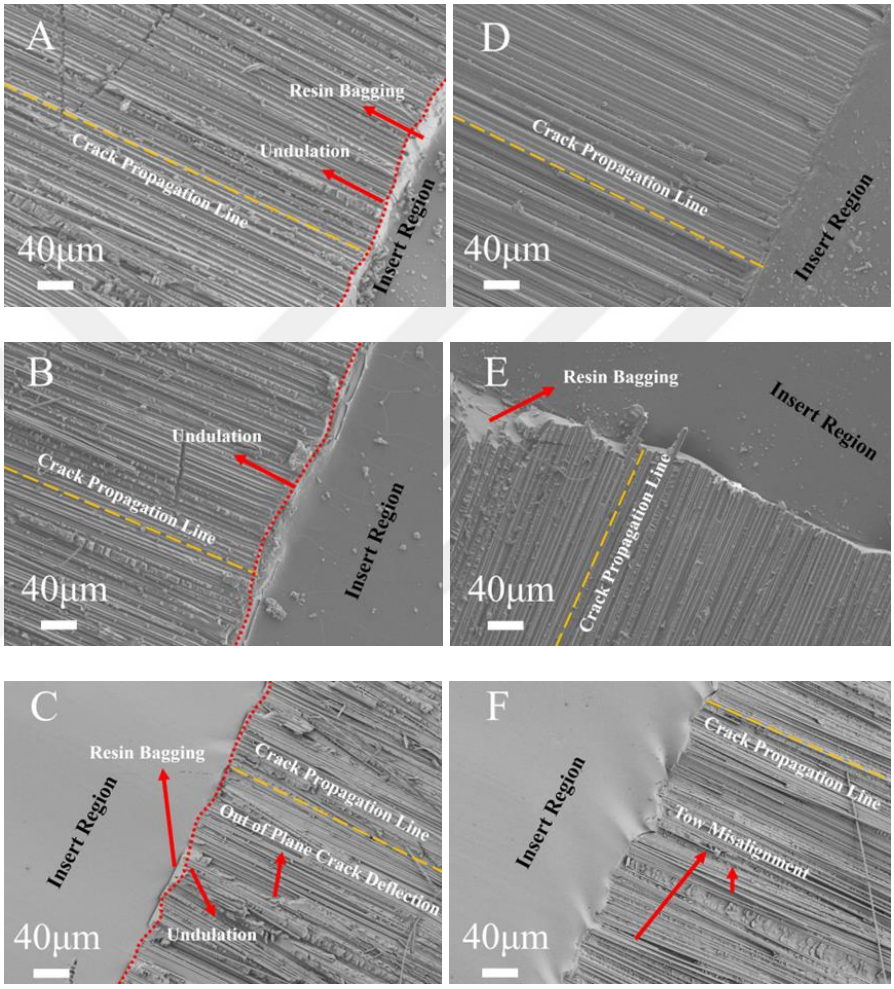

Figure 3.11 : Fractography images belonging to the pre-cracked region of fractured ENF samples; left shows RT sample: (A) CFRP-CC resin; (B) CFRP-VI resin; (C) CFRP-T resin. Right shows LN2 sample: (D) CFRP-CC resin; (E) CFRP-VI resin; (F) CFRP-T resin.

In the far region of the same undulated tow (Figure 3.11A–C), larger hackle formations, characteristic of mode-II crack propagation and fiber/matrix debonding regions, were evident, illustrating the variance in the resin volume fraction along the interlaminar plane. This phenomenon was attributed to the limited control of perpendicular resin flow and tow overlapping [102,103] during the wet-winding

process. In the investigated cases, the resin flow issue was exacerbated by the pre-crack sticking-film-insertion process, necessitating a complete process stop.

Under cryogenic conditions, the surface view appeared mostly flat and smooth, indicating fiber/matrix debonding without any plastic deformation (Figure 3.11D,E). The effect of tow undulations was minor. However, for the toughened case, matrix hackle patterns and fiber/matrix debonding damage modes were observed. Additionally, the tow misalignment suggested that tow movement was still effective for this toughened resin system due to the sample's plastic deformation capability under cryogenic conditions (Figure 3.11F).

Far-crack region (crack propagation zone)

Low-magnification images of the fracture surfaces for all three specimen types are depicted in Figure 3.12. One notable distinction in the CFRP-VI resin laminate was the observed lower fiber wettability on the delamination surface. In contrast, the CFRP-CC resin and CFRP-T resin surfaces exhibited significantly larger and more abundant hackle patterns (serrations) [97] than those observed in the CFRP-VI resin laminate. This variation contributes to the differences in the measured G_{IIc} values at room temperature. Another noteworthy observation was the coexistence of interlaminar delamination (marked by hackle patterns between continuous fibers) and fiber/matrix debonding failure events for all three types of specimens (as highlighted in Figure 3.12A, C, E). The continuous carbon fiber surfaces of the CFRP-CC resin laminates appeared relatively smoother in comparison to CFRP-VI resin, indicating weaker fiber/matrix adhesion in the former. Conversely, the T resin system exhibited well-preserved regions of the fiber/matrix interface, signifying robust fiber/matrix adhesion. Even in cases of fiber breakage, the presence of strong fiber/matrix adhesion was evident, leading to fiber rupturing (Figure 3.12E).

Moreover, the presence of perpendicular hackle patterns (Figure 3.12A) suggests that the meso-structure resulting from the winding process induced non-planar crack propagation. This contributed to an increase in the measured G_{IIc} values due to the tow interlocking effect. The frequency of such patterns was relatively lower in the case of the CFRP-VI resin (Figure 3.12C). Upon closer examination (Figure 3.12B), the morphology of hackle patterns revealed that the in-situ behavior of the CC resin was more ductile compared to the VI resin. This contrasts with the three-point bending results (Table 3.2). This contradiction suggests that the higher strain values measured

for the CC resin system during ENF testing (Figure 3.6) were primarily due to the low fiber volume fraction ratio and the undulations in the tow structures, which were facilitated at room temperature.

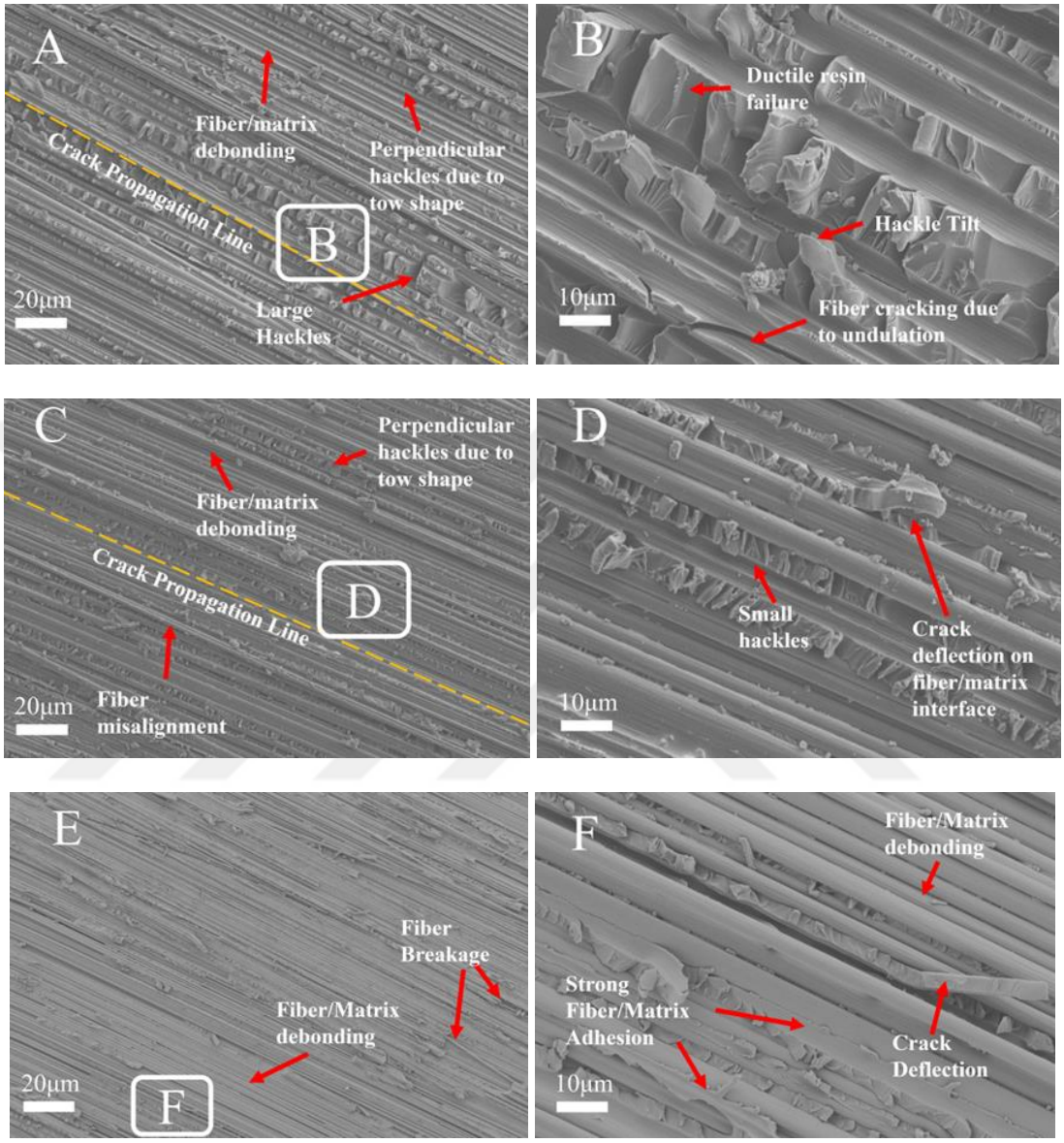

Figure 3.12 : Fractography images belonging to fractured ENF samples at RT (A); (B) CFRP-CC resin system (C); (D) CFRP-VI resin system (E); (F) CFRP-T resin system.

Conversely, the fiber/resin interaction was significantly more favorable in the case of the VI resin and the CC resin, where the surfaces of the carbon fibers were not as smooth. This resulted in a reduced impact on mode-II crack propagation (Figure 3.12D, E). The resin damage morphology in the toughened system showed crack deflection in the investigated region (Figure 3.12F). The toughness effect

demonstrated its contribution to the damage mode of the resin system due to strong fiber/matrix adhesion and high shear deformation capability (Figure 3.12F).

Effect of LN2 on multi-scaled interactions

In comparison to the room temperature testing, the number of resin failure marks on the samples at cryogenic temperatures was significantly lower and less densely distributed, showing that resin failure and tow undulations had a lower influence on the fracture of the CC resin system (Figure 3.13A). As a result, the macroscale zig-zag fracture propagation (Figure 3.13b) was predominantly attributable to fiber/matrix debonding. The rate of resin failure was substantially higher on the damaged surface of the toughened resin system, where the resin remained effective under freezing temperatures (Figure 3.13C). The overall look of the fracture surface of the CFRP-VI resin laminates (Figure 3.13B) was similar to that of the CFRP-CC laminates, supporting the similarity in the measured G_{IIc} values.

Under cryogenic circumstances, a noticeable shift in the resin morphologies for the CC resin and VI resin was visible when zoomed in (Figure 3.13D, E). The brittleness effect resulted in smaller and thinner hackles at the fiber/matrix contacts in this case [46]. In contrast, resin damage predominated in the T resin system, demonstrating that the resin contributed to the G_{IIc} values under freezing settings (Figure 3.13F). The CFRP-VI resin and CFRP-T resin laminates once again demonstrated improved fiber/matrix bonding. This was especially important for the cryogenic fracture of the laminates, because the major mode of failure was fiber/matrix debonding. Under cryogenic settings, the toughened CFRP-T resin exhibited massive cracked ductile hackles as well as good fiber/matrix adhesion. This explains the similar G_{IIc} values reported for this resin system under RT and LN2 settings.

When further zoomed in, the form of the hackles on the CFRP-CC resin laminate revealed an example failure mechanism specific to cryogenic testing. Due to the severe cold and substantial disparity in the thermal expansion coefficients of the materials, this mode featured fiber/matrix interface cracking and fiber shear rupture (Figure 3.13G) [89]. This circumstance might have resulted in a self-cracking event before to loading, thus resulting in a decrease in the G_{IIc} readings. This failure mechanism was not found in the CFRP-VI resin and CFRP-T resin laminates, which had improved fiber/matrix adhesion. The strong fiber/matrix adhesion in the CFRP-T resin system led in tow cracking and splitting on the fiber (Figure 3.13I). Furthermore, the ductile

resin failure morphology demonstrated this resin system's cryogenic performance capabilities (Figure 3.13I).

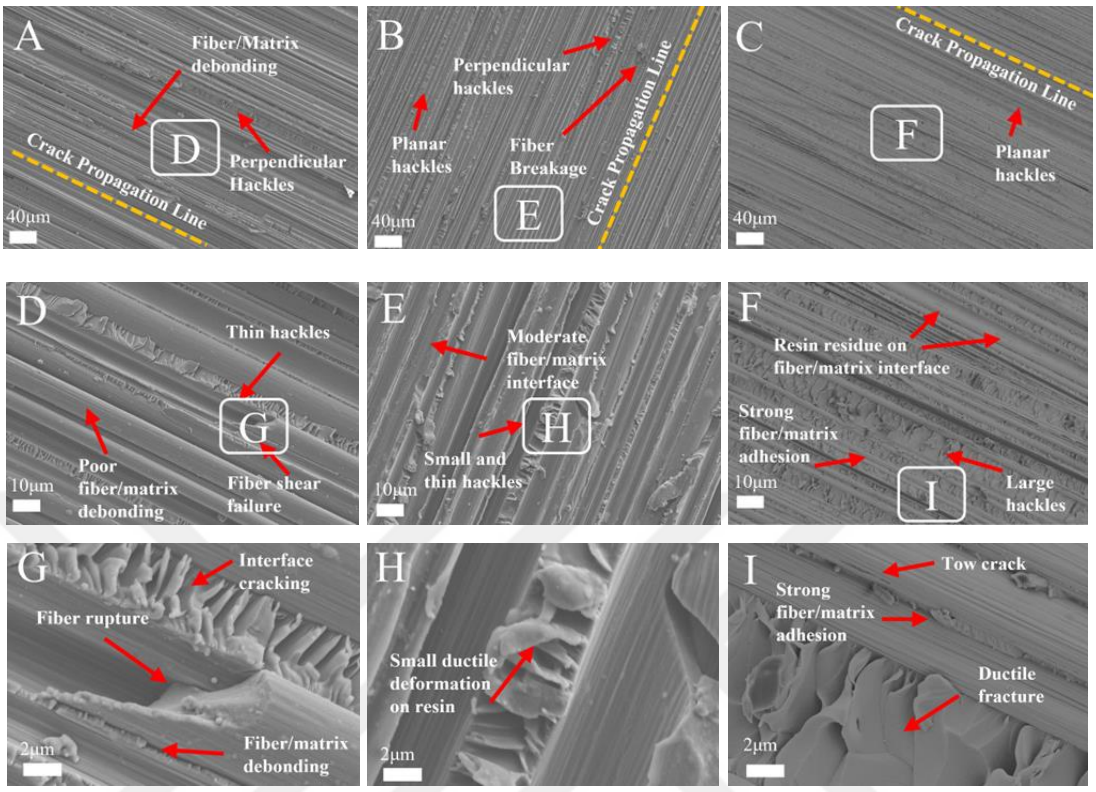

Figure 3.13 : Fracture surfaces of cryogenic fractured filament wound UD $(0)_{16}$ laminates with (A, D, G) CFRP-CC resin, (B, E, H) CFRP-VI resin and (C, F, I) CFRP-T resin.

3.2 Conclusions

The mode-II delamination behavior of filament-wound CFRP laminates with different resin types was extensively investigated under both room-temperature and cryogenic conditions through a detailed fractographic analysis. Notably, the G_{IIc} values of the CC resin system exhibited a significant reduction, decreasing from 1.74 ± 0.17 (kJ/m^2) at room temperature to 0.88 ± 0.05 (kJ/m^2) at cryogenic temperature. In contrast, both the VI and T resin systems displayed relatively stable G_{IIc} values between room and cryogenic temperature, with the VI resin at 0.97 ± 0.21 (kJ/m^2) and 0.94 ± 0.08 (kJ/m^2) and the T resin system at 1.268 ± 0.091 (kJ/m^2) and 1.216 ± 0.121 (kJ/m^2) for room and cryogenic conditions, respectively. The experimental findings lead to several conclusions:

Three-point bending tests on neat epoxy specimens revealed that cryogenic temperatures caused decrease on elongation and increase on strength and stiffness due

to embrittlement. However, the neat epoxy's behavior may not accurately reflect the cryogenic performance of composites, emphasizing the need for experiments focusing on single-fiber tow/resin interactions.

The mode-II delamination behavior was significantly affected by resin bagging and tow undulation problems associated with conventional wet winding, leading to complex 3D crack propagation. Tow movement at room temperature contributed to resin ductility, enhancing G_{IIc} levels through tow interlocking.

During crack propagation at room temperature, it has been observed matrix shear failure, fiber/matrix debonding, and fiber fracture events existed. Under severe cold conditions, the primary failure mode moved to fiber/matrix debonding, which is characterized by evident zig-zag fracture propagation.

The VI resin, which had the lowest mixture viscosity, had a wetting issue, which boosted the contribution of the undulated fiber architecture (tow interlocking). This process accounted for the comparable G_{IIc} values measured at ambient and cryogenic temperatures, with the embrittlement events reported for the resin system having a minimal influence on the laminate behavior.

With a moderate mixture viscosity, the CC resin system allowed for enhanced wetting of the interlaminar plane. This was related to the pre-crack insertion technique, which briefly interrupted the overall winding process. The undulated fiber structure and matrix phase worked together to provide the highest G_{IIc} values recorded at room temperature. However, this example also had the greatest G_{IIc} drop at cryogenic temperatures, which might be related to resin embrittlement. According to the fractographic investigations, nanoscale matrix cracking, fiber shear fracturing, and fiber/matrix debonding events all contributed to the eventual fracture.

The T resin system, which had the maximum mixture viscosity, also provided good wetting. The G_{IIc} values of the T resin system, like those of the VI resin system, were constant at freezing circumstances. Fractographic analyses revealed improved fiber/matrix adhesion at cryogenic temperatures. This resulted in an equal contribution of the matrix phase during mode-II fracture propagation. Notably, typical shear hackles associated with mode-II crack propagation were found on the fracture surfaces of the cryogenic samples evaluated. This circumstance did not exist in any of the other

resins since damage progression at cryogenic temperatures was always begun by fiber/matrix debonding and then followed by other failure events.

In conclusion, the provided results and conclusions highlight the main, material selection and manufacturing-related concerns that impact the performance of filament-wound laminates under cryogenic temperatures. Although such issues may be solved with more sophisticated AFP processes, the given interpretation of wet-wound laminate delamination behavior may provide insight for future material development. Pressure vessels with limited operating lives (e.g., sounding rockets) might still be efficiently built using traditional filament winding, which remains a dominant and cost-effective manufacturing technology in terms of volume.

4. MULTI-SCALE COMPOSITE MODELLING FOR RESIN CRACKING

The simulation method of composite materials are generally performed with orthotropic material definition. However, to correctly interpret the thermomechanical constituent behavior, one should consider micromechanical response of the structure to external loadings. The general macroscale orthotropic composite modelling does not provide enough information in case of microcrack investigation. The micromechanical calculations provide details about microcracking events on resin and fiber/matrix interface debonding. The determination of microcrack evolution and progression in composite laminates have a crucial importance in case of cryogenic composite pressure vessels. For that reason, many studies have performed to understand this phonemana by using analytical and finite element calculations. In modeling studies, a multi-scaled approach is adopted, emphasizing the importance of constitutive relations at various length scales. Finite element analysis is commonly employed in these studies [98,99]. The overarching goal is to understand vessel performance by addressing key aspects such as (i) selecting constituents at the microscale [100], (ii) enhancing tow architectures at the mesoscale [66,67], and (iii) designing overall vessel responses at the macroscale [101].

The meso-scale approaches rely on meso finite element models, which can be achieved by using commercial programs such as Digimat, ANSYS Material Designer, and Abaqus. Also, open-source software programs provide these types of modeling techniques, such as TexGen [102]. These meso-scale models were employed to determine the transverse cracking progression between composite plies, which is especially critical for cryogenic composite pressure vessels. The study conducted by Peddiraju et al. [103] investigated the leakage path of cryogenic composite laminates using analytical and finite element simulation, including CFD analysis. Abilash and Roy address challenges such as transverse micro-cracks and delaminations, presenting mathematical models to predict delaminated crack opening displacement (DCOD) and permeability. The study's findings, validated with experimental data, emphasize the sensitivity of composite permeability to stitch crack lengths in individual plies under

thermal and/or mechanical loads [104]. In addition to the mechanical response, works for determining the permeation rate and software development have also been reported [89].

The micromechanical models are developed using representative element volume (RVE) models [105–107]. Representative model elements have fibers and matrix separately, and periodic boundary conditions provide an approximate behavior for each constituent. Also, these RVE elements can be used for homogenization and provide orthotropic material properties for the macro-scale level [108,109].

4.1 Multi-Scale Composite Modelling

There are different appraoches to calculate the micro stress in the composite structure under various mechanical and thermal loadings.

Micromechanical strategies have been broadly utilized for decades to understand about stress/strain distributions on composite structures, as well as the relationship between constituent properties and large scale (effective) properties of composite materials.

Analytical expressions are preferred in many cases, but the finite element analysis (FEA) offers higher accuracy. Many studies have been made in this topic focusing on FEA of the composites.

4.1.1 Stress ampfliciation factor method

Stress amplification factor method, which is based on linear stress-strain relationship, correlations have been developed and used by many researchers [105,110,111] to conduct relationship between macro and micro stresses by equations. By using RVE, effective material properties can be calculated.

The stress/strain amplification factor is used to construct the relationships between macro (ply) and micro stress/strain [105,110,111]. The stress and failure analysis of composite structures generally done with homogenized material properties for each ply. Micromechanic analysis allows to study each constituent properties separately. Ply properties can be computed based on the mechanical properties of the fiber and matrix, while the stress distribution in the fiber and matrix can be determined from the ply stress [105,110,111].

To study constituent properties of ply, a convenient model is needed. The RVE or unit cell has been studied by many researchers. The RVE provides micro-macro relationship can be structured. The muti-level appraoch for composite structures can be seen from the Figure 4.1 [105]. Figure 4.2 and Figure 4.3 depicts the fiber distribution types on laminates and on RVE element, respectively.

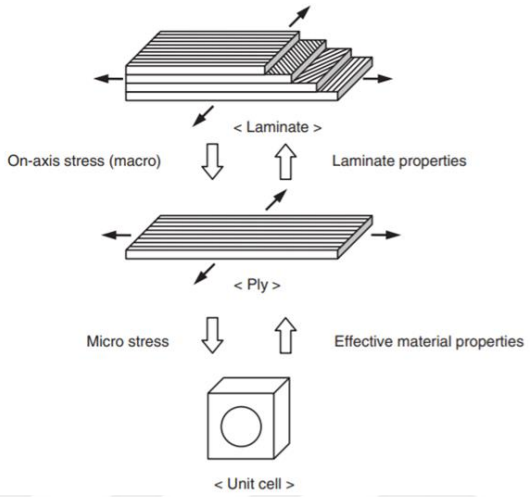

Figure 4.1 : Multi-scaled approach for composites [105].

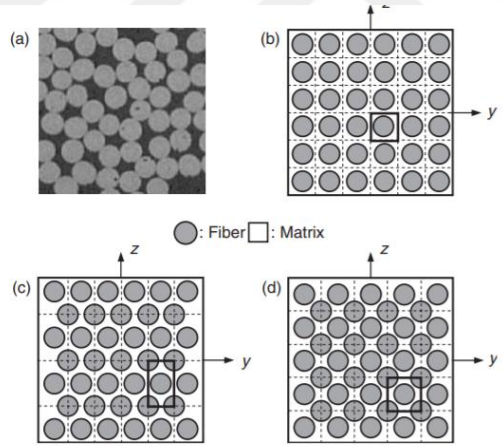

Figure 4.2 : (a) Fiber distribution on manufactured laminates, (b) Square distribution, (c) Hexagonal distribution, (d) Diamond distribution [105].

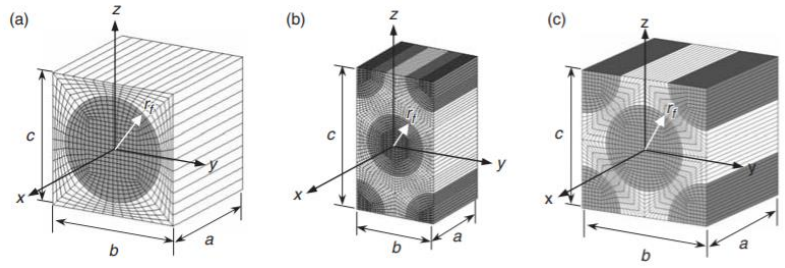

Figure 4.3 : Finite element model of regular fiber distributions; (a) Square distribution, (b) Hexagonal distribution, (c) Diamond distribution [105].

Three dimensional FE analysis can be used to calculate effective material properties and stress/strain distribution in continuous fiber reinforced composite materials at the microscopic level with high accuracy [105].

A linear stress–strain–temperature relation for a UD ply at the macro level can be formulated as follows (Equation 4.1):

$$\overline{\sigma} = \overline{C}\overline{\varepsilon}_{mech,} \qquad \overline{\varepsilon}_{ther} = \overline{\alpha}\,\Delta T, \quad \overline{\varepsilon} = \overline{\varepsilon}_{mech} + \overline{\varepsilon}_{ther} \tag{4.1}$$

where $\overline{\sigma}$ is macro stress, and $\overline{\varepsilon}$ is macro total strain; $\overline{C}$ and $\overline{\alpha}$ are macro stiffness matrix and macro coefficient of thermal expansion (CTE) respectively; $\overline{\varepsilon}_{mech}$ and $\overline{\varepsilon}_{ther}$ are macro mechanical and thermal strain, respectively. The component form of above Equation 3.1 for orthotropic material can be written as (Equation 4.2):

$$\begin{pmatrix} \overline{\sigma_1} \\ \overline{\sigma_2} \\ \overline{\sigma_3} \\ \overline{\sigma_4} \\ \overline{\sigma_5} \\ \overline{\sigma_6} \end{pmatrix} = \begin{bmatrix} \bar{C}_{11} & \bar{C}_{12} & \bar{C}_{13} & 0 & 0 & 0 \\ \bar{C}_{12} & \bar{C}_{22} & \bar{C}_{23} & 0 & 0 & 0 \\ \bar{C}_{13} & \bar{C}_{23} & \bar{C}_{33} & 0 & 0 & 0 \\ 0 & 0 & 0 & \bar{C}_{44} & 0 & 0 \\ 0 & 0 & 0 & 0 & \bar{C}_{55} & 0 \\ 0 & 0 & 0 & 0 & 0 & \bar{C}_{66} \end{bmatrix} \begin{pmatrix} \overline{\varepsilon_1} - \bar{\alpha}_1 \Delta T \\ \overline{\varepsilon_2} - \bar{\alpha}_2 \Delta T \\ \overline{\varepsilon_3} - \bar{\alpha}_3 \Delta T \\ \overline{\varepsilon_4} \\ \overline{\varepsilon_5} \\ \overline{\varepsilon_6} \end{pmatrix} \tag{4.2}$$

the macro compliance matrix S can be obtained by inverting the macro stiffness matrix C , and effective material properties or engineering constants can be computed from entities of S (Equation 4.3):

$$\begin{aligned} \overline{E_1} &= \frac{1}{\overline{S_{11}}}, \quad \overline{\nu_{21}} = -\frac{\overline{S_{21}}}{\overline{S_{11}}}, \overline{G_{12}} = \frac{1}{\overline{S_{66}}} = \overline{E_6} \\ \overline{E_2} &= \frac{1}{\overline{S_{11}}}, \quad \overline{\nu_{31}} = -\frac{\overline{S_{31}}}{\overline{S_{11}}}, \overline{G_{13}} = \frac{1}{\overline{S_{55}}} = \overline{E_5} \\ \overline{E_3} &= \frac{1}{\overline{S_{33}}}, \quad \overline{\nu_{32}} = -\frac{\overline{S_{32}}}{\overline{S_{22}}}, \overline{G_{23}} = \frac{1}{\overline{S_{44}}} = \overline{E_4} \end{aligned} \tag{4.3}$$

The Unidirectional (UD) ply is typically considered to be transversely isotropic, owing to the orthotropic nature of fibers and the randomly dispersed arrangement within the matrix. Despite uniform external loading, the strain and stress distribution within the fiber and matrix is non-uniform due to micro-level inhomogeneity. The macroscopic strain and stress distribution dictate the micro strain and stress state at each location

within the fiber or matrix. This complexity necessitates the development of equations that establish the relationship between micro strain and stress and their macroscopic counterparts [105].

Before deriving the specific equations, three logical hypotheses are introduced [105]:

1. Within both the fiber and matrix, every micro strain/stress component at each point is linearly dependent on macro strains/stresses as well as temperature increases;

2. Equation 4.1, representing the stress–strain–temperature relationship at the macro level, is equally applicable at the micro level.

3. The in-situ properties of the matrix are identical to its bulk properties.

Because of the mismatched CTE and stiffness of components, micro stresses are induced by macro mechanical strains. The following are the relationships between micro strain ε_{mech} at any internal location within the fiber or matrix and macro strains, as well as temperature (Equation 4.4) [105]:

$$\varepsilon_{mech} = M_{\varepsilon}\bar{\varepsilon}_{mech} + A_{\varepsilon}\Delta T \tag{4.4}$$

where M_ε and A_ε indicate strain amplification factors for macro mechanical strain and temperature increment at that point, respectively. M_ε is a 6x6 matrix, and A_ε is a 6x1 column vector. Without temperature effects, the general form of M_ε may be determined using the following basic concepts: micro and macro mechanical stresses are comparable in the longitudinal direction of the fiber; micro transverse linear strains plus micro transverse–transverse shear strain may be controlled by the coupled action of their macro counterparts, however, the coupled effect will have no influence on the values of two micro longitudinal shear stresses, which are also dominated by the macro counterparts' coupled effect. In summation, above Equation 4.4 may be stated in its full form as Equation 4.5 [105]:

$$\begin{pmatrix} \varepsilon_1 = \varepsilon_{xx} \\ \varepsilon_2 = \varepsilon_{yy} \\ \varepsilon_3 = \varepsilon_{zz} \\ \varepsilon_4 = \varepsilon_{yz} \\ \varepsilon_5 = \varepsilon_{zx} \\ \varepsilon_6 = \varepsilon_{xy} \end{pmatrix}_{mech} = \begin{bmatrix} 1 & 0 & 0 & 0 & 0 & 0 \\ M_{21} & M_{22} & M_{23} & M_{24} & 0 & 0 \\ M_{31} & M_{32} & M_{33} & M_{34} & 0 & 0 \\ M_{41} & M_{42} & M_{43} & M_{44} & 0 & 0 \\ 0 & 0 & 0 & 0 & M_{55} & M_{56} \\ 0 & 0 & 0 & 0 & M_{65} & M_{66} \end{bmatrix}_{\varepsilon} \begin{pmatrix} \bar{\varepsilon}_1 \\ \bar{\varepsilon}_2 \\ \bar{\varepsilon}_3 \\ \bar{\varepsilon}_4 \\ \bar{\varepsilon}_5 \\ \bar{\varepsilon}_6 \end{pmatrix}_{mech} + \begin{pmatrix} A_1 \\ A_2 \\ A_3 \\ A_4 \\ A_5 \\ A_6 \end{pmatrix}_{\varepsilon} \Delta T \tag{4.5}$$

The following equations apply to both micro and macro mechanical strains (Equation 4.6) [105]:

$$\varepsilon_{mech} = S\sigma \, , \overline{\varepsilon}_{mech} = \overline{S}\,\overline{\sigma} \tag{4.6}$$

Where σ represents the micro stress and S is the local compliance matrix at a certain internal point of UD. Equation 4.6 may be substituted into Equation 4.4 to form Equation 4.7 [105]:

$$S\sigma = M_\sigma \overline{S}\,\overline{\sigma} + A_\sigma \Delta T \tag{4.7}$$

where M_σ and A_σ are macro stress and temperature increment stress amplification factors, respectively. Because of the differences in material characteristics, the deformation of fiber and matrix is not constant as temperature varies, resulting in micro thermal stresses within the unit cells. Equation 4.8 has a full version that is quite close to inverse matrix of *S* multiplied of Equation 4.7:

$$\begin{pmatrix} \sigma_1 = \sigma_{xx} \\ \sigma_2 = \sigma_{yy} \\ \sigma_3 = \sigma_{zz} \\ \sigma_4 = \sigma_{yz} \\ \sigma_5 = \sigma_{zx} \\ \sigma_6 = \sigma_{xy} \end{pmatrix} = \begin{bmatrix} M_{11} & M_{12} & M_{13} & M_{14} & 0 & 0 \\ M_{21} & M_{22} & M_{23} & M_{24} & 0 & 0 \\ M_{31} & M_{32} & M_{33} & M_{34} & 0 & 0 \\ M_{41} & M_{42} & M_{43} & M_{44} & 0 & 0 \\ 0 & 0 & 0 & 0 & M_{55} & M_{56} \\ 0 & 0 & 0 & 0 & M_{65} & M_{66} \end{bmatrix}_\sigma \begin{pmatrix} \overline{\sigma_1} \\ \overline{\sigma_2} \\ \overline{\sigma_3} \\ \overline{\sigma_4} \\ \overline{\sigma_5} \\ \overline{\sigma_6} \end{pmatrix} + \begin{pmatrix} A_1 \\ A_2 \\ A_3 \\ A_4 \\ A_5 \\ A_6 \end{pmatrix}_\sigma \Delta T \tag{4.8}$$

Micro stresses at each location within the fiber and matrix may be calculated from external ΔT and macro stresses using stress amplification factors that vary throughout fiber and matrix in Equation 4.8.

The stress components at critical points can be taken for fiber, matrix and interphase region and failure formation can be searched. In Figure 4.4 critical points on different geometry RVE elements can be seen.

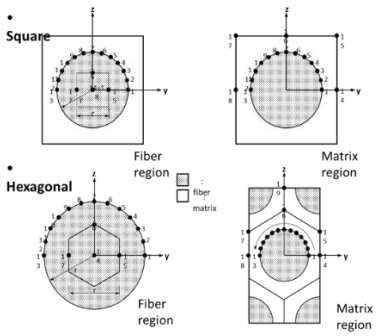

Figure 4.4 : Critical stress points for fiber, matrix and interphase region in RVE

4.1.2 Trans-scale strain ampflification method

In this method finite element analysis is performed on a representative volume element based on the detailed structure of fiber/matrix to determine the effective elastic constants and thermal expansion coefficients at micro-scale.

The material behaviors at the microscale level are taken into account in this newly designed PFA procedure (Figure 4.5). The following is a detailed explanation of each stage of this method [107–109]:

1. To perform micromechanics-based finite element analysis (FEA), thermodynamic characteristics for cryogenic constituents are first determined using a combination of experiment and numerical modeling. Then, depending on the material's microstructure characteristics, a suitable RVE is chosen. The corresponding thermodynamic characteristics of a single ply of composite in the microscale are then determined using FEA for constituents in the microscale using the periodic symmetric boundary. Meanwhile, for each unit strain and thermal loading, the microscopic stress field of the cell is determined.

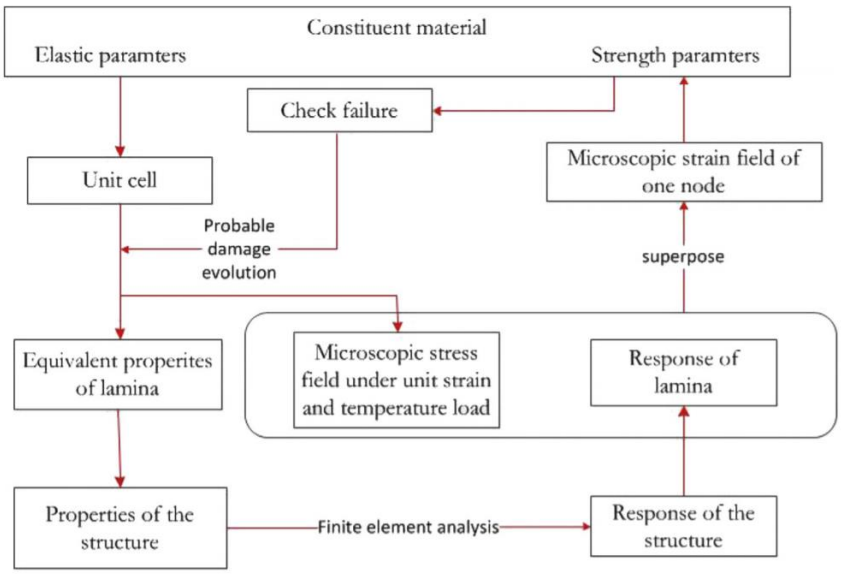

Figure 4.5 : Steps for the trans-scale PFA analysis [108].

2. Create a finite element analysis model of a filament-wound composite based on the characteristics of the composite lamina.

3. Get composite theory to get structural reactions at the macroscale and microscale levels.

4. Calculate the microscopic stress field of one spot on the lamina under real load by combining the microscopic strain field of this point with the microscopic stress field acquired in the previous step. After obtaining the constituent's stress field, a microscale strength study will be performed. Based on the strength criteria for matrix and fiber, and the possible damage development, determination of a single "micro-element" strength requirement can be made.

The objective of RVE micromechanics is to establish the connection between stress and strain by dividing the mesh to discretize the structure. The initial step involves obtaining micro stress-strain fields, followed by employing a homogenization approach to determine macroscopic stress-strain fields. This approach offers the advantage of obtaining complete stress-strain fields at the micro-scale, enabling microscale strength prediction and composite structure design. Consequently, modeling utilizing mesomechanics theories is applied to explore the thermodynamic characteristics of cryogenic composite tanks. The stress-strain relationships of the composite material are as follows [107–109]:

$$\begin{pmatrix}\sigma_1\\ \sigma_2\\ \sigma_3\\ \tau_{23}\\ \tau_{31}\\ \tau_{12}\end{pmatrix}=\begin{bmatrix}\bar{C}_{11}(T) & \bar{C}_{12}(T) & \bar{C}_{13}(T) & 0 & 0 & 0\\ \bar{C}_{12}(T) & \bar{C}_{22}(T) & \bar{C}_{23}(T) & 0 & 0 & 0\\ \bar{C}_{13}(T) & \bar{C}_{23}(T) & \bar{C}_{33}(T) & 0 & 0 & 0\\ 0 & 0 & 0 & \bar{C}_{44}(T) & 0 & 0\\ 0 & 0 & 0 & 0 & \bar{C}_{55}(T) & 0\\ 0 & 0 & 0 & 0 & 0 & \bar{C}_{66}(T)\end{bmatrix}\begin{pmatrix}\overline{\varepsilon_1}-\bar{\alpha}_1(T)\Delta T\\ \overline{\varepsilon_2}-\bar{\alpha}_2(T)\Delta T\\ \overline{\varepsilon_3}-\bar{\alpha}_3(T)\Delta T\\ \overline{\gamma_{23}}-\bar{\alpha}_{23}(T)\Delta T\\ \overline{\gamma_{31}}-\bar{\alpha}_{31}(T)\Delta T\\ \overline{\gamma_{12}}-\bar{\alpha}_{12}(T)\Delta T\end{pmatrix} \tag{4.9}$$

where $C_{ij}(T)$ and $\alpha_i(T)$ are unsolved temperature-dependent parameters. An adaptable RVE must be chosen initially at the micro-scale. The parameters above are then solved using seven sets of unit loads. All $C_{ij}(T)$ will be produced by applying unit strain loading without thermal loading with six mechanical unit loadings. The $\alpha_i(T)$ calculated by loading the RVE with unit thermal load without strain loading.

The RVE serves as a tool to derive equivalent mechanical characteristics for cryogenic composites. Alongside material properties, the calculation of microscopic stress fields under unit strain and thermal loading is crucial. The information from these physical fields becomes unit microscopic fields for the subsequent study of structural reactions. Macroscopic and microscopic strain are determined through modeling at a lower level to generate microscopic stress fields for the structure under varied loads. The RVE is further utilized to calculate the thermodynamic characteristics of cryogenic

composites. In classical laminate theory, these conclusions are employed as characteristics of homogeneous materials, enabling the construction of the cryogenic composite model. While standard finite element analysis can determine structural responses on a single-ply scale, obtaining the response of fibers and resins at the microscale is challenging with traditional analysis. However, comparable analysis is achievable. To obtain stress and strain fields of fiber and resin at a specific location within the composite, a trans-scale hierarchical analysis based on equivalent analysis is employed. The approach involves obtaining a microscopic stress field of a point coupled with unit stress fields based on strain response at the micro-scale, followed by assessing the fiber and resin at the same point. The superposition formula is as follows:

$$\{\sigma^u\}^e = [H]^e\{\varepsilon^M\} + \Delta T\{S\}^e \tag{4.10}$$

where $\{\sigma^u\}^e$ is the unit cell's microscopic stress field at particular macroscopic stresses and temperatures $[H]^e$ is the unit microscopic stress field of a unit cell under unit strain loading produced by applying the previously described boundary conditions to a hexagonal unit cell, and $\{\varepsilon^M\}$ is macroscopic strains determined by traditional finite element analysis, which is a 6x1 column. ΔT is the change of the temperature, $\{S\}^e$ is the stress field on the fiber-matrix scale calculated by unit thermal loading case.

4.1.2.1 Constituent based failure criterion

After obtaining the stress and strain fields at the microscale level, it is essential to determine the strength of the fiber and resin. Given that the resin becomes rigid and brittle at cryogenic temperatures and the fiber is predominantly oriented within the matrix, with damage occurring perpendicular to the fiber, the maximum stress criterion is employed to identify the strength of the fiber and resin. The failure criterion for the fiber is then:

$$-X_f^C < \sigma_{f1} < X_f^T \tag{4.11}$$

Where X_f^T, X_f^C fibers tensile and compressive strength values, σ_{f1} is maximum axial microstress value on fiber.

The resin materials are generally isotropic however the tensile strength T_M and compressive strength C_M can be different. According the literature matrix fracture

generally based on Von Mises stress σ_{vM} and first invariant value I_1. The invariant values for matrix can be calculated as (Equation 4.12 and Equation 4.13):

$$I_1 = \sigma_1 + \sigma_2 + \sigma_3$$
$$I_2 = \sigma_1\sigma_2 + \sigma_2\sigma_3 + \sigma_3\sigma_1 - (\sigma_4^2 + \sigma_5^2 + \sigma_6^2) \quad (4.12)$$
$$\sigma_{vM} = \sqrt{I_1^2 - 3I_2}$$

$$\sigma_{vM} \geq X_{mt} \quad (4.13)$$

4.1.2.2 Validation

The validation of the developed code is satisfied according to references [100,109]. A python script written for a Sqaure RVE with periodic boundary conditions with IM7 fiber and 977-3 resin system. All results are below the %10 error margin.

4.1.2.3 Micro rve fea analysis

Hexagonal array is selected for RVE analysis with volume fraction ratio 0.6. Six unit loadings performed for hexagonal RVE and micro stress distributions were obtained by using ABAQUS commercial software. The periodic boundary conditions were applied on RVE by using python code. These analysis have been done for 6 different materials systems and 30 analysis have been completed in total for micro analysis.

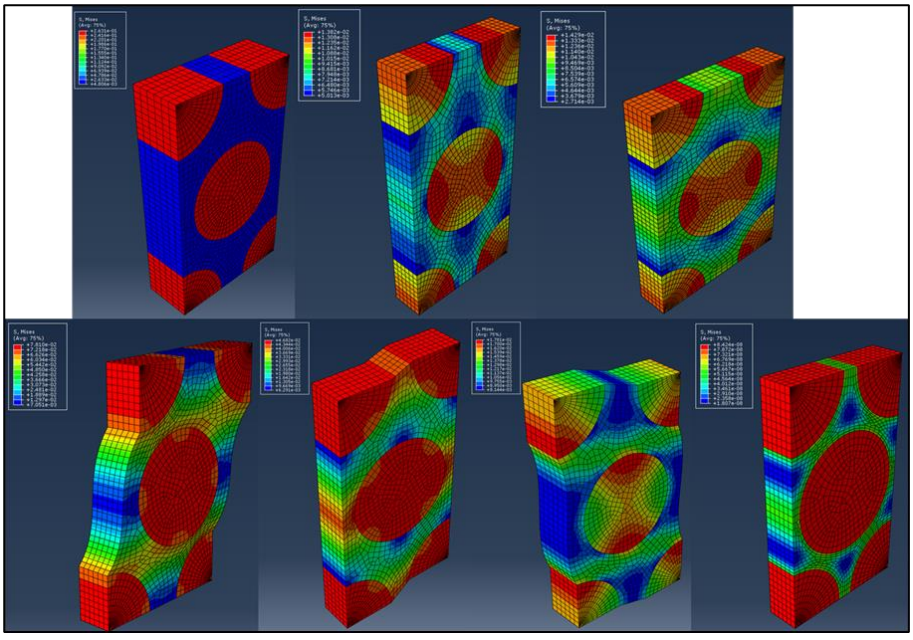

Figure 4.6 : Unit loadings of IM7/977-3 material RVE VM stress distribution.

The micro model contains 20,904 solid elements for matrix region and 13,442 solid elements for fibers (Figure 4.6). The 6 components of micro stress results have been gathered for each element and stored for Matlab code prepared. Also by using these unit loadings equivalent orthotropic material properties for each constituent system calculated.

4.1.2.4 Material properties determination for macro analysis

A49 12K DowAksa carbon fibers and different epoxy systems was used for determining material properties to use in macro analysis. The epoxy properties under room and cryogenic temperatures have been taken from the previous three-point bending test results. Using three-point bending results for determining Young's modulus and strength properties of resin is not accurate but for gaining a foresee about orthotropic material differences in laminate according to resin properties, this values were used.

Also IM7/977-3 fiber epoxy system is used for comparing commercial epoxy performances with a cryogenic fiber-epoxy system. The material properties have been obtained for RT and cryogenic temperatures. The thermal expansion coefficient values have been assumed as standart epoxy values.

	Name	Values[0]	Values[1]	Values[2]	Values[3]	Unit
	Parameters					
	Temperature	22	-60	-120	-180	C
	Engineering Const					
	E1	1.1409E+05	1.1409E+05	1.1409E+05	1.1409E+05	MPa
	E2	4.0211	5.3612	9.3808	13.399	MPa
	E3	3.787	5.0491	8.8349	12.62	MPa
	G12	1.6125	2.1499	3.7617	5.373	MPa
	G23	1.4159	1.8878	3.3033	4.7183	MPa
	G31	1.6073	2.1429	3.7495	5.3555	MPa
	nu12	0.25576	0.25583	0.25587	0.25587	
	nu13	0.25657	0.2564	0.25642	0.25648	
	nu23	0.40014	0.40013	0.40013	0.40014	
	Density					
	rho	1.48E-09	1.48E-09	1.48E-09	1.48E-09	t mm^-3
	Thermal Expansion					
	aX	-9.9963E-07	-9.9956E-07	-9.993E-07	-9.9912E-07	C^-1
	aY	3.466E-05	3.1806E-05	2.9364E-05	2.6656E-05	C^-1
	aZ	3.5136E-05	3.2227E-05	2.9738E-05	2.6978E-05	C^-1

Figure 4.7 : ANSYS material designer output.

The constituent properties of elasticity, thermal expansion and thermal conductivity is defined as a function of temperature (T) both for resin and fiber. ANSYS Material Designer module is used for determining orthotropic lamina properties (Figure 4.7).

Except for the 977-3 epoxy system, the other epoxies material properties are considered as linear with temperature change.

The thermal expansion values of each matrix system can be seen in Table 4.1. The thermal expansion values are extrapolated from room temperature by referencing 977-3 system values which are taken from literature. As it is explained in next sections thermal expansion change with temperature highly effects stress distribution on matrix.

Table 4.1 : Thermal expansion values of matrix systems.

Materials	RT	CRYO
	α (10e-6/K)	
CEA 11546	56.5	14
CEA 5025	71	25
T7109-19	59	14
T7110	31	0.5
301_2	61	14
301_2FL	56.5	14
977_3	56.5	14

The main orthotropic properties of fiber-epoxy systems can be seen in Table 4.2. The fiber direction properties depends on the fiber type. IM7 has higher rigidity than A49-Dow-Aksa carbon fiber. The temperature change effect is minimal on fiber direction modulus. The transverse direction properties is determined by epoxy properties. The 977-3 epoxys system provides higher transverse modulus value in room temperature while the value is same with other epoxy systems in cryogenic temperature. Also the transverse modulus of T7109_19 and T7110 systems are very low.

Table 4.2 : Orthotropic material properties gathered by homogenization process.

Materials	RT	CRYO	RT	CRYO
	E1(Gpa)		E2, E3(Gpa)	
IM7-997_3	159.1	159.8	8.49	10.7
A49-CEA11546	150.7	152.3	5.24	10.5
A49-CEA5025	151	152.9	6.36	11.7
A49-T7109-19	150	151.7	0.13	9
A49-T7110	150.1	154.9	1.37	14.5
A49-301_2	151.08	152.5	6.82	10.8
A49-301_2FL	150.8	152.7	5.48	11.1

4.1.2.5 Macro fea analysis

Three different tank geometries have been investigated as spherical dome tank, elliptical dome tank and sphere tank. The composite layups have been designed for pressure 10bar in room temperature and the cryogenic LOX effect was investigated for these layups. Also by using Elliptical dome 6 different material responses evaluated with trans-scale analysis.

Table 4.3 : FE analyzed tank geometries and properties.

Tank Geometry	Composite Layup	Operating Pressure (bar)	Operating Temperature(˚C)
Spherical Dome	±11.5, ±48,± 90	10	-180
Elliptical 2:1 Dome	±11.5, ±48, ± 90	10	-180
Sphere	±11.5, ±30	10	-180

The 6 macro strain components for each ply orientation has been gathered from ANSYS at fiber coordinate system. These results then used in Matlab code. For each material system fiber and matrix principal stresses and matrix Von Mises stresses were obtained.

Elliptical dome

The macro model contains 26,992 shell composite elements and 20,264 solid elements for polar bosses (Figure 4.8). For first phase boss and composite interface assumed as bonded. Nonlinear geometrical effects considered. 5 of 7 materials has convergence with these layups for 10 bar pressure and cryogenic temperature. The T7109-19 and T7110 system has a very low elastisicty modulus at room temperature for that reason the analysis could not converge for considered layup and loadings. This shows that low elastisicity materials could not bear these loadings with these ply layup and not suitable for pressure vessel production at room temperature conditions. An example of total deformation profile of the tank can be seen in Figure 4.9.

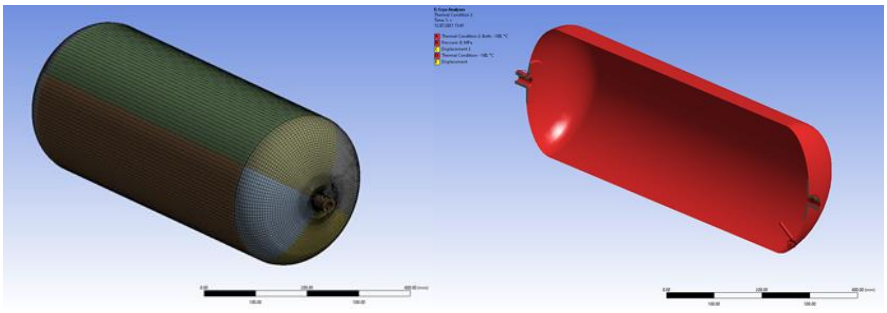

Figure 4.8 : Elliptical dome tank FEA model and thermomechanical loadings.

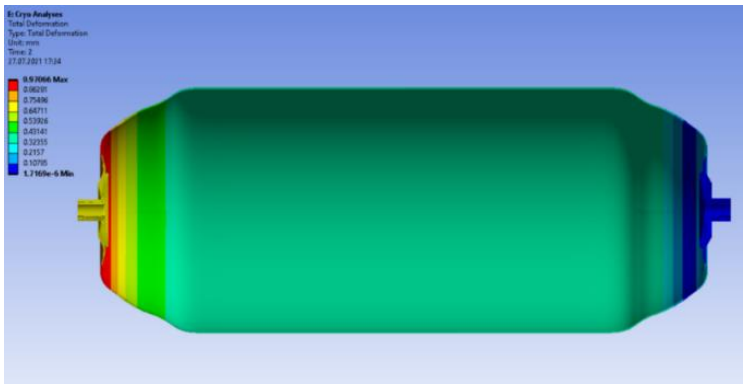

Figure 4.9 : Total deformation contour of elliptical dome tank.

4.1.2.6 Spherical dome

The macro model contains 27,437 shell composite elements and 20,264 solid elements for polar bosses (Figure 4.10). For first phase boss and composite interface assumed as bonded. Nonlinear geometrical effects considered. An example of total deformation profile of the tank can be seen in Figure 4.11.

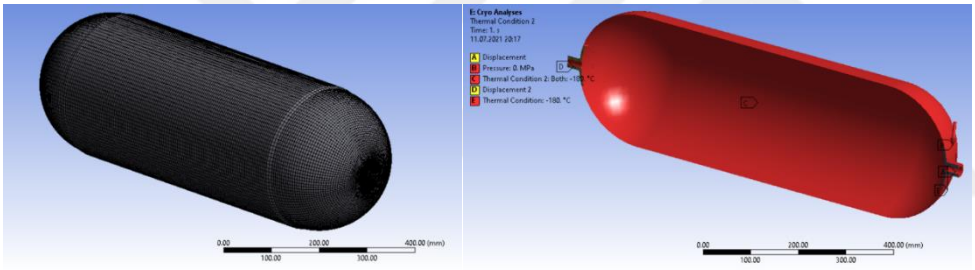

Figure 4.10 : Spherical dome tank FEA model and thermomechanical loadings.

Figure 4.11 : Total deformation contour of spherical dome tank.

4.1.2.7 Sphere

The macro model contains 13,035 Shell composite elements and 20,264 solid elements for polar bosses (Figure 4.12). For first phase boss and composite interface assumed

as bonded. Nonlinear geometrical effects considered. An example of total deformation profile of the tank can be seen in Figure 4.13.

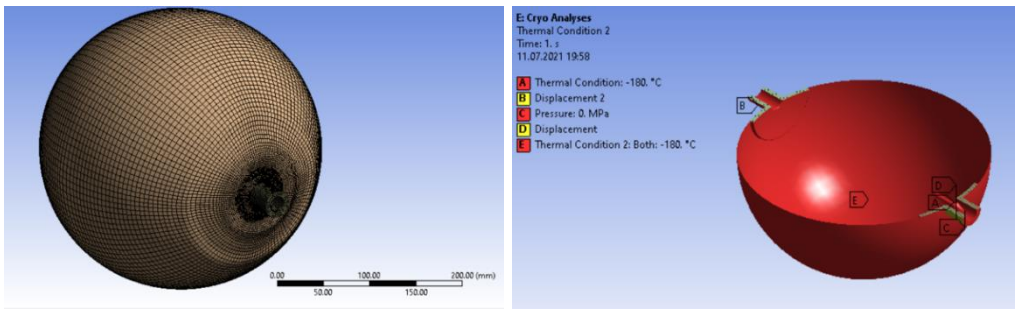

Figure 4.12 : Sphere tank FEA model and thermomechanical loadings.

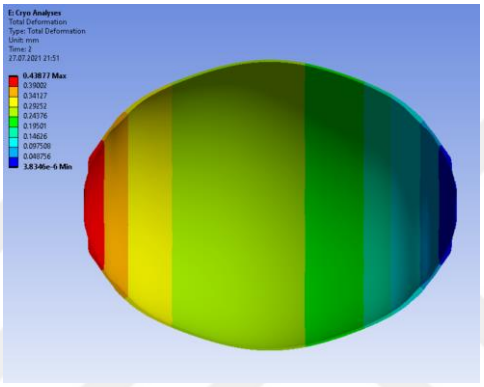

Figure 4.13 : Total deformation contour of sphere tank.

A matlab code have been developed for trans scale calculations between micro and macro FEA models. The macro stresses are derived from macro FEA analyses with .txt or .csv extension files and these files are imported to the calculator. Also the strain values from micro FEA models gathered in the same way. The matrix calculations are done by Matlab code as described above section for each macro element and maximum/minimum stresses for constituents are calculated.

4.1.2.8 Results

Figure 4.14 and 4.15 summarizes the trans-scale analysis results of each constituents for all tank geometries. Each ply's constituents calculated separately and reported.

As it's expected sphere tank geometry has the minimum and elliptical geometry has the maximum stress distribution on it's layup both on fiber and matrix.

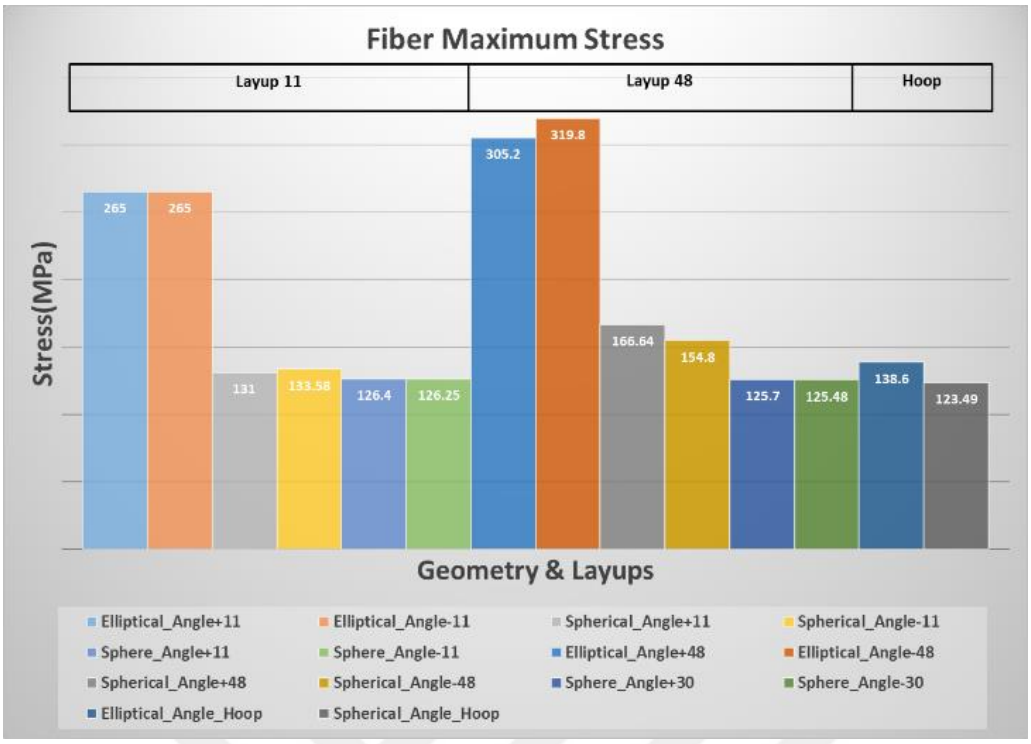

Figure 4.14 : Fiber maximum stress values for each defined ply angles and geometries

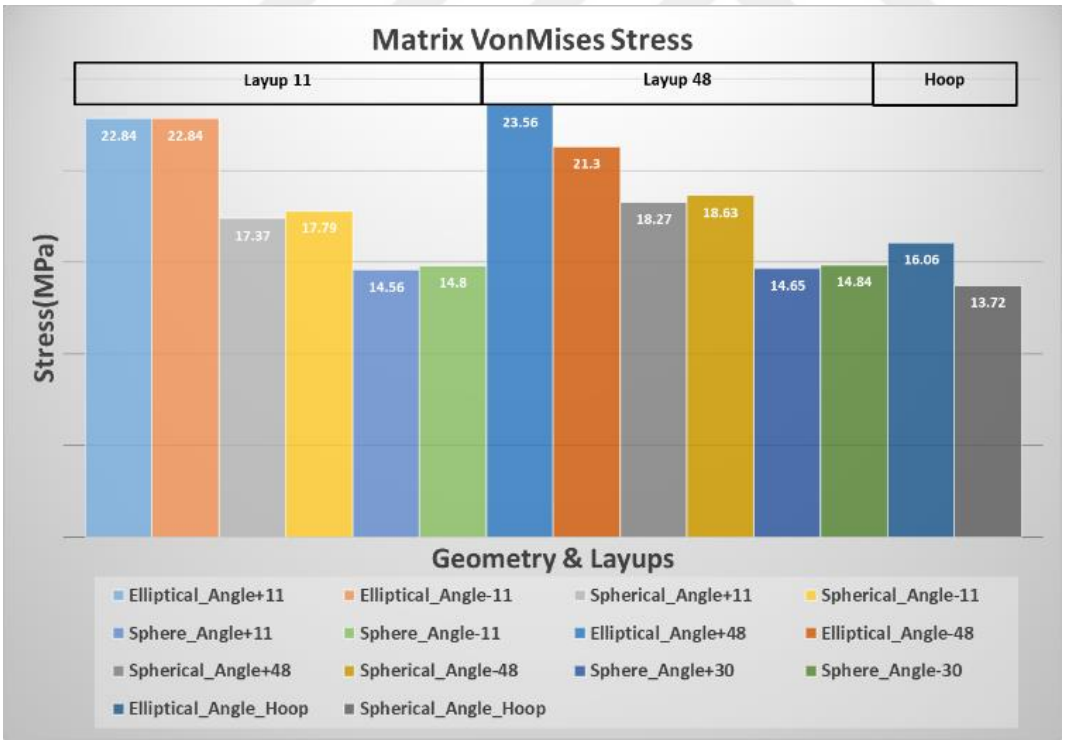

Figure 4.15 : Matrix maximum stress values for each defined ply angles and geometries

Figures 4.16, 4.17 and 4.18 summarizes the different material performances with elliptical dome geometry for each ply angles.

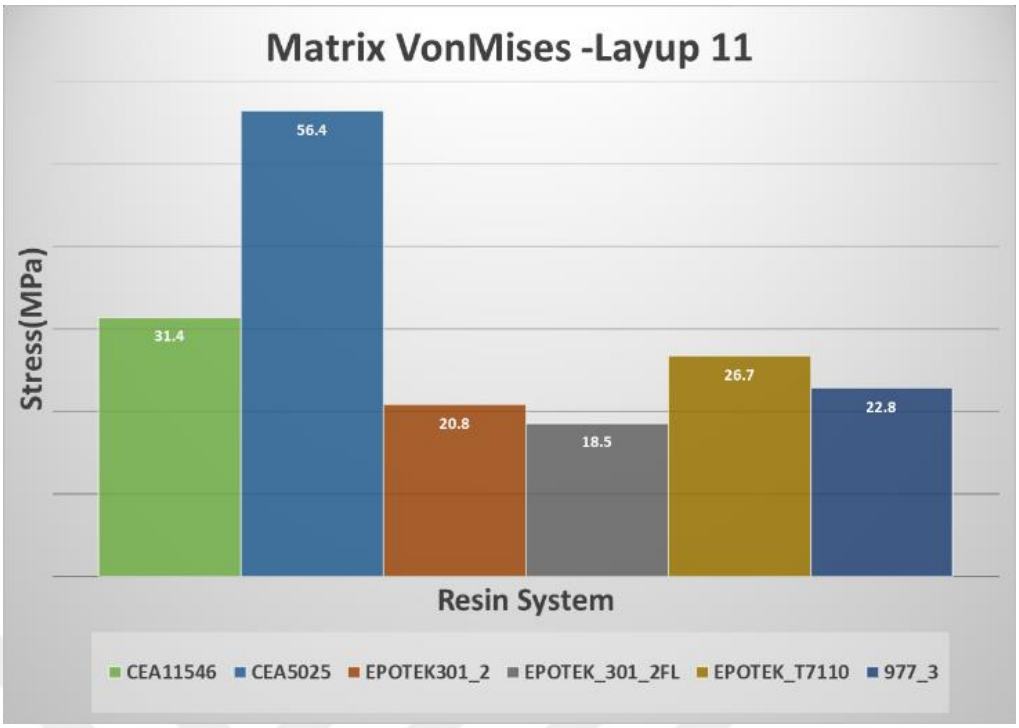

Figure 4.16 : Matrix VonMises stress values of different epoxies for ±11 ply

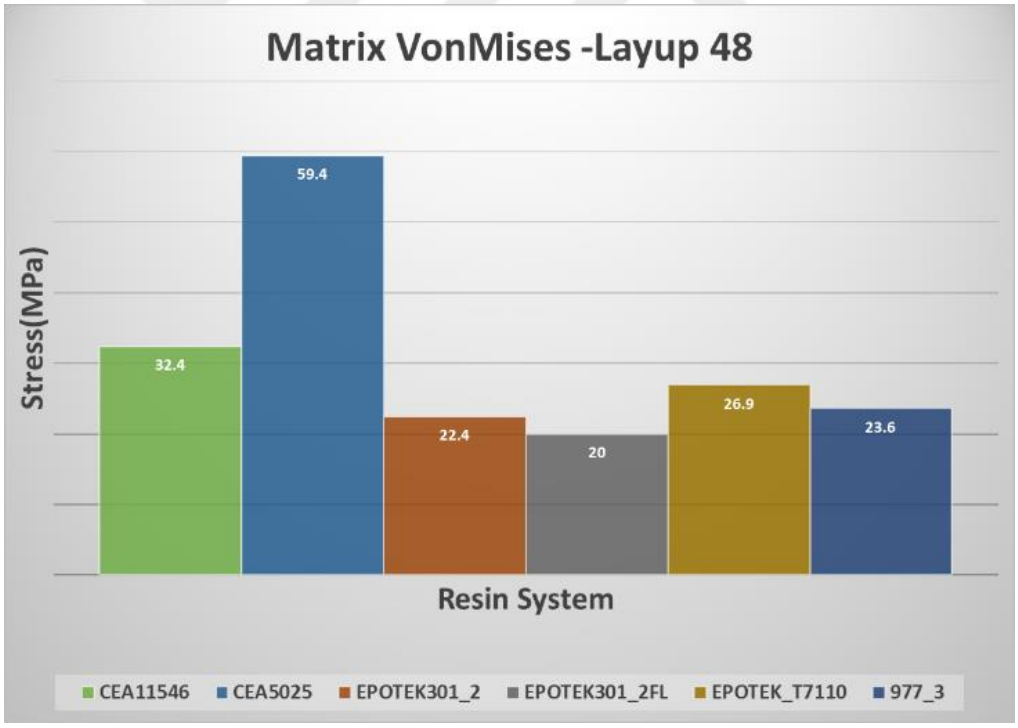

Figure 4.17 : Matrix VonMises stress values of different epoxies for ±48 ply

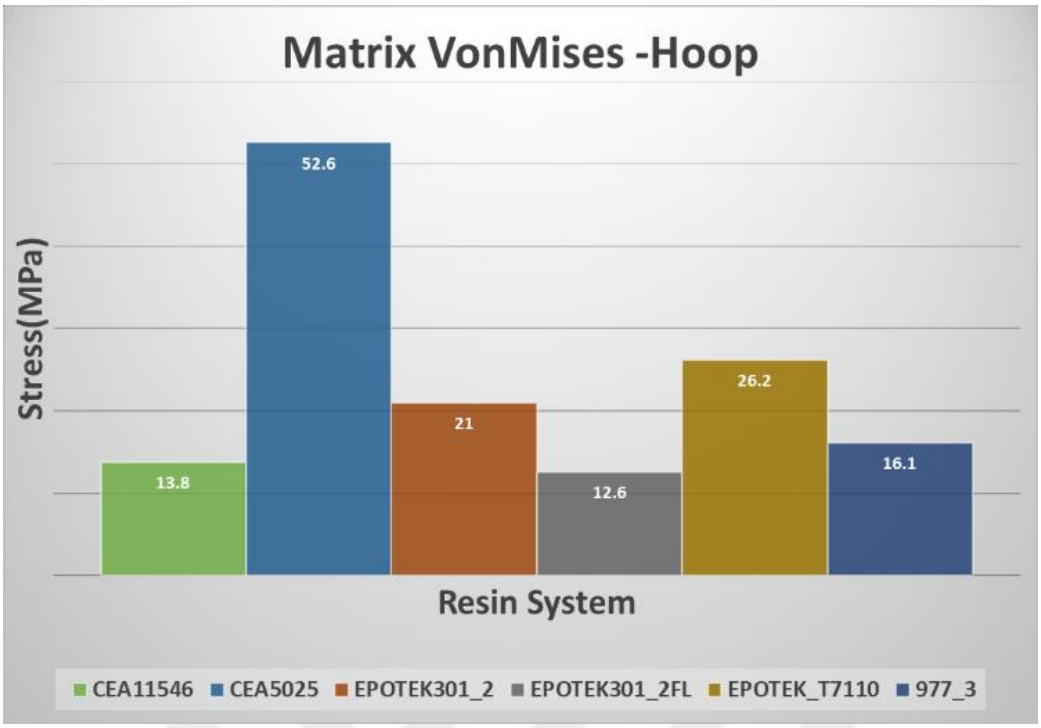

Figure 4.18 : Matrix VonMises stress values of different epoxies for hoop ply

The best system in case of Von Mises stress is Epotek 301-2FL. The thermal expansion coefficient of this system is 14e-5 (1/K) at −218˚C, also the modulus increase at cryogenic temperature is about %100, which is not dramatic as other systems. This implies that, taking Von Mises stress as criteria, the modulus and thermal expansion coefficient change of system when subjected to the cryogenic temperatures are critical. Having both values small gives much less Von Mises value.

But in case of taking the maximum stress value as criteria for matrix, T7110 is the best epoxy system. The thermal expansion of T7110 resin system is very low at cryogenic temperatures (5e-7 @ −218˚C) but the resin gets brittle and modulus shows high increasing. Having low thermal expansion value provides low CTE mismatch between matrix and fiber, and matrix-fiber working with harmony. Also the change of thermal expansion value with temperature is smaller than the other epoxies, this provides less difference thermal expansion behaviour between room and cryogenic temperatures.

According to these calculations only Epotek 301-2, 301-2FL and IM7-977-3 matrix systems can bear the cryogenic temperature and 10 bar pressure loading with given geometry. The 301-2 and 301-2FL systems can be alternatives for 977-3 resin.

This analysis should be improved with considering nonlinear material behaviour of constituents, interface properties of constituents and also intra-crack propagation

should be considered. In first phase only initial crack formation was researched for in plane conditions with linear material behaviour. The nonlinear material behaviour becomes important at transient heat transfer case. In real life the heat transfer from room temperature to cryogenic conditions will be transient and material nonlinearities will effect all crack formations.

4.1.2.9 Parametrization

Following the microscale analysis of the tested specimens, the trans-scale method has been parametrized to search material property change effect for thermal loading.

The parameters and their assigned discrete values can be seen in Table 4.4. Six unit loading and 1 unit thermal loading RVE input file (.inp) paramterized according the these parameters. An abaqus script file has been prepared as .psf file, which includes parameters, parameter values, parameter combination type and input file executions.

Table 4.4 : Material Parameters for each Constituent.

MATRIX		FIBER	
E(MPa)	CTE(1/K)	E1 (MPa)	CTE-Transverse
1000	1.00E-05	230000	1.00E-06
2000	3.00E-05	294000	5.00E-06
4000	5.00E-05	436000	1.00E-05
7000	-	-	-

These parameters gave 108 different combinations for each RVE loading. By applying 7 unit loadings 756 RVE analyses have completed. The RVE geometry has a %60 V_f ratio with hexagonal pattern. The stress values of each elements have been obtained for each constituents with another script file which provides results files for each parametrized input execution.

The macro strain levels have been gathered from the reference [100]. These macro strain contain only thermal load effects. Then macro and micro results have been imported in MATLAB with another script file and maximum, minimum and VonMises stress values have been generated for each parametric combination.

Results

In overall, when the thermal load is most dominant effect, parametric results clearly points that the most critical constituent property for cryogenic thermal load is the

matrix thermal expansion coefficient value and it's change with temperature. The lower matrix CTE ensures that the matrix stress levels will be reduced.

The lower relative difference between matrix CTE and the transverse CTE of the fiber also provide decreased matrix stress levels.

As it's expected lower matrix rigidity gives lower matrix stress levels.

The Table 4.5 below shows desired combination for the minimum stress levels on matrix.

Table 4.5 : Desired combination for the minimum stress levels on matrix.

Consituent	Property	Value	Dominance Level on Stress
Matrix	CTE	Low	Very High
	Young's Modulus	Low	High
Fiber	Transverse CTE	High	Moderate
	Longitudinal Young's Modulus	Intermediate	Not have significant effect

5. COMPOSITE VESSEL WITH LINER INVESTIGATION

As mentioned in the Introduction section, composite pressure vessels can be categorized into five different types.

- Type I – Full Metal
- Type II – Metal Hoop Composite Overwrapped
- Type III –Metal liner Composite Overwrapped
- Type IV- Polymer liner Composite Overwrapped
- Type V- Linerless composite tank

Currently, Type-IV cryogenic tanks are widely studied worldwide. However, based on the production capabilities of the author, this study focuses on the manufacturing of Type-II and Type-V tanks.

The production of a cryogenic vessel with a liner necessitates the investigation of insulation materials and the coefficient of thermal expansion (CTE) compatibility of the liner with the composite case.

5.1 Thermal Research

5.1.1 Insulation

For the design of the pressure vessel with a liner, an investigation was conducted to identify the necessary materials to protect the composite structure from cryogenic temperatures by creating a thermal barrier. In this context, even if the inner liner body is made of metal, the goal is to ensure that the composite surface temperature does not exceed −40 ~ −50˚C, thanks to the interlayer insulation (see Figure 5.1). Additionally, the inner liner thickness needs to be minimized to avoid excess weight.

To address the basic conduction problem, two different materials, bromine gas (halogen/LOX compatible) and graphite, were selected to observe the thermal conductivity effect when the insulation surface is exposed to liquid oxygen temperature (Equation 4.1). Bromine has very low thermal conductivity (k= 0.04

W/mK), while graphite has very high thermal conductivity (k=168 W/mK) [112]. With bromine insulation, the composite surface experiences a temperature of 6.8˚C, whereas with graphite insulation, the same surface experiences the temperature of liquid oxygen (-183 ˚C).

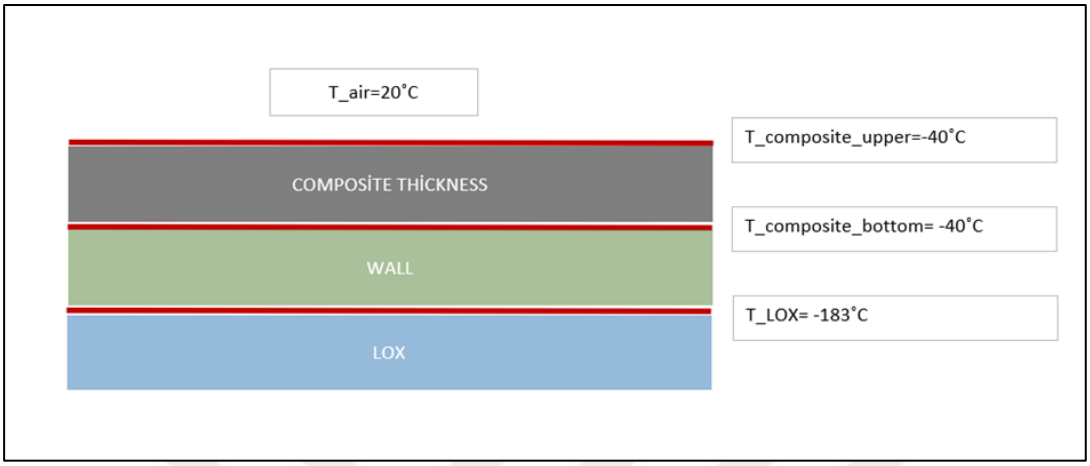

Figure 5.1 : Demonstraion of interlayer insulation for preventing composite from cryogenic temperatures.

$$q = k * \frac{\Delta T}{L_{thickness}} \tag{4.1}$$

q : Heat Flux (W/m^2K)

k: Thermal conductiviy (W/mK)

$L_{thickness}$: Thickness (m)

ΔT : Temperature change accross thickness

The lower the heat flux, the higher the temperature on the composite surface. A 10mm thickness of bromine gas is taken as a reference for calculating the reference heat flux to maintain the composite bottom surface at −40˚C. The value of the reference heat flux is found to be 5.72e-5W/mm^2K.

The thickness of all kinds of materials can be determined with a simple calculation prepared in Microsoft Excel to provide this reference q value (see Table 5.1). It can be observed that the maximum thermal barrier efficiency can be achieved by vacuum insulation, as it is already employed in large-scale cryogenic metal pressure vessels.

Table 5.1 : Potential insulation material thicknesses and equal aluminum thickness for reference heat flux [112].

Material	k (W/mK) @25C	T_wall upper (˚C)	T_wall bottom (˚C)	q (W/mm^2)	t_wall (mm)	Density (kg/m^3)	Areal Weight (kg/m^2)	Equal Aluminum Thickness(mm)
Vacuum	0	-40	-183	5.72E-05	0.0	0	0	0.0
Perlite, vacuum	0.00137	-40	-183	5.72E-05	3.4	100	342.5	0.1
Bromine (gas)	0.004	-40	-183	5.72E-05	10.0	3100	31000	11.5
Carbon dioxide (gas)	0.0146	-40	-183	5.72E-05	36.5	2000	73000	27.0
Silica aerogel	0.02	-40	-183	5.72E-05	50.0	100	5000	1.9
Urethane foam/Low density	0.021	-40	-183	5.72E-05	52.5	48	2520	0.9
Cotton wool	0.029	-40	-183	5.72E-05	72.5	90	6525	2.4
Polystyrene, expanded styrofoam	0.03	-40	-183	5.72E-05	75.0	46	3450	1.3
Polyurethane foam	0.03	-40	-183	5.72E-05	75.0	140	10500	3.9
Perlite, atmospheric pressure	0.031	-40	-183	5.72E-05	77.5	1100	85250	31.6
Styrofoam	0.033	-40	-183	5.72E-05	82.5	50	4125	1.5
Feathers	0.034	-40	-183	5.72E-05	85.0	4000	340000	125.9
Kapok insulation	0.034	-40	-183	5.72E-05	85.0	290	24650	9.1
Cotton	0.04	-40	-183	5.72E-05	100.0	450	45000	16.7
Felt insulation	0.04	-40	-183	5.72E-05	100.0	140	14000	5.2
Fiberglass	0.04	-40	-183	5.72E-05	100.0	14	1400	0.5
Glass, wool Insulation	0.04	-40	-183	5.72E-05	100.0	16	1600	0.6
Slag wool	0.042	-40	-183	5.72E-05	105.0	70	7350	2.7
Cork board	0.043	-40	-183	5.72E-05	107.5	200	21500	8.0
Polystyrol	0.043	-40	-183	5.72E-05	107.5	15	1612.5	0.6
Cork, re-granulated	0.044	-40	-183	5.72E-05	110.0	180	19800	7.3
Foam glass	0.045	-40	-183	5.72E-05	112.5	485	54562.5	20.2
Rock Wool insulation	0.045	-40	-183	5.72E-05	112.5	22	2475	0.9
Rubber, cellular	0.045	-40	-183	5.72E-05	112.5	130	14625	5.4
Balsa wood	0.048	-40	-183	5.72E-05	120.0	120	14400	5.3
Fiber insulating board	0.048	-40	-183	5.72E-05	120.0	300	36000	13.3
Calcium silicate	0.05	-40	-183	5.72E-05	125.0	170	21250	7.9
Hairfelt	0.05	-40	-183	5.72E-05	125.0	1300	162500	60.2
Neoprene	0.05	-40	-183	5.72E-05	125.0	1230	153750	56.9
Paper	0.05	-40	-183	5.72E-05	125.0	250	31250	11.6
Polyester	0.05	-40	-183	5.72E-05	125.0	1380	172500	63.9
Diatomaceous earth (Sil-o-cel)	0.06	-40	-183	5.72E-05	150.0	250	37500	13.9
Vermiculite granules	0.065	-40	-183	5.72E-05	162.5	172	27950	10.4
Cork	0.07	-40	-183	5.72E-05	175.0	240	42000	15.6
Magnesia insulation (85%)	0.07	-40	-183	5.72E-05	175.0	3200	560000	207.4
Soot	0.07	-40	-183	5.72E-05	175.0	2000	350000	129.6

As observed in Table 5.1, two criteria can be considered for selecting insulation materials. The first criterion is the required thickness to satisfy temperature, and the second is the equivalent aluminum thickness for this insulation thickness, which can be used as a weight comparison criterion (with 2mm taken as the maximum value). From the table, it is apparent that there is no conventional solid insulation material under 50mm thickness that is required to provide the reference heat flow. Perlite particles under vacuum conditions appear as a promising candidate for this design. However, as indicated in reference [113], perlite particles' thermal conductivity increases drastically (about 100% with 1 bar pressure). This is illustrated in Figures 5.2, 5.3, and 5.4 from [113], leading to a loss of all the advantages of perlite's low thermal conductivity. The LOX pressure vessel for sounding rockets will operate at pressures around 50-70 bars, and this condition is not suitable for the thermal conductivity of perlite particles. If turbopump systems can be used for pressurization, LOX pressure vessel pressure values can be decreased to 5-10 bars.

With silica aerogel and urethane foam, the desired condition can be achieved with a 50mm thickness and a low equivalent aluminum thickness. However, the same pressure problem will arise as with perlite particles. As evident here, it does not seem effective to prevent the cryogenic temperature level from reaching the composite with the insulation material in a filament-wound pressure vessel unless the pressure value is low enough.

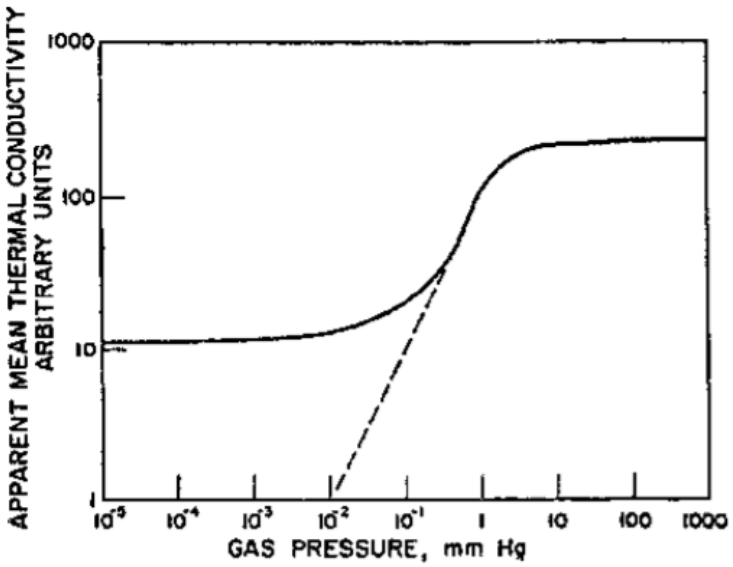

Figure 5.2 : Changes in the apparent thermal conductivity of an insulating powder as the pressure of the interstitial gas is altered [113].

Powder	Remarks	Density (g/cm^3)	Gas pressure (mm Hg)	Conductivity [$\mu W/(cm\ K)$]
Silica aerogel	Chemically prepared	0.10	$<10^{-4}$	21 ± 1
	250 A	0.10	628 (N_2)	196 ± 5
		0.10	628 (He)	620 ± 10
		0.10	628 (H_2)	800 ± 10
	+10% free silicon dust, by weight	0.11	$<10^{-4}$	18 ± 1
Silica	flame prepared,	0.06	$<10^{-4}$	21 ± 1
	150–200 A	0.06	630 (N_2)	185 ± 5
Perlite, expanded	+30 mesh	0.06	$<10^{-4}$	21 ± 0.5
	+30 mesh	0.10	$<10^{-4}$	18 ± 0.5
	+30 mesh	0.10	628 (N_2)	332 ± 5
	+30 mesh	0.10	628 (He)	1270 ± 10
	+30 mesh	0.10	628 (H_2)	1460 ± 20
	−30 + 80 mesh	0.13	$<10^{-4}$	12 ± 0.5
	−30 + 80 mesh	0.13	628 (N_2)	325 ± 5
	−30 + 80 mesh	0.13	628 (He)	1260 ± 20
		0.13	628 (H_2)	1450 ± 20
	−80 mesh	0.14	$<10^{-4}$	10 ± 0.5
	−80 mesh	0.14	628 (N_2)	350 ± 5
	−80 mesh	0.14	628 (He)	1350 ± 10
	−80 mesh	0.14	628 (H_2)	1453 ± 20
	−30 mesh	0.14	$<10^{-4}$	10 ± 0.5
Diatomaceous earth	1–100 μm	0.24	$<10^{-4}$	16 ± 0.5
		0.25	$<10^{-4}$	14 ± 0.5
		0.29	$<10^{-4}$	10 ± 0.5
Alumina, fused	−50+100 mesh	2.0	$<10^{-4}$	18 ± 0.5
Alumina, laminar	0.1–10 μm	0.07	$<10^{-4}$	23 ± 0.5
Mica, expanded	−20 + 30 mesh 30%	0.15	$<10^{-4}$	18 ± 0.5
	−30 + 15 mesh 70%	0.15	628 (N_2)	503 ± 10
		0.15	628 (He)	1500 ± 20
Lampblack		0.2	$<10^{-4}$	12.5 ± 0.5
Charcoal peach pits	20–30 mesh	0.49	$<10^{-4}$	18 ± 1
Carbon + 7% ash[b]	30% < 44 μm	0.2	$<10^{-4}$	6 ± 0.5
Talc		1.2	$<10^{-4}$	16 ± 0.5
Phenolic spheres	25–100 μm	0.2	$<10^{-3}$	13 ± 1
Calcium silicate	0.02 μm	0.17	$<10^{-5}$	7.5 ± 0.5
(synthetic)	0.02–0.07 μm	0.36	$<10^{-5}$	5.5 ± 0.5
	0.02–0.07 μm	0.36	628 (N_2)	455 ± 5
Titanium dioxide	110 Å	0.35	$<10^{-3}$	16 ± 1
Iron oxide (Fe_2O_3)	200 Å	0.19	10^{-3}	14 ± 0.5

[b] Sample thickness, 2.54 cm; boundary temperatures, 304 and 76 K; wall emissivities greater than 0.8. The variations denoted by ± represent estimate of accuracy based on a combination of probable errors of measurement and the observed differences of the thermal conductivity of samples that were nominally the same.

[b] Mostly SiO_2 and Al_2O_3.

Source: Fulk (1959) and Kropschot (1959,1963).

Figure 5.3 : Mean thermal conductivity of various evacuated powders as observed apparent values [113].

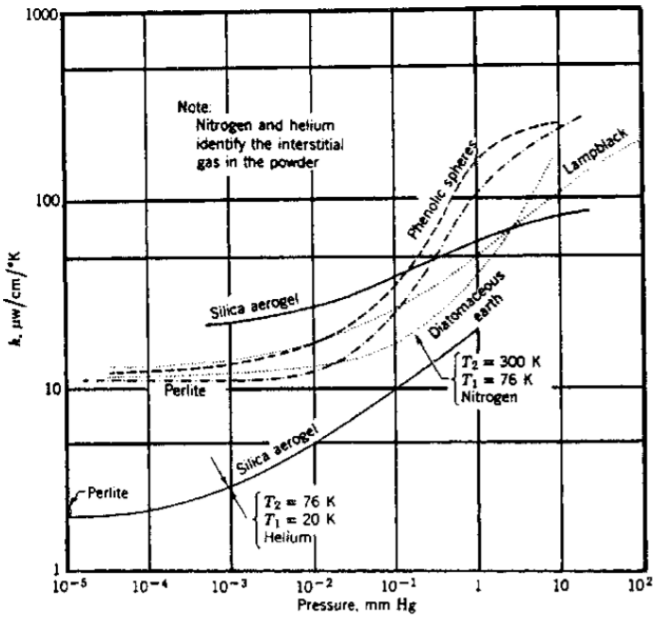

Figure 5.4 : Variations in the apparent mean thermal conductivities of multiple powders observed as a function of interstitial gas pressure [113].

5.1.1.1 Discussion

In reference [113] an example of internally insulated fiberglass wound cryogenic liquid hydrogen (LH2) tank has been explained. The tank has 457mm (18 in) diameter and 915mm (36 in) length and 6.9 bar (100psig) operation pressure. A combined plastic foam and wounded glass structure can be used for a light-weight cryogenic tank. 1/2 in.(12.5mm) thick foam layer is used as mandrel for the filament-winding.

The tank incorporates a vapor barrier on the inner side of the foam structure, enabling containment of both gaseous and liquid hydrogen. The foam layer is divided into upper and lower dome sections as well as a cylindrical midsection. Each of these segments is constructed using polyurethane foam enclosed in an aluminum–Mylar–aluminum (AMA) laminate, establishing a vacuum-tight barrier. A glass cloth is inserted between the foam and AMA laminate to facilitate a gas flow pathway during foam evacuation. The foam layer serves a dual purpose: acting as thermal insulation and functioning as a structural material that transmits internal pressure to the filament-wound shell structure.

Detailed construction details of the foam and vacuum-tight barrier in the region where the cylinder and dome sections join can be seen in Figure 5.5. The structural shell is constructed with two layers of longitudinal and four layers of circumferential wraps using glass filaments. The roving is created from 20-end S/HTS fiberglass impregnated with a low-temperature casing epoxy. For the tank liner, AMA laminate is utilized, and spin-formed domes are fashioned using a 0.005 in. (0.127 mm) thick laminate, while the cylinder section employs a 0.0025 in. (0.0635 mm) thick laminate. Ensuring a hermetic seal at -423˚F (-253˚C), the joints of the liner are sealed with adhesive after curing at a temperature compatible with the foam insulator. The vacuum-tightness of the enclosed foam is confirmed using a helium mass spectrometer, both before and after exposing the tank to cold shock with liquid nitrogen [113].

A heat loss of 1800 Btu/h (530 W); which corresponds to 50% liquid loss per hour was observed when %75 of the tank volume was filled about 1100 Btu (1160 kWh) amount of this loss cause from the conductive heat flow in the region of AMA laminate joint at the cylinder and bottom dome junction of the foam (Figure 5.5). Heat flux in the cylindrical region was about 80–110 Btu/(h ft2) [25.2–34.6 mW/cm^2] which reveals that the thermal conductiviy of foam is about 0.1 Btu in./(h ft2˚F) [0.144 mW/(cm˚C)].

At 68 psig (4.69 bar) pressure, liner failure was observed. The reason for liner failure is overstressing of the liner material [113].

The above mentioned tank uses inner thermal insulation but, the composite structure still experiences extreme cryogenic temperatures, and specially designed epoxy system was used for low temperatures.

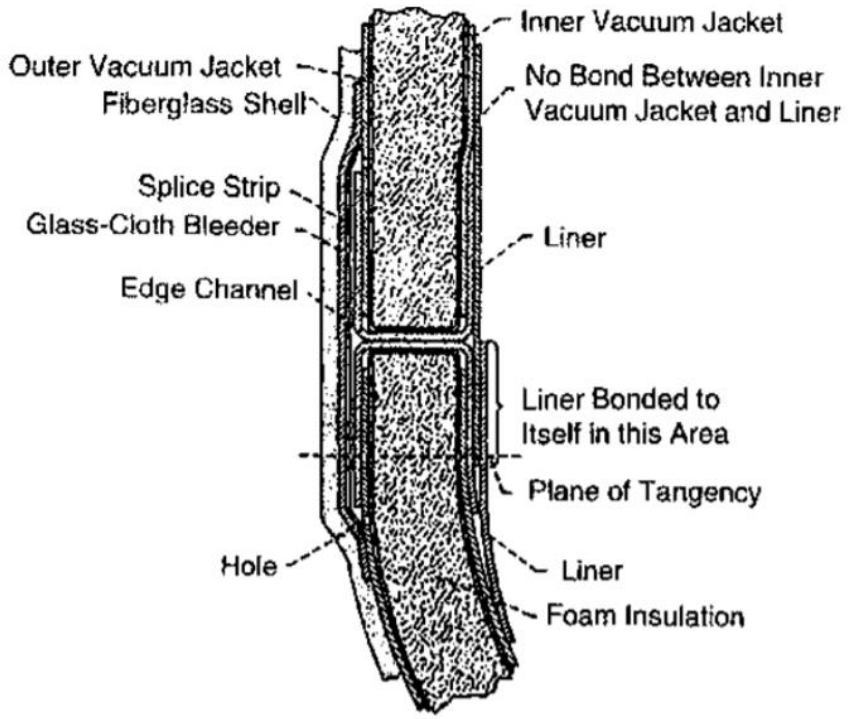

Figure 5.5 : Specifics regarding the joint between the cylindrical and dome sections of the tank's foam layer [113].

In a design with a liner, the optimum solution is to vacuum between the liner and the composite carrier to protect composite from cryogenic temperatures. However, when the thin membrane structure is pressurized after filling with liquid oxygen, this vacuum will be lost, so there will be no vacuum left to provide insulation throughout its wall thickness. To maintain this vacuum, carrier columns integrated into the inner membrane structure can be placed. However, there will be a high stress concentration at the membrane and column joints. If these column structures are placed much thinner cross sections but with close pitch, the needling effect (Hertzian contact) can be avoided. Also, the weight effect that the carrier columns will also be important (Figure 5.6). The production of this structure is another problem that needs to be solved.

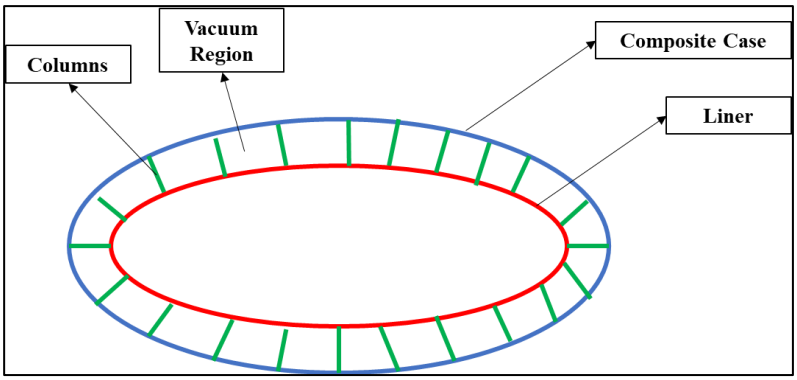

Figure 5.6 : Composite conceptual design.

Another critical issue in liner design is the potential self-damage of the liner membrane under thermal stress, which can result in issues like wrinkling and buckling. Minimizing thermal stress on the liner is crucial, and selecting a liner material with a thermal expansion coefficient (CTE) close to zero can help achieve this goal. The table below outlines the CTE, LOX compatibility, brittle/ductile transition behavior, and density of various materials. The materials are categorized based on their CTE value, LOX compatibility, ductility, and density (see Table 5.2).

Table 5.2 : Thermal expansion of materials low to high [114].

Product	CTE 10-6 m/m˚C	LOX Compability	Ductile/Brittle	Density (kg/m^3)
Carbon Fiber	-1 - +1	N/A		1790
Sitall	0.15	N/A	Brittle	2460
Quartz, fused	0.55	N/A	Brittle	2200
Diamond (Carbon)	1.1 - 1.3	N/A	Brittle	3510
Invar	1.5	YES	Ductile	8050
Wax	2 - 15	NO	Ductile	900
Silicon Carbide	2.77	N/A	Brittle	3210
Mica	3	N/A	Brittle	2880
Silicon	3 - 5	NO	Ductile	2330
Glass, Pyrex	4.0	N/A	Brittle	2230
Graphite, pure (Carbon)	4 -8	N/A	Brittle	2260
Tungsten	4.5	NO	Brittle	19280
Molybdenum	5	NO	Ductile	10200
Topas	5 - 8	N/A	Ductile	1020
Marble	5.5 - 14.1	N/A	Brittle	2800
Sapphire	5.3	N/A	Brittle	3890
Clay tile structure	5.9	NO	Brittle	1200
Hard alloy K20	6	N/A	Ductile	14600
Corundum, sintered	6.5	N/A	Brittle	3560
Titanium	8.5 - 9	NO	Ductile	4500
Steel	10.8 - 12.5	LIMIT	Brittle	8050
Epoxy	40-60	N/A	Ductile	1100

Invar36 metal liner weight and columns to protect vacuum will cause to lose all weight gains that are provided with composite material. For that reason pressure vessel with liner does not seem the effective solution for cryogenic conditions.

5.2 Type-II Cryogenic Tank Manufacturing and LN2 Testing

5.2.1 Analytical calculations

The debonding at the metal-composite interface was investigated through analytical calculations. An assumption for these calculations was made that the composite would not radially deform. While this assumption holds true for the fiber direction, it may not be accurate in the third direction.

The change in circumference and the corresponding change in radius,

From pressure (Equation 5.2):

$$\Delta r = \frac{p\ x\ r^2}{t\ x\ E(T)} \tag{5.2}$$

From thermal load (Equation 5.3):

$$\Delta r = r\ x\ \alpha(T) x\ \Delta T \tag{5.3}$$

Equating these two equations provides the pressure-temperature change relationship to maintain contact at the composite-metal interface.

Table 5.3 : Analytical calculation parameters.

Constants	Operational Variables	Material Variables as a function of temperature
Radius - r	Temperature change – ΔT	Young's Modulus – E(T)
Thickness - t	Pressure - P	Thermal expansion - α
Poissons's ratio - ν		

These analytical calculations reveal the required adhesive strength for maintaining interface contact. As depicted in the graphs below, when the vessel radius is equal to 300mm and subjected to a temperature change of −200˚C, the required pressure to protect contact is 40bar for a 2mm thickness (see Figure 5.7 and Figure 5.8).

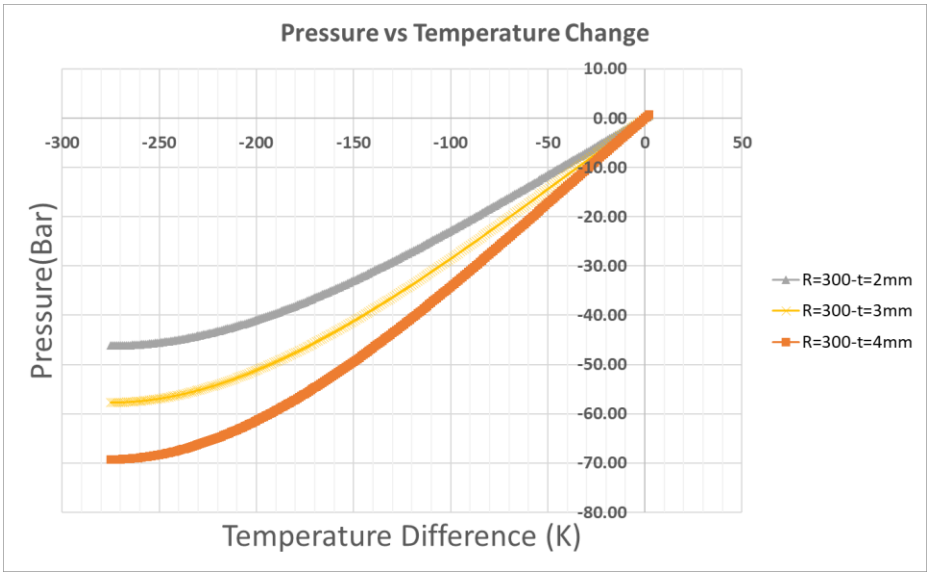

Figure 5.7 : TESOR rocket system Type-II pressure vs temperature diagram for different thickness values.

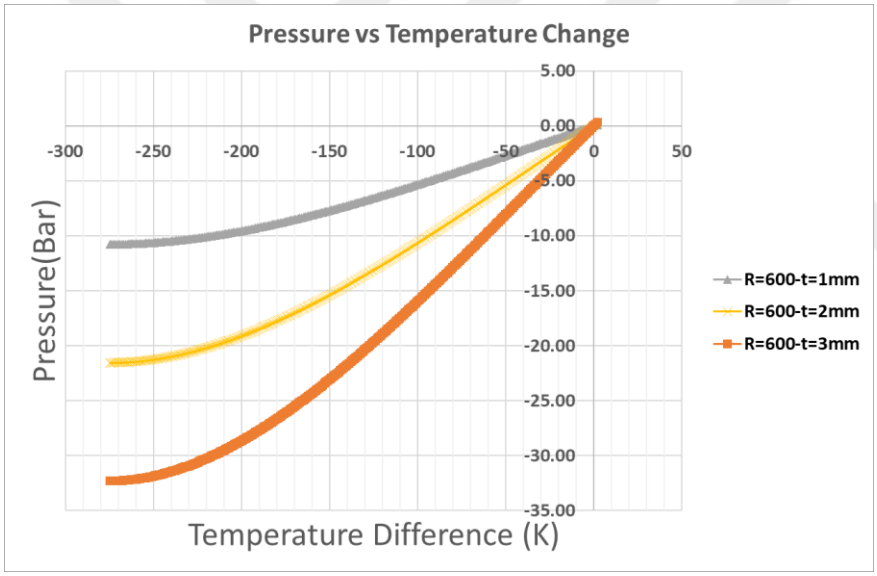

Figure 5.8 : SORS rocket system Type-II pressure vs temperature diagram for different thickness values.

5.2.2 Manufacturing

TESOR's LOX tank has been modified for test conditions. The diameter of the tank has been maintained as designed, while the length of the tank has been decreased to half of the original length. The tank now has a diameter of 300mm, length of 800mm, and a thickness of 7mm (see Figure 5.9).

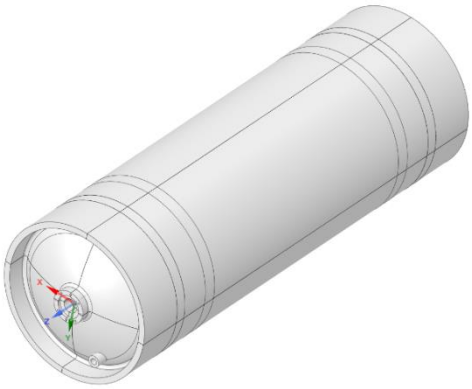

Figure 5.9 : Modified TESOR'S LOX Tank

The tank material is Aluminum 6061-T6, and the domes have been welded to the cylindrical region. The welding process leads to the loss of tempering, and as a result, the welded regions are designed thicker than the cylindrical wall region. The original tank has a 7mm wall thickness. This thickness value has been decreased to 2.5mm in the lathe, and it cannot be reduced below this value due to manufacturing constraints.

The composite layup is designed to be symmetric and as close as to quasi-isotropic structure. To obtain helical layers on metal structure, additional metal cylinders and domes have been used (Figure 5.10). The composite layup manufactured as [±49.6/90±/49.6/90/±49.6]. The carbon fibre material is Dow Aksa A49 and resin is CE-A 5025. Before winding process started, an adhesive has been applied to metal surface for obtaining higher interfacial strength between composite and metal structures.

Figure 5.10 : Type-II composite vessel filament winding and autoclave process

Figure 5.11 : Type-II composite pressure vessel

After manufacturing extra parts were removed with lathe and Type-II vessel was obtained (Figure 5.11). Details of the manufactured tank can be seen in Table 5.4.

Table 5.4 : Type-II tank weight properties

	Base Metal Tank 7.0mm	Base Metal Tank 2.5mm	With Composite
Weight(kg)	19.1	9.3	11.9

5.2.3 Thermal cycle test

A thermal cycle test was conducted to assess the performance of the manufactured Type-II tank. Prior to the thermal cycle test, non-destructive testing (NDT) methods were employed to identify manufacturing-related large-scale defects in the composite laminate.

Figure 5.12 : NDT check for detecting manufacturing based cracks

The thermal cycle setup is constructed with manuel fill and relief valves. Thermal cycle test is done via LN2 filling. Figure 5.13 and 5.14 shows the thermal cycle test.

Figure 5.13 : Type-II tank LN2 thermal cycle test

- The test is conducted in two cycles. Three thermocouples(TC) and three strain gauges(SG) mounted.
- There was an interruption in the strain and temperature data due to a computer problem. As a result, the data has been presented in two separate graphs.

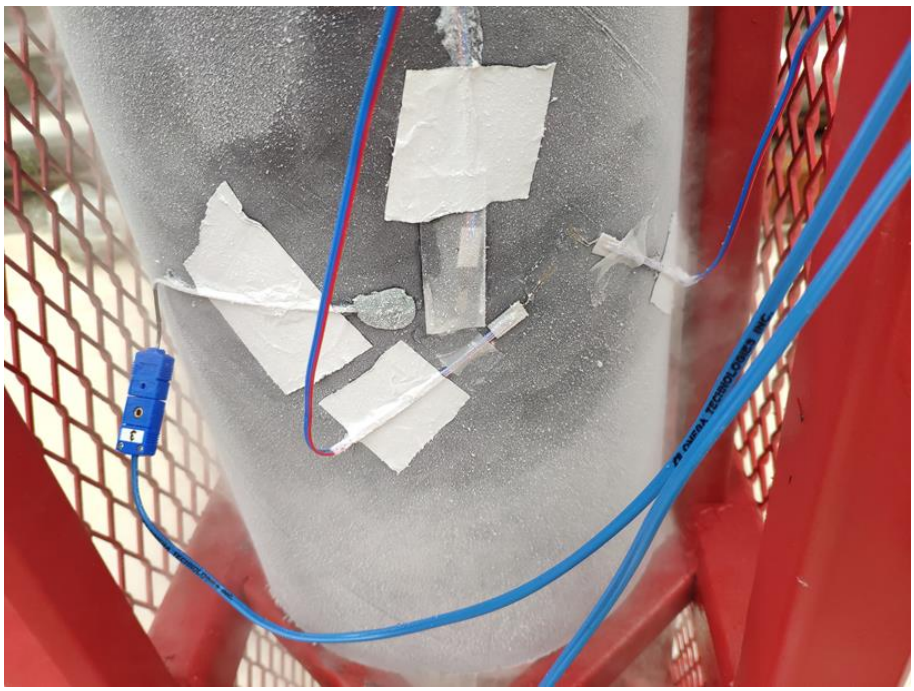

Figure 5.14 : Strain gagues on thermal cycle test

- Strain gauge 3 is free, 1 is bonded to the composite face in the transverse fiber direction, and 2 is bonded in the fiber direction.
- In the first cycle, the tank was not fully filled. TC1 (up) shows a value of 100K, while the bottom shows 77-80K. Figure 5.15 (left) illustrates the first cycle of LN2 filling and dumping.
- From Figure 5.15 (left), it can be observed that the TC on the composite lost contact from the composite. The temperature decreases to 172K but then starts to increase sharply, indicating a loss of contact from the composite face. After this point, the temperature data is not accurate for the composite face.
- The second filling cycle started without waiting for the system to come to room temperature. Figure 5.15 (right) shows the TC values. Even though the tank is filled completely, the composite TC shows 190K because of TC debonding from the composite face.
- There were sounds like explosions during LN2 filling, probably indicating debonding of the composite and metal interface. NDT inspection was performed again after the thermal cycle test, and no cracks were observed. However, the resolution of these observations may not be enough to check for composite cracks (Figure 5.17). The composite-metal interface bonding was preserved after the test, but there were likely local debonding damages.
- The values on strain gauges returned to initial values after the thermal cycle. Only the free gauge has a little residual strain (Figure 5.16).
- Strain gague values before test:
    - SG1(Matrix)= -1078 με; SG2(Fiber)=156 με; SG3(Free)= -660με
- Strain gague values after test:
    - SG1(Matrix)=-1030 με; SG2(Fiber)=164 με; SG3(Free)=-500με
- It is understood that the thermal cycle loading did not cause any macro damage to the composite, or the strain gauge data may not have enough resolution to capture microcracks.

- The temperature data was gathered via three thermocouples (TC). TC2 is located on the bottom filling region, TC1 is located on the upside vent region, and TC3 is located on the composite region.

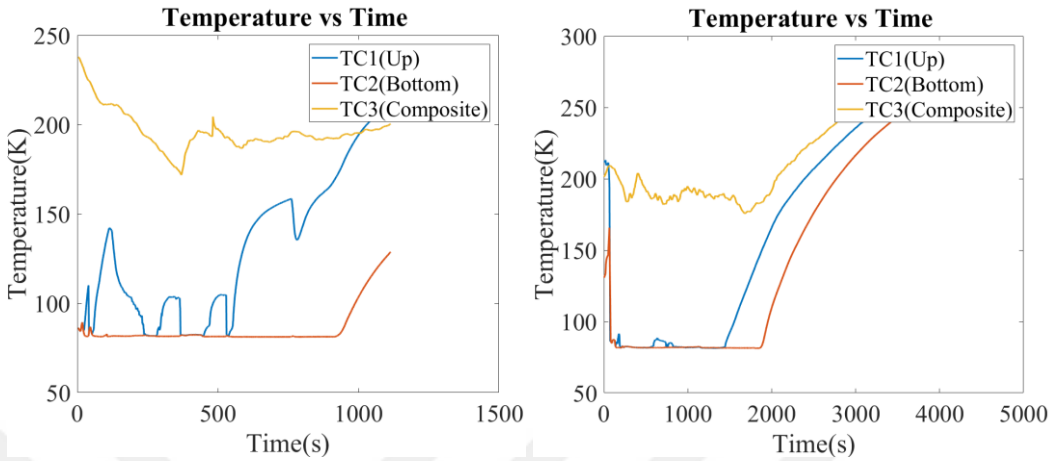

Figure 5.15 : TC values during thermal test

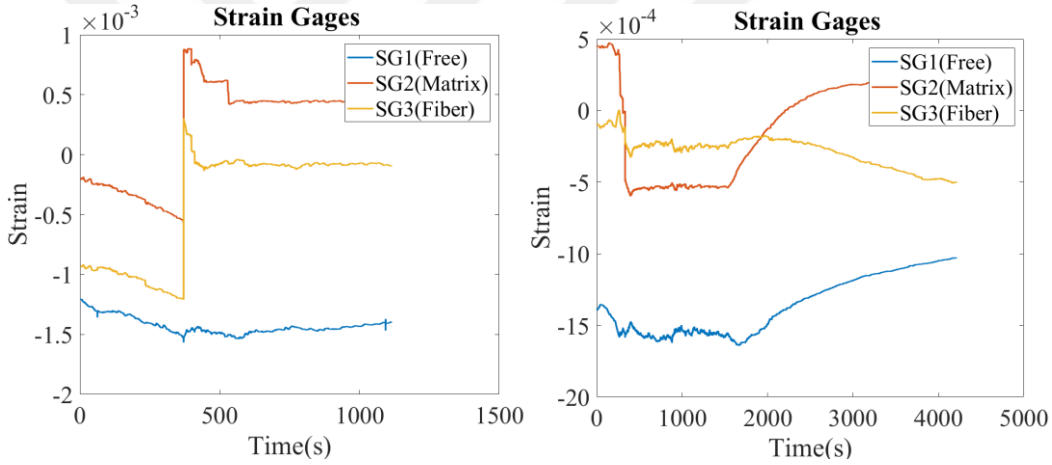

Figure 5.16 : Strain gauge values during thermal test

The high deviation of TC1(Up) occurs because of LN2 splashing during filling process.

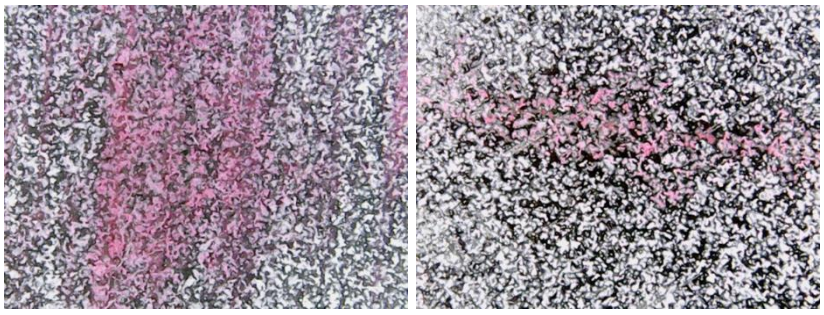

Figure 5.17 : The NDT inspection via microscope

6. TYPE-V LINERLESS TANK INVESTIGATION

Type-V (linerless) cryogenic vessels hold crucial importance in terms of weight efficiency for space applications. Continuous advancements in composite materials enable the manufacturing of these vessels using composite materials. In linerless composite vessels, the composite shell must not only provide structural strength to the vessel but also serve as a barrier against liquid and gas permeation under pressure and various environmental conditions. However, the impact of cryogenic temperatures on composite materials is substantial due to significant differences in the coefficients of thermal expansion between the fiber and epoxy constituents [22,103,109]. Kang [115] categorizes vessel types based on their structure and compares them in terms of cost, weight, and safety. Type-V tanks offer up to 60% weight savings without compromising reliability (Figure 6.1).

The production of liners for Type-III and Type-IV tanks is not cost-effective for small quantities. Therefore, the decision has been made to manufacture a linerless Type-V tank. Linerless tanks offer greater weight savings for space applications [116].

Gen.	Type Ⅰ	Type Ⅱ	Type Ⅲ	Type Ⅳ	Type Ⅴ
Liner	Steel	Steel/glass fiber	Aluminum	Polymer	Glass/ carbon fiber composite [Linerless]
Outer layer			Glass/ carbon fiber composite	Glass/ carbon fiber composite	
Diagram	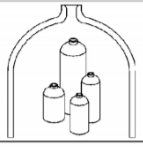	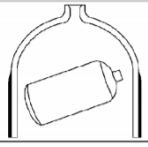		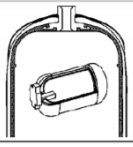	
Cost	-	-	239%	100%	80~90%
Weight	100%	80%	60%	45%	36~40%
Safety	Low	Low	Normal	High	High
Feature	Weight↑, internal corrosion problem		Need to prevent galvanic corrosion	Lightweight, Excellent stability/durability	Ultra lightweight, Excellent stability/durability
Note	N/A		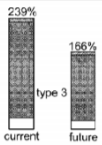	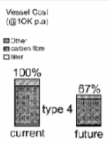	-

Figure 6.1 : Tank types comparison [115].

The development of a linerless cryogenic composite tank requires examination from modeling, experimental, and manufacturing perspectives. Numerous studies in the

literature have focused on manufacturing, constituent testing, or modeling individually. One of the most comprehensive works on linerless composite pressure vessels has been conducted by Mallick et al. [4]. Their study encompasses material development, an analytical micromechanical approach, tank design, and finite element analysis.

In terms of manufacturing, studies have explored inflatable [115], dissolvable [117], and collapsible [118] mandrel types applicable to Type-V tank manufacturing. Modeling studies have adopted a multi-scaled mechanical approach, with a focus on constitutive relations. Constituents such as fibers, epoxy, and fiber-epoxy interactions have been investigated using micro- and meso-scale calculations through analytical and finite element methods [100,103,105,107,109].

This section details the preliminary studies for the low-cost development of a cryogenic Type-V tank. The study encompasses the manufacturing method, hydro and liquid nitrogen tests for the linerless tank, and micro-scale structural calculations. In the initial phase, the Type-V tank was manufactured using a liquefiable paraffin-based mandrel and the wet filament winding technique. The tank features a hybrid composite structure with glass and carbon layers, where the glass layers were incorporated to achieve a non-permeable layer. A structural-grade epoxy system was chosen for manufacturing. Subsequently, the manufactured tank underwent hydrotesting to identify any major leakage issues. Following hydrotesting, the tank was subjected to cryogenic conditions through liquid nitrogen (LN2) filling. The LN2-tested tank underwent another hydrotest to assess the damage caused by the cryogenic temperature. The design was further evaluated using micro- and macro-level finite element analysis. Representative volume elements were employed to combine micro and macro stress-strain levels, allowing for an investigation into micro-crack initiation. All these phases constitute the preliminary steps of the cryogenic Type-V development methodology, focusing on mechanical aspects.

6.1 Manufacturing Plan

To manufacture a linerless tank extractable, collapsible, breakable, dissolvable mandrel can be used. Also inflatable bladder mandrel is another option to produce linerless tank.

To manufacture a linerless tank, various types of mandrels can be employed, such as extractable, collapsible, breakable, or dissolvable mandrels. One option is to use a dissolvable mandrel, such as wax or paraffin. However, using wax as a mandrel introduces LOX compatibility concerns, as the wax and resin may mix in certain regions during the wet winding process. To mitigate this, the wax mandrel should be covered with Teflon or another LOX-compatible material after molding to keep the wax and resin separate during manufacturing. Another main disadavantge of wax mandrel is, it can not be used with developed Cyanate ester or any other high temperature curing thermoset. Cyanate ester requires 80˚C mandrel surface for filament winding, wax could not keep it's structural integrity at these temperatures.

An alternative dissolvable mandrel material is XPS, which can be machined to form the mandrel. Polyvinyl Alcohol (PVA) is also suggested in the literature as a dissolvable mandrel material, as it can be dissolved with water (Figure 6.2). The selection criteria for a mandrel should include easy manufacturability, rigidity at room and high temperatures, reusability, and the capability for an easy extraction process.

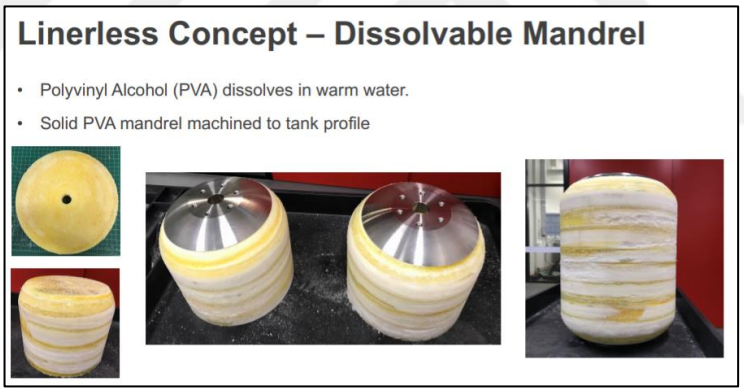

Figure 6.2 : Dissolvable mandrel with PVA material [116].

A US Patent [115] from Composite Technology Development company describes a blow-type mandrel for the production of linerless composite tanks. This technology was developed in collaboration with the U.S. Air Force Research Laboratory and the University of Texas for use in the FASTRAC 1 satellite. The blow-type tank has a diameter of 152mm, length of 203mm, volume of 1.9L, and weighs 0.2kg. The proof pressure is set at 690 bar, with a burst pressure ranging from 1,300 to 1,700 bar. The patented manufacturing technology, Multiple Use Precision Extractable Tooling (MUPET), utilizes toughened epoxy by KIBOKO and T700 carbon fiber by Toray [115].

The method involves using supporting shape memory foam, which maintains its shape and rigidity at room temperature during filament winding and the pressurizing stage at thermal curing. After curing is complete, the process continues with vacuuming and cooling to shrink the shape memory foam. This allows the foam to be removed from the tank and reused. Figure 6.3 provides a brief overview of this procedure. However, it's important to note that this manufacturing technology requires high-tech material manufacturing capabilities and process expertise.

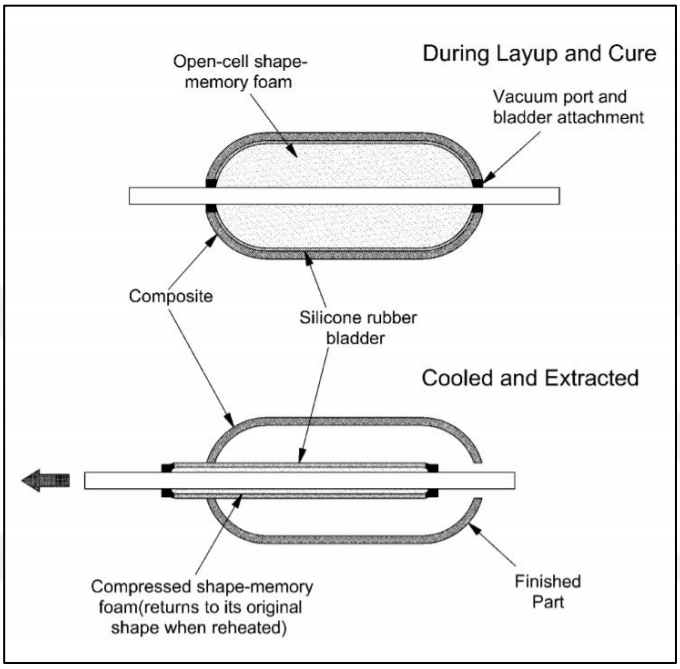

Figure 6.3 : Shape memory foam mandrel [115].

6.2 Type-V Linerless Tank Manufacturing

The Type-V production methods have been investigated using three different approaches to produce a soluble liner.

• 3D printed mandrel with PVA and ABS material

• PVA powder and paste preparation

• Parafin based mandrel

6.2.1 3D printed mandrel

Raise-3D Pro-plus2 3D printer has been utilized for the production of a plastic mandrel. Initially, PVA filament was chosen due to its water solubility. However, challenges were encountered as 3D printed PVA lacked the necessary rigidity for

mandrel applications. Consequently, ABS material was adopted, and its solubility in acetone facilitated the printing process. The dimensions of the mandrel were determined based on the limitations imposed by the 3D printer's size (Figure 6.4).

Figure 6.4 : 3D printer.

The designed mandrel features a geometry with a 100mm diameter, a cylindrical length of 100mm, and spherical dome structures. As the intention is to remove the mandrel after filament winding, a minimum thickness of 1.5mm was selected, balancing the need for rigidity. Figure 6.5 provides a visual representation of the designed filament winding mandrel for Type-V tank manufacturing. In Figure 6.6, the 3D printed mandrel and the filament winding process are showcased.

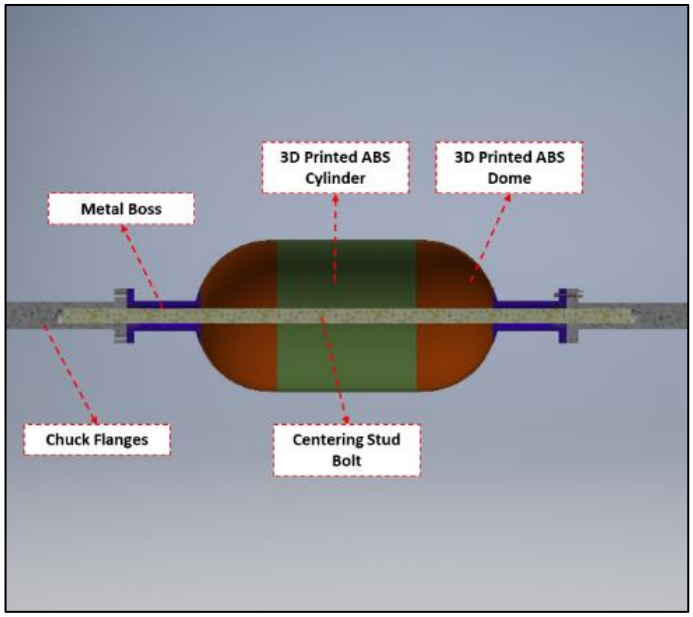

Figure 6.5 : 3D printed mandrel design for filament winding.

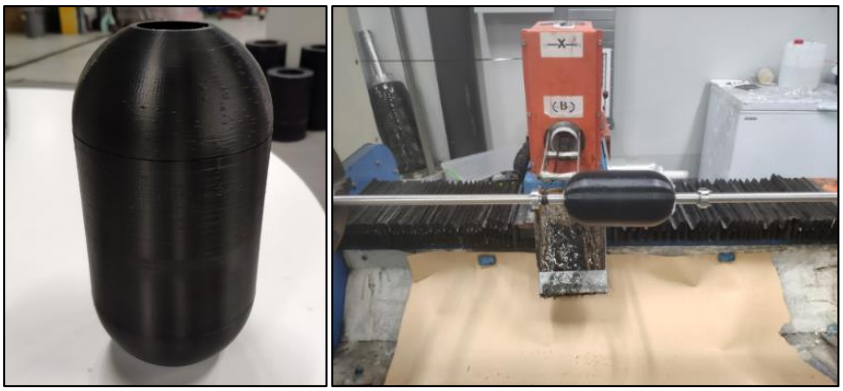

Figure 6.6 : 3D printed mandrel and machine assembly

The Hunstman 1564-3474 resin system was used for filament winding the curing cycle is 80°C for 1 hour and 120°C for 4 hours (Figure 6.7).

Figure 6.7 : 3D printed mandrel filament winding and oven curing.

It was observed that the polar bosses did not bond well to the composite and could be rotated freely by hand. This lack of adhesion was attributed to the very low bonding face area. The curved regions of the polar bosses needed to be larger. To test the solubility of the ABS material, the composite tank was filled with acetone up to half its volume and rotated on a lathe for 3 days. After draining the acetone from the tank, it was observed that the viscosity of the drained ABS-acetone mix had increased. Figure 6.8 illustrates the pasty acetone-ABS mix.

To assess whether the mandrel was completely removed, the composite tank was cut in half. Figure 6.9 reveals that the mandrel was not removed thoroughly. While this method offers a faster process for mandrel production with a 3D printer, limitations in sizing and challenges in mandrel removal led to the decision to disregard this method.

Figure 6.8 : Drain of acetone and composite tank cutting.

Figure 6.9 : Half cut section of the winded vessel.

6.2.2 PVA powder based mandrel

The PVA powder was mixed with water using a high-shear machine to obtain a paste material. The solution was allowed to evaporate water, and after a week, the solution had become pasty. However, it was observed that this material did not meet the rigidity requirement for the mandrel (Figure 6.10).

Figure 6.10 : PVA powder and processed pasty PVA.

Also, when the PVA powder is heated up to its melting temperature, the material is carbonized before melting, making this process not applicable. However, with a paraffin-based mandrel, PVA pasty material can be used to cover the wax and protect

the wax containment during wet epoxy application. As noted before, wax containment is an issue for LOX compatibility.

6.2.3 Paraffin based mandrel

A stainless steel dome with a standard 265mm inner diameter and 4mm thickness was manufactured by bending (Figure 6.11). The boss material is Aluminum 6061-T6.

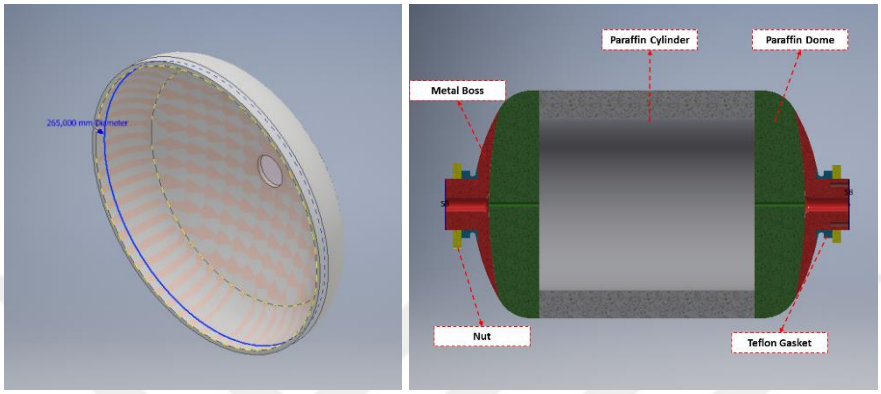

Figure 6.11 : Paraffin Mandrel and Boss design.

A paraffin formulation has been established for the required melting point and rigidity behavior of the paraffin. This formulation was prepared in a melting pot using a high shear mixer with additional particle materials (Figure 6.12). The paraffin is melted around 70°C. The dome mold is also heated up to 70°C before casting. If paraffin is applied to a cold mold, paraffin would show up with many cracks during solidification. After casting, the paraffin is left to solidify for up to 1 day at room temperature. Figure 6.13 and 6.14 show the solidification phase.

The solidified paraffin was separated from the dome with a hydraulic press. It has been observed that the paraffin was bonded very well both to the dome mold and the metal polar boss.

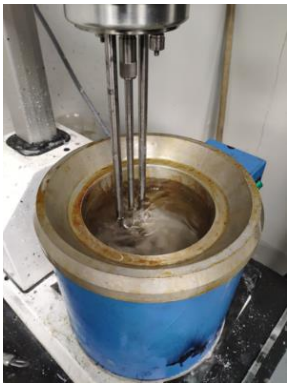

Figure 6.12 : Paraffin formulation preparation with melting pot and high shear.

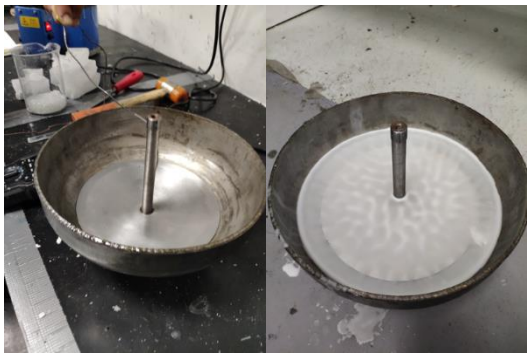

Figure 6.13 : Dome mold and liquid paraffin solidification

Figure 6.14 : Solid paraffin in mold and released paraffin dome with metal boss.

The casted domes are tooled in lathe and geometric refinement was done (Figure 6.15).

Figure 6.15 : Dimensionally refined paraffin domes.

Standard modulus carbon fiber, E-glass fiber, and a structural-grade epoxy system were used for manufacturing. The filament winding process was completed via a 4-axis filament winding machine.

The composite layup is designed with 2 glass layers (±17.9˚, ±22.4˚), 1 carbon hoop layer (±89.8˚), and 2 helical (±11.5˚) carbon layers as a hybrid structure. These angles were chosen to fully cover the paraffin mandrel and provide non-slippage on fibers during the winding process. The glass layers are aimed to provide a non-permeable layer (Figure 6.16).

Figure 6.16 : Filament winding on paraffin mandrel and autoclave curing

6.2.3.1 Materials and micro finite element analyses

The thermomechanical properties of the constituents have been given in Table 6.1 and Table 6.2 [109,119]. The carbon fiber is IM7, the glass fiber is E-Glass, and the resin material is 977-3. These material properties have been taken from the literature and may include differences with the materials that were utilized in manufacturing.

Table 6.1 : Thermo-mechanical properties of carbon fiber and E-Glass fiber.

Material	E1 (GPa)	E2=E3 (GPa)	G12=G13 (GPa)	G23 (GPa)	μ23	μ12=μ13	α11 (K^{-1})	α22=α33 (K^{-1})	X_T (MPa)	X_C (MPa)
Carbon Fiber	263	19	27.6	6.9	0.35	0.2	-0.9 e-6	7.2 e-6	5180	3200
E-Glass Fiber	74	74	30.8	30.8	0.22	0.22	4.9 e-6	4.9 e-6	2150	1450

Table 6.2 : Thermo-mechanical properties of resin

Property	@ 295K	@ 77K
E (GPa)	3.36	4.77
α (K^{-1})	56.57e-6	18.67e-6
Poisson's Ratio	0.35	0.35
Tensile Strength (MPa)	90	130

Six unit mechanical and one unit temperature loadings were performed for a hexagonal RVE with a volume fraction ratio of 0.45, and micro stress distributions were obtained. These analyses have been done for glass and carbon fiber material systems with resin thermomechanical properties at 295K and 77K (Figure 6.17 and Figure 6.18). If the

macro-analysis environmental load includes thermal loading, the RVE model with cryogenic material properties has been used. Otherwise, the RVE with room temperature material properties has been used. The micro-model contains 944 solid elements for the matrix region and 1,136 solid elements for the fibers. Also, orthotropic material properties that were used in macro-analysis were evaluated with these RVE elements (Table 6.3).

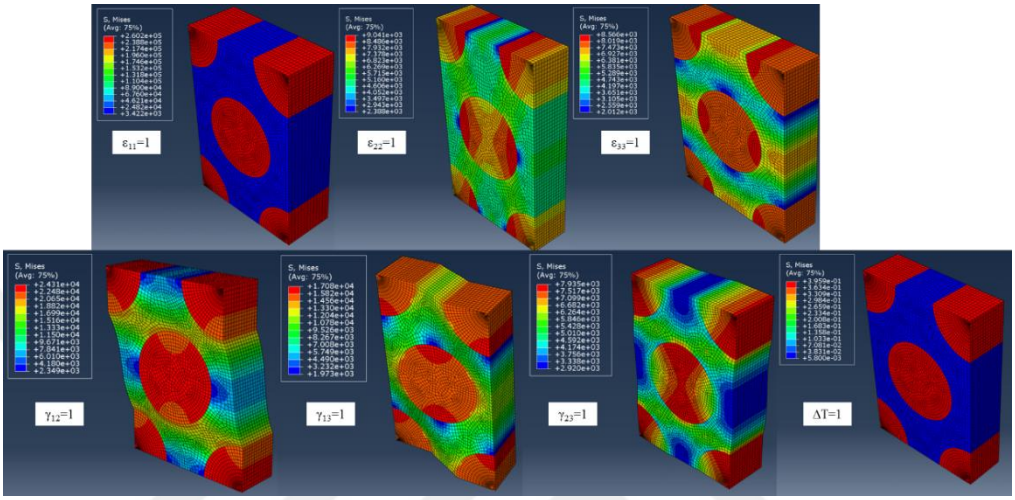

Figure 6.17 : Von Mises stress distribution of IM7/977-3 RVE with 77K properties for unit loadings.

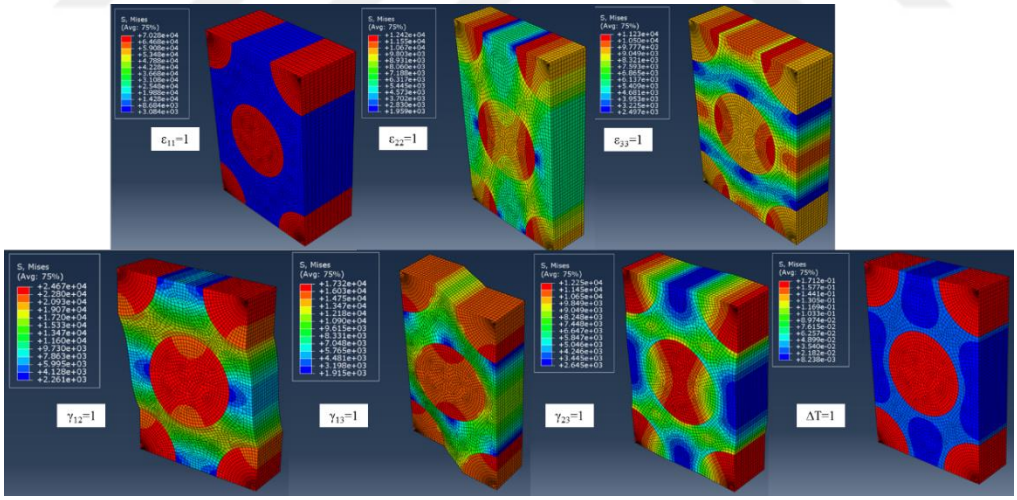

Figure 6.18 : Von Mises stress distribution of E-Glass/977-3 RVE with 77K properties for unit loadings.

6.2.3.2 Macro finite element analyses

ANSYS Workbench has been used for composite tank structural analysis. Composite layup is defined in the ACP-Pre module with filament wound layup angle and thickness data gathered via CADFIL software (Figure 6.19). A total of 108,734

elements as SOLID186 (Layered) for composite layers and SOLID186 for polar bosses were employed.

The cryogenic load is applied as liquid nitrogen temperature (77K) from room temperature (295K). The boundary conditions were defined as fixed support at one end and axially free at the other end.

The tank has been subjected to three different loading conditions separately:

- Case 1: Hydrotest / Only +30 bar pressure
- Case 2: Cryogenic Filling/ LN2 thermal load and +5 bar pressure load
- Case 3: Only LN2 thermal load (295K to 77K)

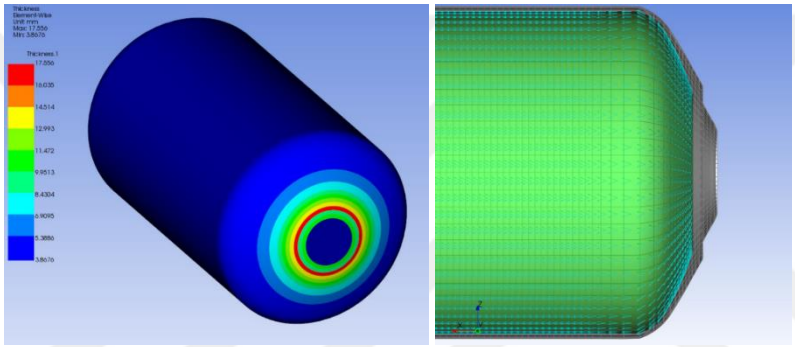

Figure 6.19 : Composite thickness distribution and fiber angle representation.

Table 6.3 : Thermo-mechanical properties of carbon and glass layers

Material	IM7/ 977-3		E-Glass/ 977-3	
Property	At 295K	At 77K	At 295K	At 77K
E1 (GPa)	159.15	159.72	45.76	46.33
E2 (Gpa)	8.56	10.56	11.87	15.83
E3 (Gpa)	8.56	10.56	11.87	15.83
G12 (Gpa)	4.29	5.74	4.35	5.84
G23 (Gpa)	2.96	3.65	4.27	5.72
G31 (Gpa)	4.29	5.74	4.35	5.84
nu12	0.254	0.255	0.265	0.265
nu13	0.254	0.255	0.265	0.265
nu23	0.438	0.437	0.401	0.392
α_x (10-6/K)	-0.349	-0.642	6.622	5.544
α_y (10-6/K)	31.874	13.827	28.392	11.164
α_z (10-6/K)	31.866	13.825	28.392	11.165

6.2.3.3 Results of case 1: hydrotest and micro scale analysis

The hydrotest results indicate that the linerless composite tank successfully withstood pressurization without experiencing damage or leakage. The test involved a gradual increase in pressure levels, as shown in Figure 6.20b, with three cycles of pressure

loading and unloading. According to the measurements, the manufactured tank demonstrated the ability to maintain the input pressure for designated hold durations without exhibiting micro-cracking (Table 6.4). Upon completion of the test, a manual inspection of the outer surface revealed no signs of damage or leakage.

Table 6.4 : Hydrotest pressure values.

Input Pressure(bar)	Hold Duration(min)	Internal Pressure(bar)
30.2	1	27.1
29.5	1	26.2
30.3	2	25.7
30.3	4	25.7

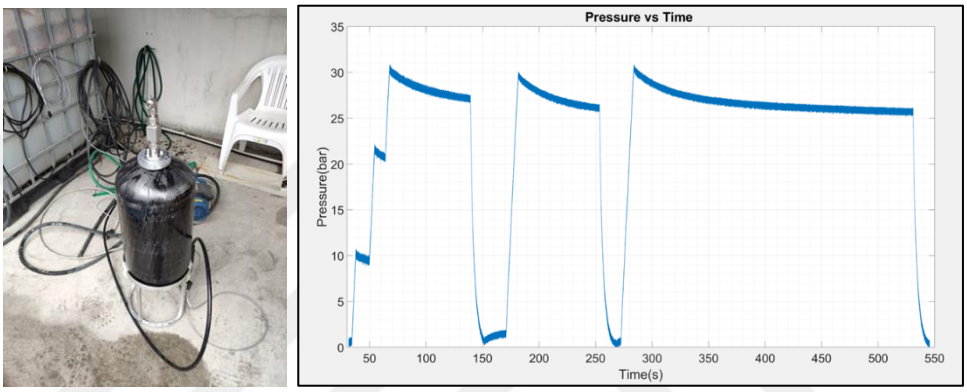

Figure 6.20 : (a) Hydrotesting of the linerless tank, (b) Pressure-Time data during hydrotest.

The strain gauges were strategically placed, as outlined in Table 6.5. However, it is noteworthy that certain strain gauges did not respond during the gas and LN2 tests. To reflect this observation, a "Serviceability" column has been included in Table 6.5 to denote the responsiveness of each strain gauge during the testing procedures.

Table 6.5 : Applied Strain Gauges Details.

Strain Gauge Number	Location	Direction	Servicability for Gas Test	Serviceability for LN2 Test
1	Dome-Cylinder Transition	Fiber	Work	X
2	Middle of Cylinder	Matrix	Work	Work
3	Middle of Cylinder	Fiber	Work	Work
4	Middle of Cylinder	Matrix	X	X
5	Dome-Cylinder Transition	Fiber	X	X
6	Dome-Cylinder Transition	Matrix	Work	X

Table 6.6 : Strain Gauge responses during gas leakage test.

Strain Gauge Number	Position	Initial Value	Value @30 bar (Initial Value Extracted)	Macro FEA	Difference(%)
1	Transition Fiber	-353	-1195	-1390	%16.3
2	Middle Matrix	-353	+2961	+2900	%2.1
3	Middle Fiber	-1393	+465	+575	%23.6
4	Middle Matrix	----------	----------	----------	
5	Transition Matrix	----------	----------	----------	
6	Transition Fiber	-778	-233	-265	%13.7

The FEA analysis revealed rapid changes in strain values on the dome transition areas. Within a 5mm width region, the strain values fluctuated from 80με to −1480 με in the fiber direction. Consequently, strain values in these regions should be measured using strain gauges with a smaller grid length to capture finer details. It's important to note that these abrupt changes were also influenced by manufacturing errors, particularly the sharp and discontinuous nature of the transition region between the dome and cylinder. Ensuring the continuity of this transition region is crucial for a gradual stress transition.

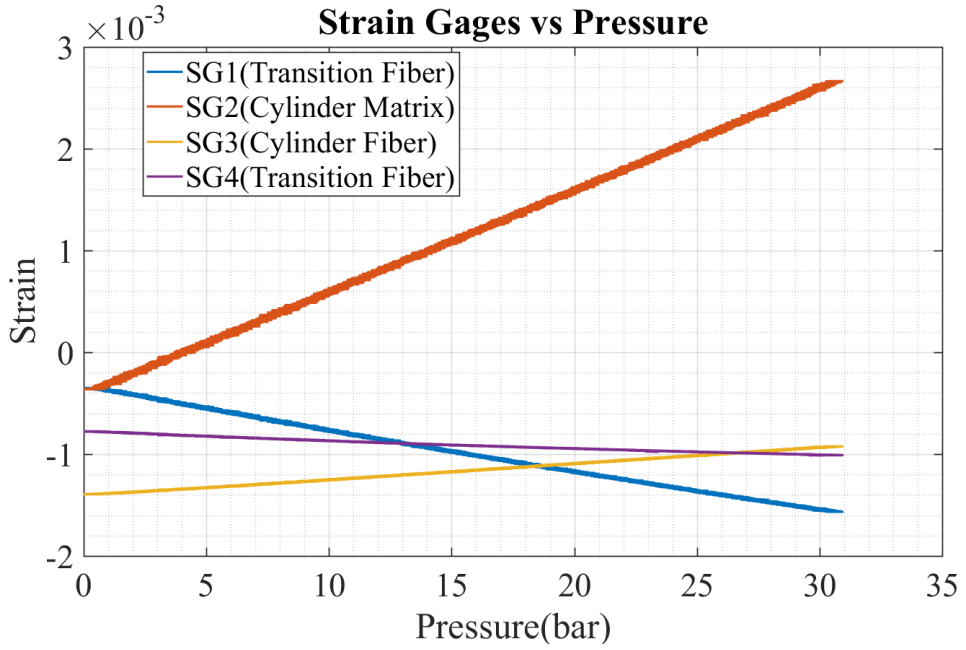

Figure 6.21 : Type-V tank nitrous leakage test strain gauge responses.

Figure 6.21 illustrates the strain gauge responses during the nitrous gas leakage test. None of the gauges exhibit any sudden behavior, indicating that there is no macro damage or interface debonding during the gas leakage test.

Additionally, the hydrotest case was evaluated using a trans-scale analysis on the cylindrical region (Table 6.7). The table demonstrates that none of the fiber materials exceed their tensile/compression strength values. Moreover, the Von Mises stress values of the matrix constituent remain below the matrix tensile strength at room temperature (90MPa). The trans-scale analysis confirms the absence of micro-damage.

Table 6.7 : Trans-scale results of case 1: hydrotest.

Loading Condition	Layer	Macro	Fiber - Micro		Macro	Matrix- Micro			Micro Crack
		$\sigma_{Fiber\ Direction}$ (MPa)	σ_{Max} (MPa)	σ_{Min} (MPa)	$\sigma_{Transverse\ Direction}$ (MPa)	σ_{Max} (MPa)	σ_{Min} (MPa)	σ_{Mises} (MPa)	σ_{Mises}
Only +30 bar pressure	Glass (±17.9˚)	45.3	184.2	97.7	35.5	140.4	104.1	33.3	No
	Glass (±22.4˚)	50.6	189.6	97.8	34.5	140.4	104.0	33.4	No
	Carbon (±89˚)	491.3	803.2	78.4	10.5	119.5	87.3	26.6	No
	Carbon (±11.5˚)	117.1	180.7	81.2	26.3	119.6	87.0	26.5	No
	Carbon (±11.5˚)	186.4	183.1	81.6	26.1	119.5	87.3	26.1	No

6.2.3.4 Results of case 2: cryogenic filling and micro scale analysis

The cryogenic test of the Type-V pressure vessel was conducted via LN2 filling (Figure 6.22a, 6.22b). During the filling process, a debonding event was captured at the metal/composite interface on the polar boss region. This failure was expected due to the high coefficient of thermal expansion (CTE) difference between the aluminum polar boss and composite shell. As shown in Figure 6.23, the pressure value increased to 10 bar at the beginning of the filling process. Subsequently, ventilation was opened, leading to a gradual decrease in pressure (average 5 bar during the test). Upon noticing LN2 leakage, the filling process was halted, ventilation fully opened, and the test was stopped.

Efforts were made to compare strain gauge values for gas and LN2 tests at similar pressure levels. However, due to the loss of contact at the polar boss-composite interface at the end of the LN2 filling process, LN2 started leaking from that region, prompting the cessation of the filling process. No pressurization was applied for the LN2 test. This type of failure was expected due to the high CTE difference between the aluminum polar boss and the composite.

Figure 6.23 illustrates the pressure and temperature (TC) values versus time graph. As observed in the graph, the pressure value increased to 10 bar at the start of the filling process, followed by the opening of ventilation and a subsequent decrease in pressure. The filling process was halted and ventilation fully opened after LN2 leakage was detected, as seen at time 900s.

Figure 6.22 : (a) Cryogenic testing setup, (b) Cryogenic Filling.

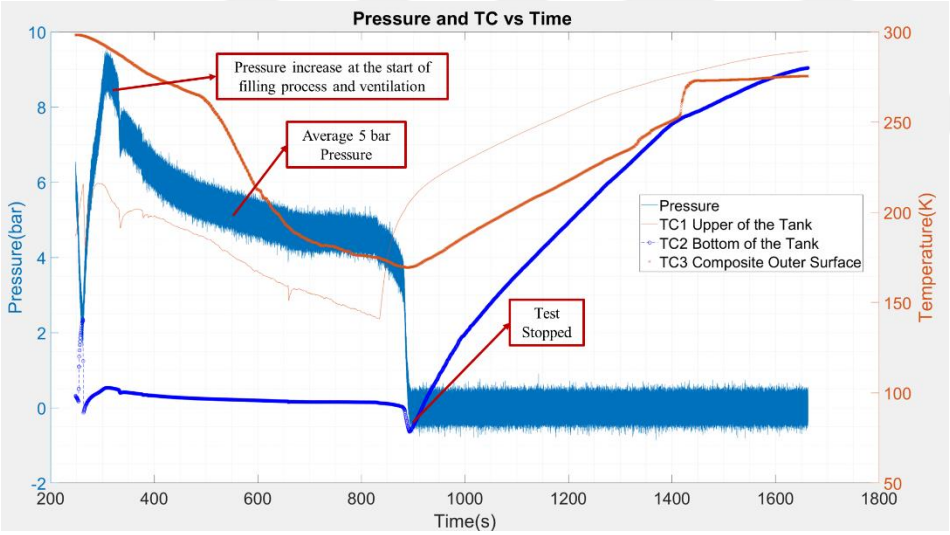

Figure 6.23 : Pressure and temperature values versus time.

Figure 6.24 displays the strain gauge responses during LN2 filling. As expected, strain values become negative in the cylinder region due to contraction. The matrix-oriented strain gauge exhibited a sudden increase in its value at time 650s, coinciding with the onset of LN2 leakage. The temperature (TC) value on the composite surface indicates a temperature of 195K at time 650s.

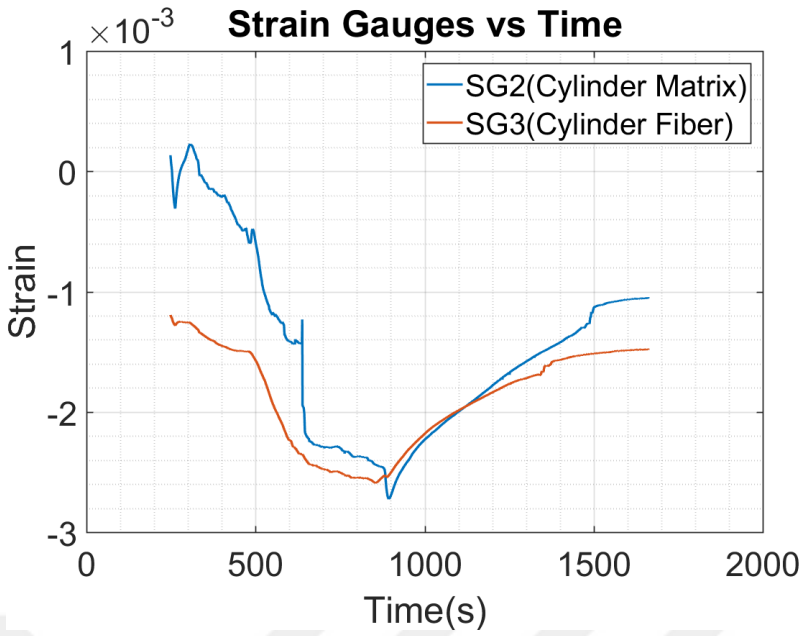

Figure 6.24 : Strain Gauge values versus Time.

The strain gauge thermal compensation is not completed; therefore, a meaningful comparison of the room temperature and LN2 test values is not possible. However, some comments have been added below. Table 6.8 provides the SG2 and SG3 values for gas and cryogenic tests. A pressure value of 4.5bar is taken as a comparison for two gauges, with the minimum temperature on the composite data obtained as 141K (−132°C).

Table 6.8 : Strain Gauge reponses during cryogenic LN2 test.

Strain Gauge Number	Position	Value @4.5 bar RT test	Value @4.5 bar LN2 test-141K
2	Middle Matrix	+396	-2028
3	Middle Fiber	+58	-1161

From the nitrous gas test (Table 6.8), it can be observed that a 1 bar pressure load causes around 99με strain on SG2 (Matrix direction) and 15.5με on SG3 (Fiber direction) (Nonlinearity effects ignored). Comparing these values with Table 6.6 shows that the cryogenic temperature change (22°C-(-132°C)) caused an additional strain (negative) equal to around 21bar and 71bar pressure load for the matrix gauge and fiber gauge, respectively, at room temperature. The equivalent pressure value for the matrix gauge is meaningful, but for the fiber gauge, it is very high. It is believed that the fiber is going into local buckling mode because of different temperatures inside and outside of the tank. The FEA analysis also shows this buckling behavior.

Table 6.9 : Trans-scale results of case 2 cryogenic filling.

Loading Condition	Layer	Macro	Fiber - Micro		Macro	Matrix- Micro			Micro Crack
		$\sigma_{Fiber\ Direction}$ (MPa)	σ_{Max} (MPa)	σ_{Min} (MPa)	$\sigma_{Transverse\ Direction}$ (MPa)	σ_{Max} (MPa)	σ_{Min} (MPa)	σ_{Mises} (MPa)	σ_{Max}
LN2 Thermal load and +5bar pressure load	Glass (±17.9˚)	58.1	280.6	125.5	37.2	163.4	123.8	35.1	Yes
	Glass (±22.4˚)	57.2	277.9	125.6	37.1	163.1	123.8	35.0	Yes
	Carbon (±89˚)	-92.9	130.2	-206.5	28.8	131.2	102.7	25.7	On Limit
	Carbon (±11.5˚)	-41.5	123.3	-120.5	26	129.3	102.8	22.7	On Limit
	Carbon (±11.5˚)	-42.5	126.9	-121.4	25.7	129.2	102.9	22.6	On Limit

The trans-scale analysis details of the cryogenic filling case on the cylindrical region have been provided in Table 6.9. The fiber stress values and matrix Von Mises stress values are below strength limits, and damage is not expected according to the Von Mises criteria. However, the resin material loses its ductility under cryogenic conditions and becomes brittle. This situation requires changing the failure criteria to maximum stress criteria for the matrix, which will provide much more accurate results. The matrix maximum stress values are higher than the tensile strength of the resin material on the glass layers and close to the tensile strength of the resin material on the carbon layers. This indicates micro failure in the matrix.

6.2.3.5 Results of case 3: only LN2 thermal load (295K to 77K) and micro scale analysis

The trans-scale analysis has also been conducted for the case of only LN2 thermal load on the cylindrical region to understand the thermal load effect clearly (Table 6.10)..

Table 6.10 : Trans-scale results of only LN2 thermal load (295K to 77K).

Loading Condition	Layer	Macro	Fiber - Micro		Macro	Matrix- Micro			Micro Crack
		$\sigma_{Fiber\ Direction}$ (MPa)	σ_{Max} (MPa)	σ_{Min} (MPa)	$\sigma_{Transverse\ Direction}$ (MPa)	σ_{Max} (MPa)	σ_{Min} (MPa)	σ_{Mises} (MPa)	σ_{Max}
Only LN2 thermal load (295K to 77K)	Glass (±17.9˚)	50.1	269.4	126.1	29.9	158.0	122.5	31.1	Yes
	Glass (±22.4˚)	48.6	266.8	126.3	30.1	158.1	122.5	31.2	Yes
	Carbon (±89˚)	-166.9	128.6	-327.5	26.6	128.8	101.1	25.6	On Limit
	Carbon (±11.5˚)	-60.8	85.8	-187.1	21.2	90.4	46.1	38.6	No
	Carbon (±11.5˚)	-62.3	86.7	-187.3	20.9	90.7	47.0	38.2	No

The previously mentioned ductile-brittle transition is again valid for this case, indicating failure on glass and carbon hoop layers with only LN2 thermal load (Table 6.10). Additionally, the comparison of the values between Table 6.7 and Table 6.10 shows that the stress values caused by the LN2 thermal load are close to the ones from the 30 bar pressure load on the glass and carbon hoop layers. However, they are higher by around 50 percent on the helical carbon layer.

6.2.3.6 Hydrotest after liquid nitrogen (LN2) test

The LN2-tested tank was hydrotested to observe the effect of cryogenic thermal load on composite damage and permeability. During the hydrotests, the composite layup sweated water under a 4-5 bar pressure load (Figure 6.25). The thermal load from LN2 resulted in microcrack accumulation, causing a decrease in thickness and leading to the loss of non-permeability in the composite layup.

The trans-scale analysis with the maximum stress criterion on the matrix accurately anticipated this damage in the composite shell under LN2 thermal load. However, the Von Mises criterion was found to have false premises for thermal load cases concerning matrix crack initiation.

Figure 6.25 : Leakage of composite after LN2 test.

In conclusion, this study on the development of a low-cost cryogenic Type-V tank holds significant practical implications for the space industry, seeking efficient and

affordable cryogenic storage solutions. The use of a liquefiable paraffin mandrel and wet filament winding technique has shown promising results in the manufacturing process, offering a pathway for cost-effective tank production.

The hydrotest conducted in the initial phase confirmed the integrity of the tank design, as no major leakage was observed. Complementing this, trans-scale finite element analysis provided further validation. However, during the cryogenic LN2 filling, the presence of a high thermal expansion difference between the composite case and the aluminum polar boss led to interface debonding at the halfway point. The LN2-tested tank was hydrotested again to assess damage to the permeability of the composite case. The composite case sweated at 4-6 bar pressure values from all surfaces. The high temperature difference caused significant damage to the composite case, resulting in microcracks formed and accumulated through thickness. The trans-scale analysis cannot capture this failure according to Von Mises stress criteria. Therefore, it is required to use the maximum stress criterion under cryogenic conditions due to the ductile-brittle transition of the resin material.

The study acknowledges limitations, such as the calculation method determining only the first crack failure, suggesting the need for an improved method with progressive damage analysis on a micro-scale level. The stress-based damage method could benefit from enhancements, including energy-based damage criteria, and interface strength evaluation. Additionally, investigating the thermal gradient through thickness during cryogenic liquid filling is essential, considering the interaction of the inner side with LN2 and the outer surface with air, which causes a thermal gradient through thickness, emphasizing the need to determine crack evolution through thickness.

In summary, this study offers informative details about manufacturing, testing, and analyzing methods for developing a low-cost cryogenic Type-V tank.

6.3 Large Scale Type-V (Linerless) Pressure Vessel Production

Up to now, a total of 32 600mm hybrid rocket motor cases have been manufactured and hydrotested. The composite case is comprised of both glass and carbon layers, with the glass layers serving as a non-permeable barrier and the carbon layers providing structural strength. However, some motor cases have experienced water leakage during hydrotesting.

The issues leading to leakage can be attributed to the epoxy curing cycle. This has been substantiated through Differential Scanning Calorimetry (DSC) analysis conducted on both liquid and production-cured epoxy specimens.

Another factor contributing to leakages is related to the fiber-epoxy interfacial bonding, particularly with the glass fibers and resin. The silane coating on glass fibers facilitates the bonding of fibers with epoxy. Any damage to this coating, whether through moisture exposure or oxidation in the presence of air, significantly reduces the bonding performance. As a consequence, leakages have been observed in some motor cases.

Addressing these issues with the epoxy curing cycle and ensuring the integrity of fiber-epoxy bonding, especially for glass fibers, will be crucial for preventing leakages and enhancing the overall reliability of the hybrid rocket motor cases.

6.3.1 Design and analysis

Structural analysis of the Type-V pressure vessel system was conducted using ANSYS Mechanical software. The Type-V pressure vessel is constructed with a combination of glass fiber and carbon fiber plies, as illustrated in Figure 6.26.

In the initial stage, material data were specified within the software, and the pre-existing geometry model was imported into ANSYS. Geometric configurations for the structural analysis were set up using the SpaceClaim module integrated into ANSYS. The ACP module was employed for modeling composites, as depicted in Figure 6.27. This comprehensive approach allowed for a detailed structural analysis of the Type-V pressure vessel system.

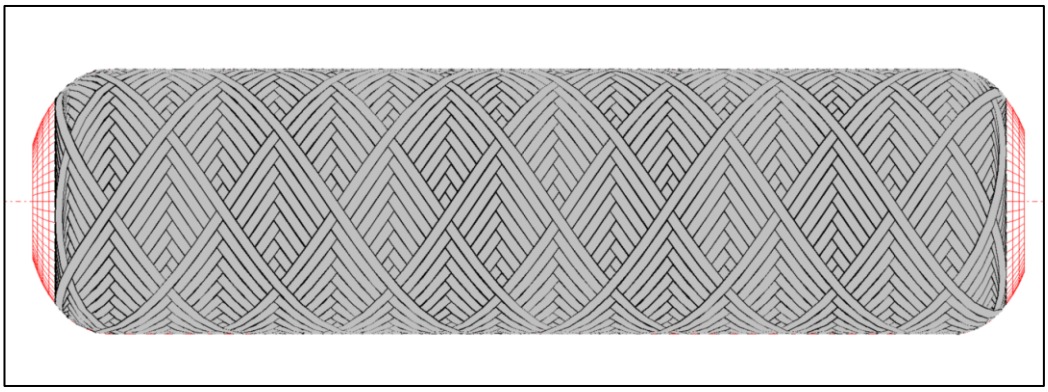

Figure 6.26 : NC view of Winding Type-V pressure vessel

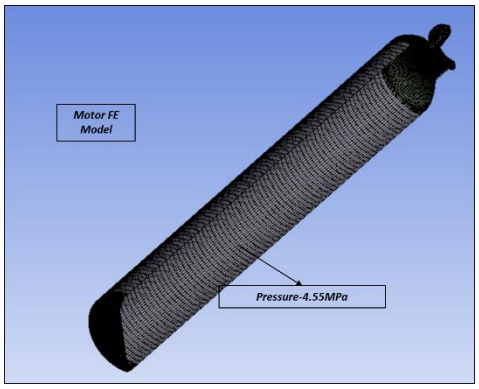

Figure 6.27 : FE model of Type-V pressure vessel.

The solution network of the model comprises 98,413 elements and 180,445 nodes. The composite body is represented using shell elements, and the model incorporates elastic material properties, nonlinear contact, and nonlinear geometry options. For the purpose of this analysis, the bolt connections are simplified and defined as a bonded contact, as the primary focus is on assessing the condition of the composite body.

The analysis does not predict any damage based on the finite element analysis results. Figure 6.28 displays the total deformation of the composite case under operating pressure. Additionally, the Tsai-Wu damage index of the outermost carbon composite layer is shown. It's worth noting that trans-scale analyses were not conducted on these motor cases.

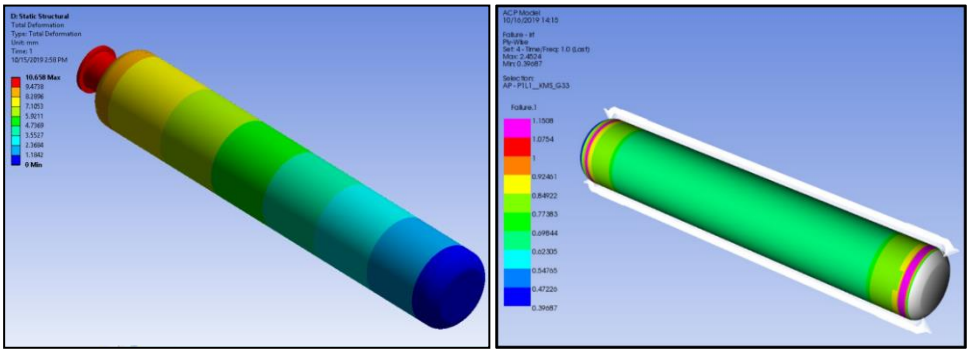

Figure 6.28 : Total deformation(left) and outer carbon layer Tsai-Wu failure index.

6.3.2 Manufacturing

The manufacturing process for the Type-V pressure vessel involves the use of a 4-axis filament winding machine, and the NC code for this process is prepared using CADFIL software. The glass winding of the Type-V pressure vessel is depicted in Figure 6.29, while Figure 6.30 shows the carbon winding.

Figure 6.29 : Glass Layer Winding.

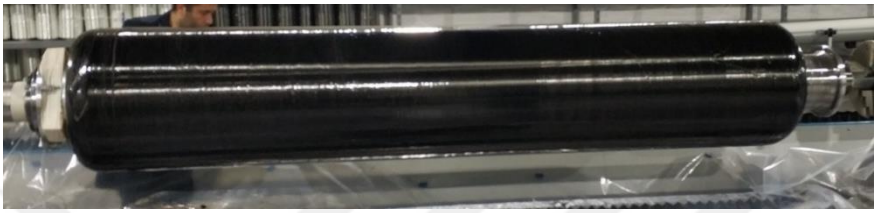

Figure 6.30 : Carbon Layer Winding.

6.3.3 Hydrotest

Hydrotesting was conducted to validate the reliability of the pressure vessel. Pressure values during the hydrotest were monitored using the NI system, which involved a pressure sensor connected to the water pump manifold connection part with a T structure. The test setup for the hydrotest can be observed in Figure 6.31. Additionally, camera records were taken during the test to inspect any areas of leakage. This thorough testing process helps ensure the integrity of the pressure vessel under operational conditions.

Figure 6.31 : Hydrotest system of Type-V pressure vessel.

The strain gauge data collected from the hydrotest has been compared and correlated with the FEA results. This correlation process involves validating the simulation predictions against the real-world measurements obtained during the hydrotest. It helps ensure that the FEA model accurately represents the structural behavior of the pressure vessel under the applied load conditions. The strain gauge data serves as experimental validation for the FEA predictions, enhancing the confidence in the simulation results and the overall structural analysis.

7. CONCLUSIONS

This study aims to develop a composite cryogenic LOX tank by addressing critical aspects such as selecting the right epoxy system, analyzing the delamination behavior of CFRP laminates, conducting microscale stress analysis, investigating Type-II tanks, and assessing the practical implications of a low-cost cryogenic Type-V tank. The study provides comprehensive details on the development phases of low-cost composite cryogenic tanks, paving the way for future developments, particularly for medium-scale sounding rockets. One of the most significant aspects of this thesis is that it's the first study conducted in Turkey on the development of cryogenic composite tanks. The study will serve as a reference for Turkey's National Space Programme in the development of such tanks.

Cryogenic composite technology requires the use of advanced material systems, but managing the supply chain and cost is a major challenge. To address this issue, a thesis was conducted to evaluate low-cost epoxy systems that are readily available. The selection and evaluation process focused on manufacturability, compatibility with LOX, and mechanical performance in both room temperature and cryogenic conditions. After rigorous testing, the Huntsman 1564-3474 epoxy system was identified as the optimal choice due to its potential mechanical properties, such as its strain capability under cryogenic conditions, and LOX compatibility, which is crucial for the fabrication of LOX pressure vessels. However, further testing using ENF specimens and Type-V tank revealed that considering only the behavior of the epoxy system is not enough to evaluate the cryogenic behavior of composites..

The study of filament-wound CFRP laminates' mode-II delamination behavior has revealed a complex interplay between resin types, manufacturing techniques, and performance under cryogenic temperatures. It was observed that vacuum infusion and toughened resin systems demonstrated stable G_{IIc} values, while the cold curing resin system, despite its excellent performance at room temperature, suffered significant reductions in G_{IIc} values under cryogenic conditions. These findings highlight the

importance of accounting for material interactions and manufacturing-related issues to ensure effective performance in cryogenic environments.

The microscale stress analysis focused on different epoxy systems' responses to cryogenic temperatures and highlighted the significance of selecting materials with compatible thermal expansion coefficients and modulus changes. Epotek 301-2 and 301-2FL emerged as the preferred choice when considering Von Mises stress, emphasizing the critical role of modulus and thermal expansion coefficient changes. Meanwhile, T7110 stood out for minimizing maximum stress on the matrix, emphasizing low thermal expansion, and maintaining matrix-fiber interaction.

Parametrization of the material properties led to understanding the property effect on microscale stress levels. When thermal load plays the most significant role, the analysis shows that the matrix's thermal expansion coefficient (CTE) and its temperature-dependent variation are crucial for cryogenic thermal loads. A lower CTE value of the matrix helps to minimize matrix stress levels. Furthermore, a smaller relative difference between the matrix CTE and the transverse CTE of the fiber also contributes to reducing matrix stress levels. As anticipated, decreased matrix rigidity leads to lower matrix stress levels. These calculation-based studies led to an in-house micromechanical calculation tool, which provides foresight to understand actual stress values on the microscale. Parametrization offers easy and fast determination of the required material properties under cryogenic conditions.

Moreover, the investigation highlighted the constraints associated with Type-II tank systems, revealing their inadequacy for cryogenic applications. Under cryogenic conditions, metal and composite shells experienced high debonding forces because of high thermal expansion differences.

Exploring a low-cost cryogenic Type-V tank introduced innovative manufacturing techniques actively studied worldwide, such as using a liquefiable paraffin mandrel and wet filament winding. These manufacturing efforts resulted in a successful prototype Type-V pressure vessel capable of withstanding pressure levels of up to 30 bars without any leakage. However, cryogenic testing of this tank revealed the crucial effects of cryogenic temperatures on composite laminates. The developed micromechanical calculation tool helped identify the cryogenic temperature effect by detecting microcracking using the maximum stress criterion for the matrix constituent.

This multidisciplinary study has made significant contributions to the field of composite cryogenic LOX tanks and has also laid out a roadmap for future research and development. By integrating material selection, manufacturing techniques, and performance analysis, this study provides a solid foundation for advancing efficient and cost-effective cryogenic storage solutions in the field of space exploration. In conclusion, this study offers valuable insights and recommendations for the development of improved cryogenic storage solutions in the future.

7.1 Recommendations and Future Work

Figure 7.1 illustrates the overall problem evaluation. While this thesis attempted to address each subtask, limitations arose due to the scope of the proposed work.

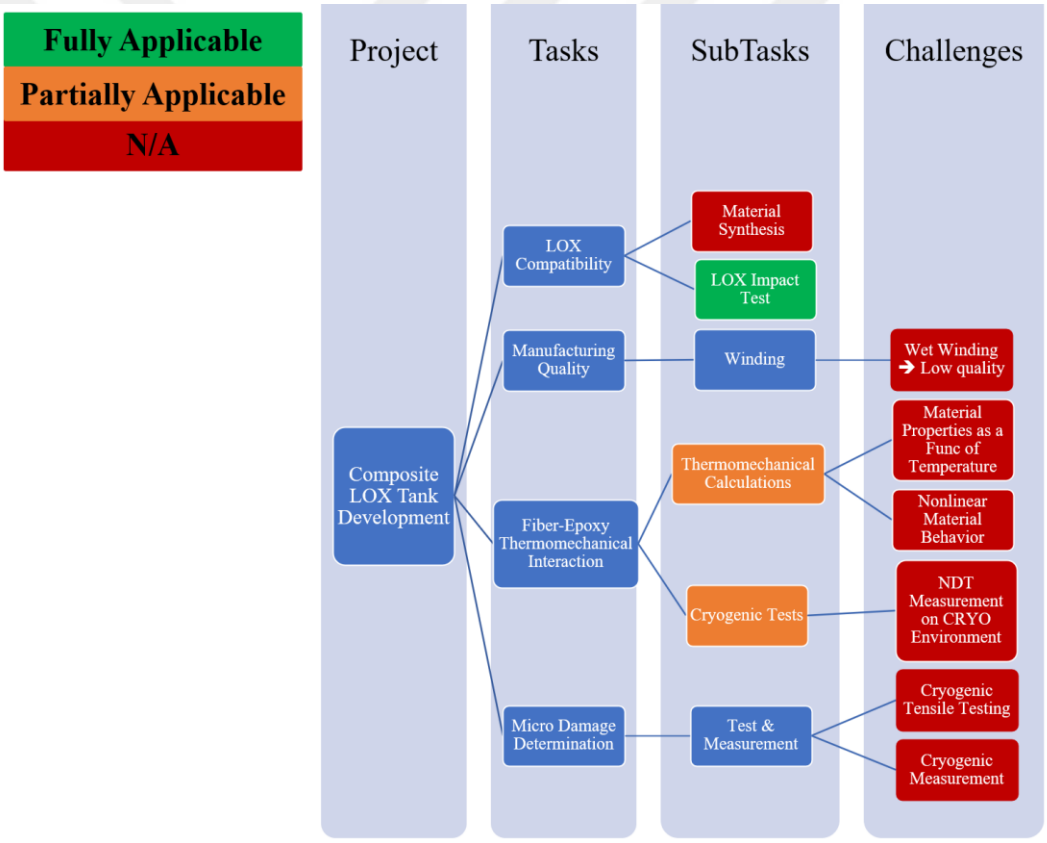

Figure 7.1 : General evaluation of the study

This work could be further expanded with below suggestions:

- The constituent base and interaction tests should be expanded under cryogenic environments.

- The constituent thermal and mechanical properties should be determined as a function of temperature.
- Manufacturing is currently done with the wet filament winding technique, which introduces many uncertainties for composite materials. The manufacturing of such space systems is generally accomplished with prepreg and automated fiber placement systems.
- NDT measurement techniques could be researched and developed under cryogenic environments to determine microcrack evolution on composite laminates. The determination of the fiber/matrix interaction under cryogenic conditions is crucial to develop composite cryogenic pressure vessels.
- This thesis does not focus on the effects of thermal cycling loads as rocket propellant tanks generally do not require thermal cycling. However, cryogenic thermal cycle tests could pave the way for the development of composite LH2 storage tanks, which could also be used in the automotive industry where hydrogen is considered as an alternative future fuel technology.

REFERENCES

[1] **Y. He, L. Zhang, G. Chen, X. Li, D. Yao, J.H. Lee, Y. Zhang.** (2014). Surface functionalized carbon nanotubes and its effects on the mechanical properties of epoxy based composites at cryogenic temperature, *Polymer Bulletin*, ***71***. https://doi.org/10.1007/s00289-014-1202-6.

[2] **K. Mallick, J. Cronin, S. Arzberger, M.L. Tupper, L. Grimes-Ledesma, J.C. Lewis, C. Paul, J.S. Welsh.** (2004). Ultralight linerless composite tanks for in-space applications, *A Collection Technical Papers - AIAA Space 2004 Conference Exposition*, 1 , 1–13. https://doi.org/10.2514/6.2004-5801.

[3] **N. Liu, B. Ma, F. Liu, W. Huang, B. Xu, L. Qu, Y. Yang.** (2021). Progress in research on composite cryogenic propellant tank for large aerospace vehicles, *Composites Part A Applied Science and Manufacturing*, ***143***. https://doi.org/10.1016/j.compositesa.2021.106297.

[4] **K. Mallick, J. Cronin, K. Ryan, S. Arzberger, N. Munshi, C. Paul, J.S. Welsh.** (2005). An integrated systematic approach to linerless composite tank development, in: *Collection Technical Papers - 46th AIAA/ASME/ASCE/AHS/ASC Structures, Structural Dynamics, and Materials Conference*, Austin, Texas, pp. 3553–3569. https://doi.org/10.2514/6.2005-2089.

[5] **M.A. Karabeyoglu, Nitrous oxide and oxygen mixtures (Nytrox) as oxidizers for rocket propulsion applications.** (2014). *Journal of Propulsion and* Power., ***30*** 696–706. https://doi.org/10.2514/1.B34768.

[6] **M. Sippel, A. Kopp, D. Mattsson Swerea SICOMP, S. Jonas Freund.** (2015). Final Results of Advanced Cryo-Tanks Research Project CHATT, *The European Conference for Aeronautics and Space Sciences*.

[7] **M. Sippel, A. Kopp.** (2016) Progress on Advanced Cryo-Tanks Structural Design Achieved in CHATT-Project, *14th European Conference on Spacecraft Structures, Materials and Environmental Testing*.

[8] **M. Sippel, A. Kopp, D. Mattsson.** (2013), Advanced Cryo-Tanks Research in CHATT, *5th European Conference for Aerospace Sciences*.

[9] **M. Sippel, A. Kopp, D. Mattsson, S. Koussios**. (2014). Advanced Cryo-Tanks Structural Design Investigated in CHATT, *13th European Conference on Spacecraft Structures, Materials and Environmental Testing*. 727.

[10] **M.J. Robinson**, (1994). Composite cryogenic propellant tank development, in: *Collection Technical Papers - 46th AIAA/ASME/ASCE/AHS/ASC Structures, Structural Dynamics, and Materials Conference*, https://doi.org/10.2514/6.1994-1375.

[11] **W. Zhou, Z. Wu, L. Mevel** (2010). Vibration-based damage detection to the composite tank filled with fluid, *Structural Health Monitoring*, **9**. https://doi.org/10.1177/1475921710361329.

[12] **J. Ju, B.D. Pickle, R.J. Morgan, J.N. Reddy**. (2007). An initial and progressive failure analysis for cryogenic composite fuel tank design, *Journal of Composite Materials*, **41**, 2545–2568. https://doi.org/10.1177/0021998307076492.

[13] **H. Zheng, X. Zeng, J. Zhang, H. Sun.** (2018). The Application of Carbon Fiber Composites in Cryotank, in: *Solidification*, https://doi.org/10.5772/intechopen.73127.

[14] **I.G. Tapeinos, D.S. Zarouchas, O.K. Bergsma, S. Koussios, R. Benedictus.** (2019). Evaluation of the mechanical performance of a composite multi-cell tank for cryogenic storage: Part I - Tank pressure window based on progressive failure analysis, *International Journal of Hydrogen Energy*, ***44***, 3917–3930. https://doi.org/10.1016/j.ijhydene.2018.12.118.

[15] **I.G. Tapeinos, A. Rajabzadeh, D.S. Zarouchas, M. Stief, R.M. Groves, S. Koussios, R. Benedictus.** (2019). Evaluation of the mechanical performance of a composite multi-cell tank for cryogenic storage: Part II – Experimental assessment, *International Journal of Hydrogen Energy*, ***44***, 3931–3943. https://doi.org/10.1016/j.ijhydene.2018.12.063.

[16] **M.J. Robinson.** (1996). Composite structures on the DC-XA reusable launch vehicle, in: *International SAMPE Technical Conference*.

[17] **D.C. Freeman, T.A. Talay, R.E. Austin.** (1997). Reusable launch vehicle technology program, *Acta Astronautica*, ***41***. https://doi.org/10.1016/S0094-5765(97)00197-5.

[18] **E.H. Stokes.** (2002). Hydrogen Permeability of a Polymer Based Composite Tank Material Under Tetra-Axial Strain, *5th Conference on Aerospace Materials, Processes, and Environmental Technology*.

[19] **J.H. Vickers.** (2013). Composite Australia Conference Composite Cryotank Project Structures for Launch Vehicles, *Composite Australia Conference*, 54.

[20] **Url-1** <*https://www.compositesworld.com/articles/developing-a-linerless-all-composite-spherical-cryotank*>, date retrieved 15.04.2022.

[21] **D.M. Grogan, C.M. Ó Brádaigh, J.P. McGarry, S.B. Leen.** (2015). Damage and permeability in tape-laid thermoplastic composite cryogenic tanks, *Composites Part A Applied Science and Manufacturing*, ***78***, 390–402. https://doi.org/10.1016/j.compositesa.2015.08.037.

[22] **K. Mallick, M.L. Tupper, B.J. Arritt, C. Paul.** (2003). Thermo-micromechanics of microcracking in a cryogenic pressure vessel, in: *Collection Technical Papers - 44th AIAA/ASME/ASCE/AHS Structures, Structural Dynamics, and Materials Conference*, Norfolk, Virginia, pp. 3320–3329.

[23] **T. Yokozeki, T. Ogasawara, T. Aoki, T. Ishikawa.** (2006). Experimental evaluation of gas permeability through damaged composite laminates for cryogenic tank, *Special Issue 12th European Conference on Composite Materials ECCM 2006.*, ***69***, 1334–1340. https://doi.org/10.1016/j.compscitech.2008.05.019.

[24] **T. Yokozeki, T. Aoki, T. Ishikawa.** (2005). Experimental cryogenic gas leakage through damaged composite laminates for propellant tank application, *Journal of Spacecraft and Rockets*., ***42***. https://doi.org/10.2514/1.13955.

[25] **D. Gaulke, M. Malcherzyk, M. Meyer, B. Höck, S. Schmitt, T. Probst.** (2002). PHOEBUS, an ArianeGroup & MT-Aerospace cooperation for preparation of an optimized lightweight low cost future Upper Stage, in: *Proceedings of the International Astronautical Congress IAC*.

[26] **Url-2** <*https://www.toraytac.com/media/story/tAwc/Linerless-Liquid-Oxygen-LOX-tank-for-small-sat-space-launcher*>, date retrieved 01.09.2023.

[27] **T.K. DeLay.** (2000). *U.S. Patent No. 6,158,605.* Washington, DC: U.S. Patent and Trademark Office.

[28] **A. Elizabeth P. Kirn, Neil Anthony Graf, River Ridge, Kevin Wilbur Ely.** (2002). *U.S. Patent No. 6,334,589 B1*. Bethesada, MD: U.S. Patent and Trademark Office.

[29] **ASTM** (1995). *Standard Test Method for Compatibility of Materials with Liquid Oxygen (Impact Sensitivity Threshold and Pass-Fail Techniques) (ASTM D2512-95)*. https://doi.org/10.1520/D2512-95.

[30] **A. Elizabeth P. Kirn, Neil Anthony Graf, River Ridge, Kevin Wilbur Ely.** (2002). *U.S. Patent No. 6,375,125 B1*. Bethesada, MD: U.S. Patent and Trademark Office.

[31] **A. Elizabeth P. Kirn, Neil Anthony Graf, River Ridge, Kevin Wilbur Ely.** (2003). *U.S. Patent No. 6,491,259.* Bethesada, MD: U.S. Patent and Trademark Office.

[32] **A. Elizabeth P. Kirn, Neil Anthony Graf, River Ridge, Kevin Wilbur Ely.** (2002). *U.S. Patent No. 6,494,405.* Bethesada, MD: U.S. Patent and Trademark Office.

[33] **A. Kenneth R. Hampsten, N.** (2008). *U.S. Patent No. 7,389,890 B1*. Washington, DC: U.S. Patent and Trademark Office.

[34] **J.D. Menczel, R.B. Prime.** (2009). *Thermal Analysis of Polymers, Wiley*. https://doi.org/10.1002/9780470423837.

[35] **F. Schué.** (2002). Polymer analysis. Edited by Barbara Stuart. John Wiley and Sons, Chichester. pp 302,. ISBN 0-471-81363-X, *Polymer International*, ***52***, 1553–1553. https://doi.org/10.1002/pi.1256.

[36] **M.R. Saeb, E. Bakhshandeh, H.A. Khonakdar, E. Mäder, C. Scheffler, G. Heinrich.** (2013). Cure kinetics of epoxy nanocomposites affected by MWCNTs functionalization: *A review, The Scientific World Journal*. https://doi.org/10.1155/2013/703708.

[37] **J.E. Ehlers, N.G. Rondan, L.K. Huynh, H. Pham, M. Marks, T.N. Truong.** (2007). Theoretical study on mechanisms of the epoxy-amine curing reaction, *Macromolecules*., ***40***. https://doi.org/10.1021/ma070423m.

[38] **S. Nishijima, Y. Honda, T. Okada.** (1995). Application of the positron annihilation method for evaluation of organic materials for cryogenic use, *Cryogenics (Guildf).*, ***35***, 779–781. https://doi.org/10.1016/0011-2275(95)90913-Z.

[39] **ASTM** (2002). *Standard Test Methods for Flexural Properties of Unreinforced and Reinforced Plastics and Electrical Insulating Materials (ASTM D790-17)*. https://doi.org/10.1520/D0790-17.

[40] **T. Ueki, S. Nishijima, Y. Izumi.** (2005). Designing of epoxy resin systems for cryogenic use, *Cryogenics (Guildf).*, ***45***,. https://doi.org/10.1016/j.cryogenics.2004.07.002.

[41] **G. Hartwig.** (1978). Low-Temperature Properties of Epoxy Resins and Composites, in: *Advances in Cryogenic Engineering*, Springer US, Boston, MA, 1978: pp. 17–36. https://doi.org/10.1007/978-1-4613-9853-0_2.

[42] **Z. Sápi, R. Butler.** (2020). Properties of cryogenic and low temperature composite materials – A review, *Cryogenics (Guildf).*, ***111***, 103190. https://doi.org/10.1016/j.cryogenics.2020.103190.

[43] **Q. Feng, J. Yang, Y. Liu, H. Xiao, S. Fu.** (2014). Simultaneously Enhanced Cryogenic Tensile Strength, Ductility and Impact Resistance of Epoxy Resins by Polyethylene Glycol, *Journal of Materials Science & Technology*, ***30***, 90–96. https://doi.org/10.1016/j.jmst.2013.08.016.

[44] **K. Mishra, R.P. Singh.** (2013). Reinforcement of Epoxy Resins with POSS for Enhancing Fracture Toughness at Cryogenic Temperature. in: *Composite Materials and Joining Technologies for Composites*, ***7***, pp. 179–187. https://doi.org/10.1007/978-1-4614-4553-1_19.

[45] **G.D. Quinn.** (2020). NIST Recommended Practice Guide: Fractography of Ceramics and Glasses, 3rd edition, Special Publication (NIST SP), National Institute of Standards and Technology, Gaithersburg, MD, [online], https://doi.org/10.6028/NIST.SP.960-16e3.

[46] **B. Ellis.** (1993). *Chemistry and Technology of Epoxy Resins*, Springer Netherlands, Dordrecht. https://doi.org/10.1007/978-94-011-2932-9.

[47] **J. Rocks, G.A. George, F. Vohwinkel.** (2003). Curing kinetics and thermomechanical behaviour of co-anhydride cured aminoglycidyl epoxy resins, *Polymer International*, ***52***, https://doi.org/10.1002/pi.1286.

[48] **M. Nobelen, B.S. Hayes, J.C. Seferis.** (2003). Influence of Elastomer Distribution on the Cryogenic Microcracking of Carbon Fiber/Epoxy Composites, *Journal of Applied Polymer Science*, ***90***. https://doi.org/10.1002/app.12900.

[49] **Y. Zhao, Z.K. Chen, Y. Liu, H.M. Xiao, Q.P. Feng, S.Y. Fu**. (2013). Simultaneously enhanced cryogenic tensile strength and fracture toughness of epoxy resins by carboxylic nitrile-butadiene nano-rubber, *Composites Part A: Applied Science and Manufacturing*, ***55***. https://doi.org/10.1016/j.compositesa.2013.09.005.

[50] **R.N. Pease.** (1938). Combustion, Flames and Explosions of Gases (Lewis, Bernard; von Elbe, Guenther), *Journal of Chemical Education*, ***15***. https://doi.org/10.1021/ed015p448.3.

[51] **J.M. Kuchto, R.J. Goto, G.H. Mortindill.** (1971). Ignıtıon and Fire Suppression in Aerospace Vehicles National Technical (TECHNICAL REPORT AFAPL-TR-71-93). Pittsburghi Pennsylvania: NIST.

[52] **ASTM Flammability and Sensitivity of Materials in Oxygen-Enriched Atmospheres: Eighth Volume.** (1997). ASTM International. https://doi.org/10.1520/stp1319-eb.

[53] **N.A. Graf, R.J. Hudgins, M. Mcbain. (**2000). Oxygen Compatibility Testing of Composite Materials.

[54] **M. Robinson, J. Stolzfus, T. Owens.** (2001). Composite material compatibility with liquid and gaseous oxygen, in: *19th AIAA Applied Aerodynamics Conference, American Institute of Aeronautics and Astronautics*, Reston, Virigina. https://doi.org/10.2514/6.2001-1215.

[55] **P.M. Ordin.** (1997). *Safety standard for hydgogen and hydrogen systems. Guidelines for Hydrogen System Design, Materials Selection, Operations, Storage, and Transportation* (Technical Memorandum (TM) 19970033338), NASA.

[56] **L. Schoenma.** (1989). *Final Report Oxygen Materials Compatibility Testing* (Report No: NASA CR 182195). Cleveland, Ohio 44135: NASA.

[57] **J.B. Coleman.** (1976). *High-Pressure Liquid and Gaseous Oxygen Impact Sensivity Evaluation of Materials for Use at Kennedy Space Center* (Report No: NASA TN D-8160). Washington, D. C. : NASA.

[58] **W.A. Gayle, J.B., Key, C.F., Riehl.** (1963). *Reactivity of titanium with oxygen* (TECHNICAL REPORT R-180), Huntsville, AL, USA: NASA.

[59] **R. Wang, C. Zhang, W. Liu.** (2011). Compatibility and anti-oxidation properties of study on liquid oxygen compatibility with nano-modified epoxy composites, *Polymers and Polymer Composites*, ***19***. https://doi.org/10.1177/0967391111019004-515.

[60] **Z. Wu, J. Li, Y. Chen, Z. Wang, S. Li.** (2015). Synthesis and liquid oxygen compatibility of a phosphorous-containing epoxy resin, P*olymer Engineering and Science*, ***55***. https://doi.org/10.1002/pen.23933.

[61] **Boyd, W. K. Berry, W. E. White, E. L.** (1965). Compatibility of materials with rocket propellants and oxidizers (Report No: AD0613553). Ohio :DMIC.

[62] **E.S. Harrison.** (1973). *Liquid Oxygen-Compatible Filament-Winding Matrix Resin* (Report No: ADA307374), San Diego, CA: DMIC.

[63] **G. Wang, X. Li, R. Yan, S. Xing**. (2006). The study on compatibility of polymer matrix resins with liquid oxygen, *Materials Science and Engineering B: Solid-State Materials for Advanced Technology*, ***132***, 70–73. https://doi.org/10.1016/j.mseb.2006.02.028.

[64] **G.H. Abumeri, D.N. Kosareo, J.M. Roche.** (2004). Cryogenic composite tank design for next generation launch technology, in: *40th AIAA/ASME/SAE/ASEE oint Propulsion Conference and Exhibition*. https://doi.org/10.2514/6.2004-3390.

[65] **D. Chen, J. Li, Y. Yuan, C. Gao, Y. Cui, S. Li, X. Liu, H. Wang, C. Peng, Z. Wu.** (2021). A review of the polymer for cryogenic application: Methods, mechanisms and perspectives, *Polymers (Basel).*, ***13***. https://doi.org/10.3390/polym13030320.

[66] **D.S. Adams, D.E. Bowles, C.T.** (1986). Herakovich, Thermally Induced Transverse Cracking in Graphite-Epoxy Cross-Ply Laminates, *Journal of Reinforced Plastics and Composites*, ***5***,. https://doi.org/10.1177/073168448600500301.

[67] **V.T. Bechel, R.Y. Kim.** (2004). Damage trends in cryogenically cycled carbon/polymer composites, *Composites Science and Technology*, ***64***. https://doi.org/10.1016/j.compscitech.2003.12.007.

[68] **M. Flanagan, D.M. Grogan, J. Goggins, S. Appel, K. Doyle, S.B. Leen, C.M. Ó Brádaigh**. (2017). Permeability of carbon fibre PEEK composites for cryogenic storage tanks of future space launchers, *Composites Part A: Applied Science and Manufacturing*, ***101***, 173–184. https://doi.org/10.1016/j.compositesa.2017.06.013.

[69] **A.O. Pozdnyakov, M.M. Brzhezinskaya, A.S. Vinogradov, K. Friedrich.** (2008). NEXAFS spectra of polymer-nanocarbon composites, in: *Fullerenes, Nanotubutes Carbon Nanostructures*. https://doi.org/10.1080/15363830802282409.

[70] **X.J. Shen, Y. Liu, H.M. Xiao, Q.P. Feng, Z.Z. Yu, S.Y. Fu.** (2012). The reinforcing effect of graphene nanosheets on the cryogenic mechanical properties of epoxy resins, *Composites Science and Technology*, ***72***. https://doi.org/10.1016/j.compscitech.2012.06.021.

[71] **M. Tudela, R. Kim.** (2005). Impact damage response of composite materials at LOX/cryogenic temperatures, in: *Collection Technical Papers - AIAA/ASME/ASCE/AHS/ASC Structures, Structural Dynamics, and Materials Conference*, https://doi.org/10.2514/6.2005-2157.

[72] **X. Liu, T. Sun, Z. Wu, H. He.** (2018). Mode II interlaminar fracture toughness of unidirectional fiber-reinforced polymer matrix composites with synthetic boehmite nanosheets at room temperature and low temperature, *Journal of Composite Materials*, ***52***. https://doi.org/10.1177/0021998317716529.

[73] **B.C. Kim, S.W. Park, D.G. Lee.** (2008). Fracture toughness of the nano-particle reinforced epoxy composite, *Composite Structures*, ***86***. https://doi.org/10.1016/j.compstruct.2008.03.005.

[74] **P. Coronado, A. Argüelles, J. Viña, I. Viña.** (2014). Influence of low temperatures on the phenomenon of delamination of mode I fracture in carbon-fibre/epoxy composites under fatigue loading, *Composite Structures,* ***112***. https://doi.org/10.1016/j.compstruct.2014.02.007.

[75] **V.T. Bechel, M. Negilski, J. James.** (2006). Limiting the permeability of composites for cryogenic applications, *Composites Science and Technology,* ***66*** (2006). https://doi.org/10.1016/j.compscitech.2005.12.003.

[76] **J. Rousseau, D. Perreux, N. Verdière.** (1999). The influence of winding patterns on the damage behaviour of filament-wound pipes, *Composites Science and Technology,* ***59***. https://doi.org/10.1016/S0266-3538(98)00184-5.

[77] **M. Torres Arellano, L. Crouzeix, B. Douchin, F. Collombet, H. Hernández Moreno, J. González Velázquez.** (2010). Strain field measurement of filament-wound composites at ±55° using digital image correlation: An approach for unit cells employing flat specimens, *Composite Structures,* ***92***. https://doi.org/10.1016/j.compstruct.2010.02.014.

[78] **H. Hernández-Moreno, B. Douchin, F. Collombet, D. Choqueuse, P. Davies.** (2008). Influence of winding pattern on the mechanical behavior of filament wound composite cylinders under external pressure, *Composites Science and Technology,* ***68***. https://doi.org/10.1016/j.compscitech.2007.07.020.

[79] **Y. Zhang, Z. Xia, F. Ellyin.** (2008). Two-scale analysis of a filament-wound cylindrical structure and application of periodic boundary conditions, *International Journal of Solids and Structures,* ***45***. https://doi.org/10.1016/j.ijsolstr.2008.05.026.

[80] **H.H. Mian, H. Rahman.** (2011). Influence of mosaic patterns on the structural integrity of filament wound composite pressure vessels, *International Journal of Solids and Structures,* Integr., ***2***. https://doi.org/10.1108/17579861111162932.

[81] **S.P. Pai, D.W. Jensen.** (2001). Influence of Fiber Undulations on Buckling of Thin Filament-Wound Cylinders in Axial Compression, *Journal of Aerospace Engineering,* ***14***,12–20. https://doi.org/10.1061/(asce)0893-1321(2001)14:1(12).

[82] **E. Pourahmadi, F. Taheri-Behrooz.** (2020). The influence of fiber bundle width on the mechanical properties of filament-wound cylindrical structures, *International Journal of Mechanical Sciences,* ***178***,. https://doi.org/10.1016/j.ijmecsci.2020.105617.

[83] **C. Shen, X. Han.** (2018). Damage and failure analysis of filament wound composite structure considering fibre crossover and undulation, *Composites and Advanced Materials,* ***27***. https://doi.org/10.1177/096369351802700202.

[84] **M. Barcikowski, K. Rybkowska.** (2022). Mode II fracture characterization of toughened epoxy resin composites, *International Journal of Fracture,* ***234***. https://doi.org/10.1007/s10704-022-00616-4.

[85] **M.F. Abd Rased, S.H. Yoon.** (2021). Experimental study on effects of asymmetrical stacking sequence on carbon fiber/epoxy filament wound specimens in DCB, ENF, and MMB tests, *Composite Structures*, ***264*** (113749. https://doi.org/10.1016/j.compstruct.2021.113749.

[86] **A.B. De Morais, J.F. Silva, A.T. Marques, P.T. De Castro.** (2002). Mode II interlaminar fracture of filament wound angle-ply specimens, *Applied Composite Materials*, ***9***, 117–129. https://doi.org/10.1023/A:1013898312796.

[87] **J. Bonhomme, A. Argüelles, J. Viña, I. Viña.** (2009). Fractography and failure mechanisms in static mode I and mode II delamination testing of unidirectional carbon reinforced composites, *Polymer Testing*, ***28***. https://doi.org/10.1016/j.polymertesting.2009.05.003.

[88] **S. Li, D. Chen, Y. Yuan, C. Gao, Y. Cui, H. Wang, X. Liu, M. Liu, Z. Wu.** (2020). Influence of flexible molecular structure on the cryogenic mechanical properties of epoxy matrix and carbon fiber/epoxy composite laminate, *Materials and Design*, ***195***, 109028. https://doi.org/10.1016/j.matdes.2020.109028.

[89] **Y. Shindo, T. Takeda, F. Narita, N. Saito, S. Watanabe, K. Sanada.** (2009). Delamination growth mechanisms in woven glass fiber reinforced polymer composites under Mode II fatigue loading at cryogenic temperatures, *Composites Science and Technology*, ***69***, 1904–1911. https://doi.org/10.1016/j.compscitech.2009.04.010.

[90] **S. Choi, B. V. Sankar.** (2007). Fracture toughness of transverse cracks in graphite/epoxy laminates at cryogenic conditions, *Composites Part B: Engineering*, ***38***, 193–200. https://doi.org/10.1016/j.compositesb.2006.06.005.

[91] **ASTM** (2014). *Standard test method for determination of the mode II interlaminar fracture toughness of unidirectional fiber-reinforced polymer matrix composites* (ASTM D7905), https://doi.org/10.1520/D7905_D7905M-19E01.

[92] **ISO** (2015). *Fibre-reinforced plastics—methods of producing test plates—part 5: filament winding* (ISO 1268-5), Retrieved from www.iso.org/standard/27247.html.

[93] **V.K. Srivastava, T. Gries, D. Veit, T. Quadflieg, B. Mohr, M. Kolloch.** (2017). Effect of nanomaterial on mode I and mode II interlaminar fracture toughness of woven carbon fabric reinforced polymer composites, *Engineering Fracture Mechanics*, ***180***, 73–86. https://doi.org/10.1016/j.engfracmech.2017.05.030.

[94] **C. Peng, J. Li, Z. Wu, W. Peng, D. Zhou.** (2016). Investigating into the liquid oxygen compatibility of a modified epoxy resin containing silicon/phosphorus and its mechanical behavior at cryogenic temperature, *RSC Advances*, ***6***, 38300–38309. https://doi.org/10.1039/c6ra06033a.

[95] **I.M. Ward, P.R. Pinnock**. (1966). The mechanical properties of solid polymers, British Journal of Applied Physics, **17**, https://doi.org/10.1088/0508-3443/17/1/302.

[96] **X.X. Chu, Z.X. Wu, R.J. Huang, Y. Zhou, L.F. Li.** (2010). Mechanical and thermal expansion properties of glass fibers reinforced PEEK composites at cryogenic temperatures, *Cryogenics (Guildf).*, ***50***. https://doi.org/10.1016/j.cryogenics.2009.12.003.

[97] **T. Johannesson, P. Sjöblom, R. Seldén.** (1984). The detailed structure of delamination fracture surfaces in graphite/epoxy laminates, *Journal of Materials Science*, ***19***. https://doi.org/10.1007/BF01120026.

[98] **B.N. Nguyen, K.L. Simmons.** (2013). A multiscale modeling approach to analyze filament-wound composite pressure vessels, *Journal of Composite Materials*, ***47***. https://doi.org/10.1177/0021998312454508.

[99] **A.B. Pereira, A.B. De Morais.** (2004). Mode II interlaminar fracture of glass/epoxy multidirectional laminates, *Composites Part A: Applied Science and Manufacturing*, ***35***, 265–272. https://doi.org/10.1016/j.compositesa.2003.09.028.

[100] **S. Choi, B. V. Sankar.** (2006). Micromechanical analysis of composite laminates at cryogenic temperatures, *Journal of Composite Materials*, ***40***, 1077–1091. https://doi.org/10.1177/0021998305057365.

[101] **M. Azeem, H.H. Ya, M. Kumar, P. Stabla, M. Smolnicki, L. Gemi, R. Khan, T. Ahmed, Q. Ma, M.R. Sadique, A.A. Mokhtar, M. Mustapha.** (2022). Application of Filament Winding Technology in Composite Pressure Vessels and Challenges: A Review, *Journal of Energy Storage*, ***49***. https://doi.org/10.1016/j.est.2021.103468.

[102] **Url-3** <*https://texgen.sourceforge.io/index.php/Main_Page*>, date retrieved 18.06.2022.

[103] **P. Peddiraju, D. Lagoudas, J. Noh, J. Whitcomb.** (2004). Numerical modeling of cryogen leakage through composite laminates, in: *Collection of Technical Papers. - 45th AIAA/ASME/ASCE/AHS/ASC Structures, Structural Dynamics, and Materials Conference*, Palm Springs, California, pp. 3761–3771. https://doi.org/10.2514/6.2004-1862.

[104] **A. Nair, S. Roy.** (2007). Modeling of permeation and damage in graphite/epoxy laminates for cryogenic tanks in the presence of delaminations and stitch cracks, *Composites Science and Technology*, ***67***. https://doi.org/10.1016/j.compscitech.2006.12.003.

[105] **K.K. Jin, Y. Huang, Y.H. Lee, S.K. Ha.** (2008). Distribution of micro stresses and interfacial tractions in unidirectional composites, *Journal of Composite Materials*, ***42***, 1825–1849. https://doi.org/10.1177/0021998308093909.

[106] **P.F. Liu, J.K. Chu, S.J. Hou, J.Y. Zheng.** (2012). Micromechanical damage modeling and multiscale progressive failure analysis of composite pressure vessel, *Computational Materials Science*, ***60***. https://doi.org/10.1016/j.commatsci.2012.03.015.

[107] **M. fa Ren, X. wen Zhang, C. Huang, B. Wang, T. Li.** (2019). An integrated macro/micro-scale approach for in situ evaluation of matrix cracking in the polymer matrix of cryogenic composite tanks, *Composite Structures*, ***216***, 201–212. https://doi.org/10.1016/j.compstruct.2019.02.079.

[108] **M.F. Ren, X. Chang, H.Y. Xu, T. Li.** (2017). Trans-scale analysis of composite overwrapped pressure vessel at cryogenic temperature, *Composite Structures*, ***160***. https://doi.org/10.1016/j.compstruct.2016.10.126.

[109] **C. Huang, M.F. Ren, T. Li, X. Chang, J. Cong, Y.J. Lei.** (2016). Trans-scale modeling framework for failure analysis of cryogenic composite tanks, *Composites Part B: Engineering*, ***85***, 41–49. https://doi.org/10.1016/j.compositesb.2015.09.023.

[110]**W. Li, H. Cai, C. Li, K. Wang, L. Fang.** (2015). Micro-mechanics of failure for fatigue strength prediction of bolted joint structures of carbon fiber reinforced polymer composite, *Composite Structures*, ***124***, 345–356. https://doi.org/10.1016/j.compstruct.2015.01.026.

[111] **T.E. Tay, G. Liu, V.B.C. Tan, X.S. Sun, D.C. Pham.** (2008). Progressive failure analysis of composites, *Journal of Composite Materials*, ***42***, 1921–1966. https://doi.org/10.1177/0021998308093912.

[112] **Url-4** <*https://www.engineeringtoolbox.com/thermal-conductivity-d_429.html*>, date retrieved 14.03.2020.

[113] **T.M. Flynn.** (2004). *Cryogenic engineering: Second edition, revised and expanded*, https://doi.org/10.1201/9780203026991.

[114] **Url-4** <*https://www.engineeringtoolbox.com/linear-expansion-coefficients-d_95.html*>, date retrieved 14.03.2020.

[115] **H. min Kang, J.K. Lee.** (2014). *U.S. Patent No. 2015/025874.0 A1*. Seoul, KR: U.S. Patent and Trademark Office.

[116] **J. Kaerger, L. Atz.** (2019). Water Soluble Mandrels for Lost Core Applications in Manufacturing of Hollow Composite Structures, in: *SAMPE European Conference*, Nantes.

[117] **J.C. Brooks.** (1987). *U.S. Patent No. 4,684,423*. Utah: U.S. Patent and Trademark Office.

[118] **Pearce. G.** (2019). Design of a Linerless Carbon Fibre Composite Pressure Vessel for Cryogenic Fuel Tank Applications, in: *Hydrogen Liquefaction and Storage Symposium*, University of Western Australia, Perth.

[119] **A.S. Kaddour, M.J. Hinton.** (2012). Input data for test cases used in benchmarking triaxial failure theories of composites, *Journal of Composite Materials*, ***46***. https://doi.org/10.1177/0021998312449886.

CURRICULUM VITAE

Name Surname **: Recep UFUK**

EDUCATION **:**

- **B.Sc.** **:** 2012, Istanbul Technical University, Faculty of Civil Engineering, Civil Engineering
- **B.Sc.** **:** 2014, Istanbul Technical University, Faculty of Mechanical Engineering, Mechanical Engineering
- **M.Sc.** **:** 2016, Istanbul Technical University, Faculty of Mechanical Engineering, Automotive

PROFESSIONAL EXPERIENCE AND REWARDS:

- 2014-2017 CAE Engineer at SDM Research and Engineering.
- 2017-2017 Researcher at TUBITAK Space Technologies.
- 2017- Lead R&D Engineer at DeltaV Space Technologies.

PUBLICATIONS, PRESENTATIONS AND PATENTS ON THE THESIS:

- **Ufuk, R., Karakaş, T., Bilge, K., Ereke, Karabeyoğlu, A.** 2022: Linerless Hybrid Structured Composite Pressure Vessel Development. International Graduate Research Symposium (IGRS22), June 1-3, 2023, Istanbul, Türkiye.
- **Ufuk, R., Karakaş, T., Bilge, K., Ereke, Karabeyoğlu, A** 2023: Cryogenic Type-V Pressure Vessel Design, Manufacturing And Testing. 23rd International Conference on Composite Materials (ICCM23), August, 2023, Belfast, UK.
- **Ufuk, R., Bilge, K., Kıral, B.K., Ereke, Karabeyoğlu, A.** 2023. Fractographic Investigation of Cryogenic Temperature Mode-II Delamination Behavior of Filament Wound CFRP Laminates with Varied Resin Systems, *Journal of Composites Science*, ***7***, no. 11: 450. https://doi.org/10.3390/jcs7110450